

In Situ Modeling of Chemical Membrane Degradation in Polymer Electrolyte Fuel Cells

by

Ka Hung Wong

M.Phil, The Hong Kong Polytechnic University, 2012

B.Sc., The Chinese University of Hong Kong, 2007

Thesis Submitted in Partial Fulfillment of the
Requirements for the Degree of
Doctor of Philosophy

in the
School of Mechatronic Systems Engineering
Faculty of Applied Sciences

© Ka Hung Wong 2015

SIMON FRASER UNIVERSITY

Summer 2015

All rights reserved.

However, in accordance with the *Copyright Act of Canada*, this work may be reproduced, without authorization, under the conditions for "Fair Dealing." Therefore, limited reproduction of this work for the purposes of private study, research, criticism, review and news reporting is likely to be in accordance with the law, particularly if cited appropriately.

CONFIDENTIAL

Approval

Name: Ka Hung Wong
Degree: Doctor of Philosophy (Mechatronic Systems Engineering)

Title: *In Situ Modeling of Chemical Membrane Degradation
in Polymer Electrolyte Fuel Cells*

Examining Committee: Chair: Gary Wang
Professor

Erik Kjeang
Senior Supervisor
Assistant Professor

Michael Eikerling
Supervisor
Professor

Ned Djilali
Supervisor
Professor

Majid Bahrami
Internal Examiner
Associate Professor
School of Mechatronic Systems
Engineering

Kunal Karan
External Examiner
Associate Professor
Chemical and Petroleum Engineering
University of Calgary

Date Defended/Approved: June 23rd, 2015

Partial Copyright Licence



The author, whose copyright is declared on the title page of this work, has granted to Simon Fraser University the non-exclusive, royalty-free right to include a digital copy of this thesis, project or extended essay[s] and associated supplemental files (“Work”) (title[s] below) in Summit, the Institutional Research Repository at SFU. SFU may also make copies of the Work for purposes of a scholarly or research nature; for users of the SFU Library; or in response to a request from another library, or educational institution, on SFU’s own behalf or for one of its users. Distribution may be in any form.

The author has further agreed that SFU may keep more than one copy of the Work for purposes of back-up and security; and that SFU may, without changing the content, translate, if technically possible, the Work to any medium or format for the purpose of preserving the Work and facilitating the exercise of SFU’s rights under this licence.

It is understood that copying, publication, or public performance of the Work for commercial purposes shall not be allowed without the author’s written permission.

While granting the above uses to SFU, the author retains copyright ownership and moral rights in the Work, and may deal with the copyright in the Work in any way consistent with the terms of this licence, including the right to change the Work for subsequent purposes, including editing and publishing the Work in whole or in part, and licensing the content to other parties as the author may desire.

The author represents and warrants that he/she has the right to grant the rights contained in this licence and that the Work does not, to the best of the author’s knowledge, infringe upon anyone’s copyright. The author has obtained written copyright permission, where required, for the use of any third-party copyrighted material contained in the Work. The author represents and warrants that the Work is his/her own original work and that he/she has not previously assigned or relinquished the rights conferred in this licence.

Simon Fraser University Library
Burnaby, British Columbia, Canada

revised Fall 2013

Abstract

Chemical membrane degradation is a major limiting factor for polymer electrolyte fuel cell (PEFC) durability and lifetime. While the effects of chemical membrane degradation are characterized in the literature, the underlying mechanism is not fully understood. This motivates the development of a comprehensive in situ chemical membrane degradation model addressed in this work to determine the linkages between the membrane electrolyte assembly (MEA) macroscopic phenomena, in situ operating conditions, and the temporal membrane degradation process. Chemical membrane degradation through OH radical attack on the membrane, where the radical is produced by decomposition of hydrogen peroxide in the presence of contaminants such as Fe²⁺, is comprehensively investigated. A redox cycle of iron ions is discovered within the MEA which sustains the Fe²⁺ concentration in the membrane and results in the most severe chemical degradation at open circuit voltage (OCV). The cycle is suppressed at lower cell voltages leading an exponential decrease in Fe²⁺ concentration in the membrane and associated membrane degradation rate, which suggests that intermediate cell voltage operation would efficiently mitigate chemical membrane degradation and extend the fuel cell lifetime.

Effectiveness of membrane additives (e.g., ceria) in mitigating the membrane degradation is explored. At high cell voltages, abundant Ce³⁺ ions are available in the membrane to quench hydroxyl radicals which is the primary mitigation mechanism observed at OCV conditions. However, the mitigation is suppressed at low cell voltages, where electromigration drives Ce³⁺ ions into the cathode catalyst layer (CL). Without an adequate amount of Ce³⁺ in the membrane, the hydroxyl radical scavenging is significantly reduced. Moreover, the modeling results reveal that proton starvation may occur in the cathode CL due to local Ce³⁺ accumulation and associated reductions in proton conductivity and oxygen reduction kinetics. Significant performance tradeoffs in the form of combined ohmic and kinetic voltage losses are therefore evident. A lower initial Ce³⁺ concentration is demonstrated to mitigate voltage losses without compromising membrane durability at high cell voltages. However, the harmful Fe²⁺ concentration in the membrane increases with the Ce³⁺ concentration, which suggests that ceria-supported MEAs can experience higher rates of degradation than baseline MEAs at low cell voltages. Strategic MEA design is recommended in order to ensure membrane durability at low cell voltages.

CONFIDENTIAL

Keywords: Durability; fuel cells; membranes; chemical degradation; modeling

Dedication

I dedicate my thesis to the many people who have inspired me.

Acknowledgements

I would like to express my deepest appreciation to my supervisor, Dr. Erik Kjeang, who have supported and guided me over the years in my research. I am indebted to him for sharing his expertise that advances and consolidates the work presented in this thesis.

I am also very grateful to my committee members, Dr. Ned Djilali and Dr. Michael Eikerling, for their mentorship and valuable comments and advices which enhance the quality of my research.

I would like to thank my colleagues at SFU FCREL, Ballard, and UVic for their helps and inspirations, and I have had the great pleasure to work with them.

I would like to acknowledge the financial support from Ballard Power Systems and the Natural Sciences and Engineering Research Council of Canada through an Automotive Partnership Canada (APC) grant.

Finally, I would like to take this opportunity to express my gratitude to my family for their endless love. It is their encouragements to support me studying overseas. I would also like to thank my girlfriend and my friends I met in Canada for their constantly supports.

Table of Contents

Approval.....	ii
Partial Copyright Licence	iii
Abstract.....	iv
Dedication.....	vi
Acknowledgements	vii
Table of Contents.....	viii
Chapter 1. Introduction	1
1.1. Objective	1
1.2. Introduction on Polymer Electrolyte Fuel Cell Technology	3
1.3. Overview of Degradation Mechanisms in MEA	4
1.3.1. CL and GDL Degradations	4
1.3.2. Membrane Degradation	5
Thermal Degradation	6
Mechanical Degradation	6
Chemical Degradation Mechanism and its Mitigation Strategies	7
Effects of Chemical Degradation	11
1.4. Modeling of Chemical Membrane Degradation	12
1.4.1. Challenges in Modeling of Chemical Membrane Degradation.....	15
Chapter 2. Summary of Contributions.....	17
2.1. Macroscopic In Situ Modeling of Chemical Membrane Degradation in Polymer Electrolyte Fuel Cells	17
2.1.1. Model Formulation and Assumptions.....	17
Assumptions.....	17
Modeling Domain	18
Species of interest.....	18
Ionomer Degradation Model	19
2.1.2. Model Validation	19
2.1.3. Model Challenges and Opportunities	21
2.2. Mitigation of Chemical Membrane Degradation in Fuel Cells: Understanding the Effect of Cell Voltage and Iron Ion Redox Cycle	22
2.2.1. Membrane Contaminants and Additives	23
2.2.2. PFSA Ionomer Degradation.....	24
2.2.3. Open Circuit Voltage	24
2.2.4. Below Open Circuit Voltage	25
2.2.5. Further Discussion.....	27
2.3. In situ modeling of chemical membrane degradation mitigation in ceria- supported fuel cells.....	28
2.3.1. Open Circuit Voltage	28
2.3.2. Below Open Circuit Voltage	29

CONFIDENTIAL

2.4. Simulation of Performance Tradeoffs in Ceria Supported Polymer Electrolyte Fuel Cells	31
2.4.1. Model Assumptions	32
2.4.2. Beginning of Life (BOL) MEA Performance.....	32
2.4.3. Membrane Durability and Fuel Cell Performance.....	34
Chapter 3. Conclusions and Future Research.....	37
3.1. Challenges and Opportunities.....	39
References	42
Appendix A: Macroscopic In-Situ Modeling of Chemical Membrane Degradation in Polymer Electrolyte Fuel Cells	53
Appendix B: Mitigation of Chemical Membrane Degradation in Fuel Cells: Understanding the Effect of Cell Voltage and Iron Ion Redox Cycle	64
Appendix C: In situ modeling of chemical membrane degradation and mitigation in ceria-supported fuel cells	77
Appendix D: Simulation of Performance Tradeoffs in Ceria Supported Polymer Electrolyte Fuel Cells	116

Chapter 1.

Introduction

1.1. Objective

The objective of this work is to develop an *in situ* chemical membrane degradation model for an operating polymer electrolyte fuel cell (PEFC). This *in situ* model targets on modeling the chemical membrane degradation and exploring its coupling effects in a standard membrane electrolyte assembly (MEA) which consists of membrane, catalyst layer (CL), and gas diffusion layer (GDL). The developed degradation model also aims to provide a platform in evaluating the effectiveness of advanced materials design and fuel cell operation on mitigation of membrane degradation.

The work presented in this thesis belongs to the modeling component of the Automotive Partnership of Canada (APC) funded project aiming to develop next generation heavy duty fuel cell (NG-HDFC) technology with enhanced durability and reliability (www.apc-hdfc.ca). The project focuses on the durability issue of perfluorosulfonic acid (PFSA) ionomer membranes, which are generally use in hydrogen PEFCs to separate the two electrodes in the MEA. Although PFSA membranes have high proton conductivity at low temperatures, relatively low reactant permeation, and superior electrical insulation leading to high fuel cell performance, the ionomer membrane can be degraded in the fuel cell environment which reduces its stability and limits its lifetime [1, 2]. Chemical and mechanical degradation are the primary mechanisms leading membrane failure that resulted from lifetime limiting hydrogen leaks across the MEA. In the project, chemical membrane degradation is investigated by

CONFIDENTIAL

various experimental and modeling methodologies. Based on the developments from these investigations and existing knowledge in the literature, an underlying chemical membrane degradation mechanism is developed and is incorporated into a state-of-the-art MEA fuel cell performance model to achieve an *in situ* modeling platform for chemical membrane degradation as presented in this thesis. As a modeling task in the NG-HDFC project, the *in situ* modeling platform is applied to generate a set of metrics to represent the chemical degradation fingerprints, including the changes in ion exchange capacity (IEC), fluoride release rate, membrane thinning, open circuit voltage (OCV) decay, and reduction in proton conductivity. These metrics are used to quantify the rate of chemical membrane degradation. The degradation model is also a modeling element which can be integrated with the mechanical membrane degradation model and the statistical ionomer aggregation model developed in the project to form a more general membrane durability model in which chemical, mechanical, and coupled degradation modes can be addressed. Key phenomena related with membrane stabilizing additives are included in the proposed model. Their behaviours and interactions between other fuel cell components under an *in situ* operating fuel cell are explored and examined which generate a portfolio of results that can be applied in selecting next generation stabilizing additives for fuel cell.

Notable significant efforts have been made in characterizing and understanding the chemical membrane degradation in PEFC which indicate the degradation mechanism involves formation of hydrogen peroxide and oxygen radicals and radical attack on the membrane. However, full understanding cannot be achieved without considering these degradation processes in operating hydrogen PEFCs. The role of this thesis in fuel cell durability research is to establish an *in situ* chemical membrane degradation model in which the chemical degradation processes of membrane in operating fuel cell are simulated. The developed model attempts to explore the missing but important mechanisms in chemical membrane degradation. In order to make this objective clear, an introduction on fuel cell technology is given in Section 1.2, followed by an overview on fuel cell degradation in Section 1.3. Finally, a detailed review on the modeling of chemical membrane degradation is given in Section 1.4.

1.2. Introduction on Polymer Electrolyte Fuel Cell Technology

Fuel cells are electrochemical devices that continuously convert the chemical energy of a fuel and oxidant directly into electricity.

The possible applications of fuel cell technology include portable, stationary, and transport applications. Currently, hydrogen PEFCs are the leading alternatives to heat engines in transport applications because they can operate at low temperatures (<100°C) [3]. PEFCs use a thin and solid PFSA ionomer membrane as a polymer electrolyte to separate the fuel and oxidant. The ionomer membrane is sandwiched between two thin and porous electrodes which consist of CL and GDL. GDL is a macroporous substrate with various additive materials such as microporous layer (MPL) and polytetrafluoroethylene (PTFE) to manage water transport within PEFCs. CL has a more complex structure with ionomer and carbon inter-connected networks and distributed platinum (Pt) as a catalyst to enhance the oxygen reduction reaction (ORR). Both GDL and CL are highly porous to provide good reactant transport to and product removal from the catalyst.

In the anode CL, hydrogen is oxidized to generate electrons and protons. Protons are transported from anode CL to cathode CL through an ionically conductive but electrically insulating PFSA ionomer membrane. Simultaneously, electrons are transported from anode CL to cathode CL via external circuit. In the cathode CL, oxygen is electrochemically reduced by recombining with protons and electrons from anode CL [3]. The reduction has a slow kinetic, and therefore platinum is incorporated to enhance the kinetic. The use of platinum also allows PEFCs to operate at a low temperature, which makes PEFCs having a rapid response with respect to changes in power output.

The feasibility of PEFC technology in transport applications has been widely demonstrated in various fuel cell electric bus (FCEB) projects around the world [4]. FCEBs have been shown to be more fuel efficient compared to diesel buses. Moreover, using hydrogen as a fuel, FCEBs has zero emission at the point of use. PEFCs are also

CONFIDENTIAL

applicable in light vehicles; several automobile companies such as Hyundai [5] are launching fuel cell electric vehicles based on PEFC technology in 2015. Recently, Ballard Power Systems has successfully demonstrated the world's first PEFC powered electric tram in China (<http://www.ballard.com>). Although PEFC technology has been well demonstrated in various transport applications, several technical barriers have to be addressed to achieve complete commercialization of PEFC technology. The main challenges include PEFC durability and stability, and initial capital cost of PEFC power modulus [1, 2]. For example, the current Ballard HD-6 fuel cell module offers 12000 hours lifetime with 5-year warranty [4]. However, the Department of Energy and the Department of Transportation's Federal Transit Administration set a target of 25000 hours durability for fuel cell propulsion system. In PEFCs, safe operation of fuel cell stacks is heavily relied on the low gas permeability of ionomer membrane, but microscopic pinholes and divots that allow reactant permeation have been observed in the degraded MEAs from FCEBs [4]. The reactant permeation can cause performance losses and result in direct combustion of hydrogen and oxygen at pinholes or divots which generates local hot spots which can decompose the ionomer [1, 2]. Eventually, a significant amount of leak of reactants is generated to cause fuel cell failure. As a result, membrane degradation has a more significant impact on the fuel cell lifetime with respect to MEA cracking than other degradations take place in other MEA components such as CL and GDL, which are related with fuel cell performance losses.

1.3. Overview of Degradation Mechanisms in MEA

1.3.1. CL and GDL Degradations

In CLs, high electrochemical active surface area (ECSA) per volume has been achieved by applying high-surface-area carbon supported Pt catalyst. However, ECSA can be reduced during fuel cell operations. The loss of ECSA is attributed to Pt dissolution, coarsening of Pt particles, and corrosion of carbon support [6, 7]. Pt dissolution is enhanced by high cell voltages, low pH values, high temperatures, and transient voltage conditions [8] which suggest Pt dissolution is more significant at

CONFIDENTIAL

cathode CL. The dissolved Pt can either deposit on the surface of larger Pt particles leading to particle growth (coarsening of Pt particle) or transport across the membrane and precipitate in the membrane or anode CL by reacting with hydrogen [6, 7, 9]. Carbon corrosion is found to be sensitive cell voltage, and the corrosion is accelerated at high cell voltages [6, 7]. Therefore, carbon corrosion is believed to be more significant at the cathode CL during usual fuel cell operations. The corrosion reduces the amount of carbon support in CLs which directly increases electrical resistance and reduces the ECSA in CLs.

The main roles of the GDL are to allow reactant transport from fuel cell gas channel to the active surface in the CL and transfer electrons between the CL and bipolar plates for continuously supporting the electrochemical reactions. The GDL is also responsible for facilitating water vapor and liquid water transports in fuel cell to maintain effective reactant transport. Hydrophobic material is usually added in the GDL to prevent the blockages of pores due to water flooding at high current densities. The MPL is inserted between the GDL macroporous substrate and CL to remove the excess water and maintain an adequate amount of water in the CL and membrane [10]. An adequate amount of water in fuel cell is critical to fuel cell performance. However, the wetting properties in the GDL can change due to loss of the hydrophobic material and surface oxidation of the carbon fiber, which reduces the stability of the fuel cell performance [6, 11].

Although the GDL and CL do degrade in the fuel cell environment and lead degradation in the fuel cell performance, these degradation processes are out of the scope for this thesis and are not considered in the development of the degradation model.

1.3.2. Membrane Degradation

This section covers thermal, mechanical, and chemical degradations in PFSA membrane. Detailed discussion on chemical degradation including the mitigation strategies is provided.

Thermal Degradation

PFSA membrane can experience thermal decomposition at temperature above 200°C. About this temperature, sulfonic acid groups begin to decompose due to C-S bond cleavage which leads the formation of sulfur dioxide, OH radical and carbon-based radical on the chain [7]. Degradation can propagate along the degraded chain when the temperature is further elevated [1, 7]. On the other hand, PFSA membrane is relatively robust at typical fuel cell operating temperature because of the strong C-F bond and the shielding effect induced by the electronegative fluorine atoms the backbone [1, 7], and hence thermal degradation is possibly not the initiating reaction to cause fuel cell failures. .

Mechanical Degradation

The fuel cell operating condition changes with respect to the varying power demand in heavy duty transport applications, which result in cyclic membrane swelling and contraction due to hygrothermal variations. Since the membrane is confined within the MEA, the swelling and contraction impose mechanical stress on the membrane [12]. The stress generated can possibly cause permanent plastic membrane degradation in catalyst coated membranes (CCM) because of the elastic-viscoplastic behavior of CCMs [13, 14]. Fatigue process in the membrane due to cyclic stress has been analyzed and simulated, and these studies suggested that the fatigue process can finally lead membrane fracture [15, 16]. Creep (time dependent deformation under constant applied stress) can also result in mechanical damage on the membrane and CCM [17]. Interestingly, temperature is found to be more dominant than relative humidity in both creep behaviour and fatigue process of the membrane [16, 17], and this may suggest the mechanical degradation is more severe at fuel cell conditions than at room conditions. However, the membrane degradation at fuel cell conditions is further compounded by the chemical degradation which can dramatically deteriorate the physicochemical and mechanical properties of the membrane [13, 18, 19, 20].

Chemical Degradation Mechanism and its Mitigation Strategies

Chemical membrane degradation is considered to be caused by radical attack on the membrane during fuel cell operation [21, 22, 23, 24, 25]. This hypothesis is corroborated by the *in situ* detection of hydroxyl ($\cdot\text{OH}$), hydroperoxyl ($\cdot\text{OOH}$), and hydrogen ($\text{H}\cdot$) radicals and degraded ionomer species comprising oxygen and carbon centered radicals by utilizing an electron spin resonance (ESR) spectrometer [26, 27] or a fluorescence probe [28]. The hydroxyl radical can be generated in the membrane and is considered to be the “usual suspect” responsible for the chemical degradation [22, 29] and to initiate the formation of the hydroperoxyl and hydrogen radicals [29].

In hydrogen PEFC, the presence of the hydroxyl radical is highly related with the hydrogen peroxide, which was detected in the effluent water collected during OCV accelerated stress test (AST) [30]. The formation of hydrogen peroxide has been observed when oxygen was reduced at Pt or Pt/C catalyst in the hydrogen-rich environment (voltage < 0.2 V) via two-electron ORR [31, 32]. The estimated diffusion length of hydrogen peroxide is in the centimeter range that indicates hydrogen peroxide can diffuse through the entire membrane [29]. When there are contaminants such as Fe^{2+} and Cu^+ in the membrane, hydroxyl radical can be formed upon the decomposition of hydrogen peroxide [30, 33]. Among these metal contaminants, the Fe^{2+} ion is found to have the highest impact on the rate of chemical degradation [34]. This finding is also consistent with the *ex situ* Fenton's test [35] in which an increased formation of fluoride ions and hydroxyl radicals was observed in Fe^{2+} -exchanged membranes compared with as-received and platinum(Pt)-dispersed membranes. Indeed, a higher Fe^{2+} ion concentration has stronger impact on the degradation rate as revealed by the decomposition of CF_2 in the polymer backbone detected by means of X-ray photoelectron spectroscopy [36].

In the Pt-dispersed membrane, hydroxyl radical is suggested to be formed from the decomposition of hydrogen peroxide on the Pt surface or the reaction of dissolved oxygen and hydrogen upon the Pt surface [37, 38]. However, the mechanism of hydroxyl radical formation via Pt in the membrane is still contentious; for example, the direct OH

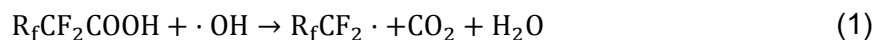
CONFIDENTIAL

radical formation from dissolved oxygen in the membrane is not likely to happen [39]. Moreover, mitigating effects on the membrane degradation have been observed when Pt band is formed in the membrane [19, 40]. The dual role of the Pt is suggested to depend on the Pt particle size and particle density in the membrane which determine the rate of radical formation and decomposition [38]. The Pt catalyst property could depend on the local equilibrium condition at Pt in the membrane [41]. Overall, it is important to capture the local distribution and transport phenomena of membrane contaminants such as Pt and iron in the chemical degradation model. Pt is in general absent in fresh MEAs. However Pt can migrate from CLs to membrane, which is a common consequence of CL degradation. Deposition of Pt in the membrane is a complicated process involving dissolution of Pt, transport of Pt ion or Pt complex, Pt reduction by dissolved hydrogen in the membrane, and growth of Pt particle. Hence, the Pt distribution, size, and form in the membrane are highly related with the fuel cell materials and operating conditions, which are expected to have influences on the dual role of the Pt in chemical membrane degradation. Iron contaminant is commonly present in fuel cell materials due to fuel cell fabrication and may also enter the MEA during fuel cell operation. However, their exact forms and positions in the MEA during operation are generally unknown.

The first proposed chemical degradation mechanism for PFSA membrane is hydroxyl radical attack on H-containing end groups terminated the main chain of the ionomer which can be formed during the membrane manufacturing [21, 42, 43]. One of the most common end groups considered in the degradation process is the carboxylic acid end group, $R_f\text{COOH}$. The proposed degradation proceeds via unzipping reaction including sequential reactions which are initiated by hydroxyl radical attack at the carboxylic acid end groups [21, 42, 43]. When the carboxylic acid end group is attacked by hydroxyl radical, a hydrogen is abstracted from the acid end group to form a perfluorocarbon radical and release a carbon dioxide and water as described in Eq. (1). The perfluorocarbon radical, $R_f\text{CF}_2\cdot$, can react with hydroxyl radical to give a perfluoroalcohol, $R_f\text{CF}_2\text{OH}$, which can be decomposed to an acid fluoride, $R_f\text{COF}$, and a hydrogen fluoride (Eq. (2)). The acid fluoride can be hydrolyzed to form a new carboxylic acid end group and release another hydrogen fluoride presented in Eq. (3). The unzipping reaction can continue provided that CF_2 group is present in the degraded main

CONFIDENTIAL

chain. This chemical membrane degradation has been discussed and modeled [29, 43, 44]. However, more recent studies focused on side chain degradation [25, 45, 46, 47, 48, 49] that has become more important in developing mitigation strategies for chemical membrane degradation since the carboxylic acid group concentration of recent industry standard membranes is significantly reduced [50].



The side chain degradation due to hydroxyl radical attack has two possible initiating regions, carbon-sulphur (C-S) bond and ether bond cleavages were suggested in the literature. C-S bond cleavage was proposed in the literature [24, 46, 48] and supported by density functional theory (DFT) calculations [46, 48]. However, ether bond cleavage was shown to be more favorable in other DFT calculations [45] and supported by several experiments [18, 25, 49]. The side chain unzipping reaction in recent chemically stabilized PFSA membranes has been demonstrated to be initialized from hydroxyl radical attack on the ether bond in the OCF_2 group (αOCF_2) which is closer to the ionic head groups [25, 49]. Hydroxyl radical can further attack the degraded side chain after cleaving the ether bond in αOCF_2 group leading to the unzipping of the side chain [49]. This stepwise degradation can propagate along the side chain until main chain scission occurs by hydroxyl radical attack of the OCF_2 group near the main chain [24, 43, 51]. The carboxylic acid groups formed after the main chain scission event further degrade via the well-established main chain unzipping reaction [43, 50]. The additional material loss contributed by main chain degradation was recently confirmed experimentally [18].

Recently, hydrogen radical attack at the CF bond in the tertiary carbon where the side chain is attached to the main chain has been observed in *ex situ* experiment [49].

CONFIDENTIAL

Since hydroxyl radical has the higher redox potential [2] and higher concentration in fuel cell system [29] than hydrogen radical, the side chain degradation in PFSA membrane is predominant due to the hydroxyl radical attack on the ether bond.

Considering the dominant role of hydroxyl radicals in the chemical membrane degradation, radical scavenging is proposed to mitigate the chemical damage by quenching the radicals before they attack the ionomer. Metal cations such as Ce^{3+} and Mn^{2+} are proposed to quench the radicals in the membrane [23, 52]. Introduction of either Ce^{3+} or Mn^{2+} cations in the electrode or in the membrane significantly reduces the chemical membrane degradation rate indicated by the dramatic reductions in fluoride release rate and in OCV decay rate [23]. Moreover, Ce^{3+} is found to be about four times more effective than Mn^{2+} at reducing fluoride release rate when they have the same concentration [23].

Another promising membrane additive to quench $\cdot\text{OH}$ in fuel cells is ceria (CeO_2), which has been shown to effectively protect the ionomer membrane under OCV AST or *ex situ* Fenton's durability test conditions [23, 53, 54, 55, 56, 57, 58]. Ceria in general can dissolve in acidic aqueous environments provided that the electrochemical potential is not too high (below 1.76 V) according to the Pourbaix diagram for cerium [59]. Due to the high proton concentration ($c_{\text{H}^+} \approx 1800 \text{ mol m}^{-3}$) and relatively low operating potentials (0 – 1 V) of PEFCs, ceria dissolves and forms a $\text{Ce}^{3+}/\text{Ce}^{4+}$ redox couple in the ionomer phase when it is incorporated in the CLs or membrane [57, 60]. The Ce^{3+} ion can react with $\cdot\text{OH}$ and oxidize to the Ce^{4+} ion, while the Ce^{4+} ion can be reduced to the Ce^{3+} ion by reacting with hydrogen peroxide or hydrogen [21]. However, the distribution, transport, and formation/consumption of cerium ions within a fuel cell would be very challenging to measure quantitatively within an operating fuel cell [61]. The experimental limitations can be compensated by using fuel cell modeling methodologies to analyze the chemical membrane degradation and mitigation in ceria supported MEA. Although ceria additive can mitigate membrane degradation at OCV conditions, it has also been shown to compromise the fuel cell performance [62]. The performance drop is believed to have the same origin as the effects caused by cationic contaminants (such as iron and copper ions). Their performance effect is associated with reduced proton

concentration and conductivity in the membrane [63, 64, 65] since ceria can dissolve into the ionomer phase and bond to the sulfonic acid end group. The voltage losses predicted for ceria-supported MEAs are expected to counteract the durability benefits and may possibly even outweigh the motivation for the use of radical scavengers unless care is taken to analyze the interactions between membrane stability and MEA performance.

Effects of Chemical Degradation

Accelerated stress test (AST) is designed to elevate the chemical membrane degradation in an operating PEFC by elevating the cell temperature, cell voltage, and inlet oxygen partial pressure or reducing the relative humidity of the inlet gases [18, 19, 30, 66]. Various diagnostic methods are then applied on the AST degraded samples to characterize the effects of chemical membrane degradation.

Fluoride loss has been widely observed in the AST degraded samples and is considered to be an important indicator of chemical membrane degradation [18, 19, 30]. The fluoride loss is originated from the hydrogen fluoride and fluorine-containing fragments formed during the chemical degradation. The degradation possibly occurs in both side chain and main chain of the ionomer as suggested by the numerous fluoride loss observed in the recent OCV AST [18]. Membrane thinning is another indicator of chemical membrane degradation which is prevalent in the AST degraded samples [18, 19]. In general, the membrane thickness loss is in good agreement with the cumulative fluoride loss [18, 19].

The chemical membrane degradation also causes OCV decay [18, 19, 30]. The OCV drop starts with a milder decay rate, and the decay rate is significantly increased at the end of the AST. The growth in the OCV drop is highly consistent with the increase in the hydrogen leak which suggests the increased hydrogen leak would be the major cause of OCV drop in the degraded MEA [18, 30] even though the OCV drop may also be compounded by the degradation of platinum catalyst [30].

The mechanical properties of AST degraded samples have been investigated by conducting tensile traction tests [18, 19, 66]. The fracture strain is dramatically reduced in the degraded samples, for instance, the fracture strain decreases from ~160% at the beginning of the life (BOL) to ~20% at the end of the life (EOL) [19]. The loss of ductile behavior in the degraded samples reduces their capacities to resist the damage due to the plastic deformation of the membrane and increases the possibility of forming fatal damages such as pinholes. Although there is active role of chemical degradation on membrane mechanical properties, the underlying mechanism has not been established [67].

1.4. Modeling of Chemical Membrane Degradation

PEFC performance modeling has been significantly developed in the past two decades to optimize fuel cell components, design advanced water and heat management strategies etc [68] that can improve fuel cell efficiency. On the other hand, there are relatively few models published up to date to address chemical membrane degradation, although degradation models are important to identify and understand the major degradation mechanisms and to propose adequate mitigation strategies for membrane degradation.

Kinetic models [29, 43, 51, 69] have been developed to investigate ionomer degradation processes under a specific environment which is not linked with the operating fuel cell conditions. Xie *et al.* [43] developed a kinetic model to describe two ionomer degradation processes with two different initiating regions, main chain defects followed by main chain unzipping and side chain cleavage followed by side chain unzipping mechanisms, and their effects on carboxylic acid group concentration and fluoride release. Although this is the pioneer kinetic model on ionomer degradation, radical formation which determines the aggressive radical concentration in the ionomer phase was not included. Gubler *et al.* [29] modeled the $\cdot\text{OH}$, $\text{H}\cdot$, and $\cdot\text{OOH}$ concentrations by considering a set of chemical reactions including the radical formation from the decomposition of hydrogen peroxide in the presence of cationic contaminant,

CONFIDENTIAL

e.g., Fe^{2+} , radical reactions with hydrogen, oxygen, water, and hydrogen peroxide, and chemical attack on PFSA ionomer. The model concluded that the Fenton's reaction is an important source for $\cdot\text{OH}$. However, the model focused on the ionomer degradation induced by the carboxylic acid end group while the degradation induced by side chain cleavage supposed to be more dominant in stabilized PFSA ionomer membrane was ignored. This inspired Ghelichi *et al.* [51] to develop a more general ionomer degradation model to describe the degradation in stabilized PFSA type membranes including short side chain membrane. Their model suggests the side chain cleavage has a strong impact on main chain backbone scission and generates new degradable end groups on backbone which indicates that the membrane durability is highly related with the side chain stability in fuel cell environment. The kinetic models mentioned so far target the $\cdot\text{OH}$ formation and its attack on the ionomer, but kinetic model can actually be extended to discuss the mitigating effect induced by cerium ions which is widely observed under OCV AST or *ex situ* Fenton's durability conditions [53, 54, 55, 56, 57, 58, 70]. Gubler *et al.* [69] modeled the cerium ion mitigation processes by examining the chemical reaction rates between the $\text{Ce}^{3+}/\text{Ce}^{4+}$ redox couple and radicals in the membrane and concluded that the mitigation effect is based on the rapid $\cdot\text{OH}$ quenching facilitated by Ce^{3+} .

Macroscopic effects such as transport phenomena in MEA components cannot be included in the kinetic models. Therefore the interrelations between fuel cell conditions and designs and degradation processes cannot be fully addressed which limits the applicability of kinetic based membrane degradation models. MEA degradation models based on conservation laws to account for the role of transport phenomena in membrane degradation have been developed [38, 44, 71] which focuses on various aspects of transport phenomena on chemical membrane degradation. The models developed by Shah *et al.* [44] and Coulon *et al.* [71] incorporate hydrogen peroxide formation via Fenton's reaction and its transport phenomenon to provide a spatial hydrogen peroxide distribution along the through plane direction and sequentially calculate the radical formation based on the local hydrogen peroxide concentration. Shah *et al.* [44] focused on analyzing the role of hydrogen peroxide and radical in membrane degradation processes, and studied the degradation rate primarily in relation to the kinetics of both peroxide/radical formation and radical attack. On the other hand,

CONFIDENTIAL

Coulon *et al.* [71] aimed to model the impact of membrane degradation on the cell potential and membrane proton conductivity. Unlike Fenton metal ions such as iron ion which mainly accelerate chemical membrane degradation [34], Pt in the membrane (PITM) demonstrates a dual role in membrane durability, *i.e.*, catalyst to generate [37] or quench [40] $\cdot\text{OH}$. A detailed Pt pathway of radical formation is developed by Gummalla *et al.* [38] to address this dual properties of PITM by suggesting there is a nonlinear relationship between the Pt particle size and spacing in the membrane and the radical formation/quenching. Overall, the details of ionomer degradation processes were generally ignored and simplified degradation mechanisms rather than experimentally supported degradation mechanisms were considered. Recent experimental results [18, 25, 49] suggest the chemical degradation processes on the chemically stabilized PFSA ionomer involves sequential reactions which are activated by the ether bond cleavage in side chain. Simplified degradation mechanisms cannot fully address the impact of membrane degradation on the macroscopic membrane properties, for instance, the membrane thickness, degraded ionomer species concentrations, fluoride release rate etc [18]. Moreover, the transport and reaction phenomena of the metal contaminants were generally neglected in simulations, despite of their importance in chemical membrane degradation.

Chemical membrane degradation can significantly reduce membrane lifetime and also deteriorate the fuel cell performance. The performance decay due to chemical membrane degradation has been observed in terms of OCV decay and reduction in membrane proton conductivity [18, 19]. However, only the model developed by Coulon *et al.* [71] attempts to address the reduction in membrane proton concentration resulted from the side chain cleavage. Moreover, one of the most promising mitigation strategies which is the incorporation of radical quenching additives such as ceria CeO_2 into MEA have been shown to compromise the fuel cell performance [62], *e.g.*, the voltage loss in fresh BOL ceria-supported MEA can be up to 30 millivolts at current density of 1 A cm^2 . The performance drop is believed to have the same origin of the effects caused by cationic contaminants (such as iron and copper ions) which is associated with reduced proton concentration and conductivity in the membrane [63, 64, 65] since ceria can dissolve into the ionomer phase and bond to the sulfonic acid end group. In this context,

several cationic contaminant models have been developed to explore this type of degradation [72, 73, 74, 75]. Weber *et al.* [73] investigated the potassium ion transport in membrane in a hydrogen-pump setup. The simulation suggests the current densities are limited because the sulfonic acid groups are occupied by the cationic contaminants. The steady-state cationic contaminant model developed by Kienitz *et al.* [72] also suggests the current density is limited due to high contamination level. Greszler *et al.* [74] incorporated the Nernst equation to calculate the voltage loss due to the reduction in proton concentration in the ionomer membrane and suggested the proton concentration difference that develops between the anode and cathode plays an important role in the performance decay in the contaminated membranes. Serincan *et al.* [75] included the cation transport phenomena in the entire CCM and applied it to analyze the fuel cell performance when cationic contaminant continuously enters into membrane from the air stream or the fuel stream. However, no *in situ* models that describe the effects of ceria additive on the fuel cell performance have been published to date. Additionally, these models cannot be directly applied to study cerium ion transport and its impact on fuel cell performance since none of them simultaneously address the initial embedded ceria in the membrane during MEA fabrication, resulting in a fixed amount of cerium ions in the MEA, and the cerium ion transport in the CLs resulting in a significant cerium accumulation in the ionomer phase of the cathode CL [62].

1.4.1. Challenges in Modeling of Chemical Membrane Degradation

Modeling of chemical membrane degradation is challenging due to its complexity. The first difficulty is the wide range of time scales, species lifetimes, and species concentrations involved in the model. For instance, the time scale for membrane to reach its equilibrium state in humidified air is in the 100-1000 s range [76], while the time scale for membrane to reach its EOL state can be in the 10000 hour range [7]. The knowledge of the underlying degradation mechanism is also limited. As an example, the radical formation process in Pt-dispersed membrane has not been fully understood [41]. Therefore, simple and empirical relations are usually implemented in the existing degradation models. Calibration and validation are also vital in PEFC modeling, however, *in situ* measurement of hydrogen peroxide, OH radical, degraded ionomer

CONFIDENTIAL

species, degraded ionomer morphology, and parameters related with chemical membrane degradation are always challenging. Hence, parametric studies are usually conducted in the existing simulations to screen the chemical membrane degradation at different operating conditions and model parameters.

Chapter 2. Summary of Contributions

In this chapter, a summary of contributions is given. More details about the contributions are discussed in the articles attached in Appendices A to D.

2.1. Macroscopic In Situ Modeling of Chemical Membrane Degradation in Polymer Electrolyte Fuel Cells

A framework for simulating *in situ* chemical membrane degradation within an operating fuel cell is developed. The model simultaneously addresses the PFSA ionomer membrane degradation processes and transport-reaction phenomena of $\cdot\text{OH}$ and hydrogen peroxide, which are generally scrutinized separately in kinetic models [29, 43, 51, 69] and MEA models [38, 44, 71] of membrane degradation. The results simulated in the model are published in the paper attached in Appendix A [77].

2.1.1. Model Formulation and Assumptions

Assumptions

The model is 1-D MEA model, in which the important through-plane transport phenomena are considered. In-plane transport phenomena, for example, the current distribution under gas channel and plate land, are not considered. Isothermal model is assumed, and the effects of temperature distribution on chemical membrane degradation are neglected. Although liquid water transport is necessary for predicting fuel cell performance in low cell voltages, the interaction between liquid water transport and chemical membrane degradation is poorly understood and is thus neglected in the model. The chemical degradation is considered in the membrane, while the ionomer degradation in the CLs is neglected in the model since there is no clear evidence for

ionomer degradation in CLs [18]. In the model, we assume there is no Pt dissolution and migration in the CLs. Hence, the PITM and its consequences on chemical membrane degradation are neglected in the model. Continuous boundary conditions are assumed between all MEA interfaces and no contact resistances is assumed.

Modeling Domain

The developed model focuses on the ionomer degradation in the membrane but not in the CLs, because no evidence was found for the ionomer degradation in the CLs in the recent ASTs [18, 19, 40]. However, the CLs have to be included to account for the electrochemical reactions and transport phenomena that are involved in the membrane degradation, for example, hydrogen peroxide formation due to two-electron oxygen reduction reaction (ORR). Moreover, GDLs have to be included in order to address the transport phenomena within the membrane and CLs. Therefore, a macroscopic computational fluid dynamics (CFD)-based MEA model is adopted in this work to model the *in situ* chemical membrane degradation in hydrogen PEFCs.

Species of interest

In the present model, gas and electron transport is considered in GDLs and CLs, and transport in the ionomer phase is considered in the CLs and membrane. The species considered in the ionomer phase includes: dissolved hydrogen, oxygen, water, and hydrogen peroxide, and protons. In the membrane, hydroxyl radical, hydrogen radical, hydroperoxyl radical, side chain end groups (R_fSO_3), and degraded ionomer species ($R_f\alpha O \cdot$, $R_f\beta O \cdot$, R_fCOOH , HF , CF_2) are considered, and their concentrations are simulated. Description of transport phenomena (transport of mass) are based on the law for conservation of mass in combination with the constitutive relations which describe the transports of the species. Water transport in the ionomer phase is described by diffusion and electro-osmotic drag [78]. Diffusion is considered to be the main transport mechanism for non-charged species. More details about the model formulation and governing equations are given in Appendix A.

Ionomer Degradation Model

The ionomer membrane degradation model is developed based on the observations in recent experimental results in the NG-HDFC project [18, 25, 49]. Side chain cleavage is considered to initiate the overall chemical degradation processes of the chemically stabilized PFSA ionomer membrane. Further degradation on side chain is considered as an unzipping process, and continuous side chain unzipping could result in main chain degradation which is described as main chain fragmentation. In order to describe the evolution of the ionomer structure during the degradation, side chain end group (R_fSO_3) and degraded ionomer species ($R_f\alpha O \cdot$, $R_f\beta O \cdot$, R_fCOOH , HF , CF_2) concentrations simulated in the model are considered to be time dependent, which means the transient term of those species ($\frac{\partial c_i}{\partial t}$) is included in the governing equations. Those concentrations are then used to calculate metrics of degradation processes which can be characterized, and membrane morphology change due to membrane degradation is neglected. The metrics includes the membrane thickness, cumulative fluoride release, OCV, and membrane proton resistance.

2.1.2. Model Validation

The model is implemented into COMSOL, and the simulated results are demonstrated to be independent with respect to mesh size. Then, the model is applied to simulate membrane degradation in the case of a recently published COCV AST in the NG-HDFC project [18]. The COCV AST combines chemical and mechanical membrane degradation by means of a steady state OCV-hold phase to accelerate chemical degradation and periodic wet/dry cycles to apply mechanical stress [18]. A full range of diagnostic methods were applied to provide consistent and comprehensive information with respect to the membrane degradation process. This dataset is utilized here for systematic validation and demonstration of the model. The inlet hydrogen, oxygen, and water vapor concentrations, and temperature used in the simulation are based on the operating conditions applied in the COCV AST [18], and they are 60.2 mol m^{-3} , 21.3 mol m^{-3} , 15.3 mol m^{-3} , and 368.15 K , respectively. Other parameters used in the model are given in Appendix A.

CONFIDENTIAL

In general, the simulated results match the experimental trends obtained in the recent AST dataset [18] as shown in the article attached in Appendix A. The simulation of ionomer molecular structure is congruous with the experimentally observed ionomer degradation: the end of the side chain is cleaved first, followed by the side chain unzipping and release of the side chain and main chain CF chemical groups. Specifically, the simulated degradation rates of the degraded ionomer groups are compatible with the degradation rates observed in nuclear magnetic resonance (NMR) results [18], which is important for estimating the evolution of the macroscopic membrane properties with respect to fuel cell operating conditions. Membrane thinning and cumulative fluoride release are also calculated, and the results suggest the main chain degradation induced by the side chain degradation have to be considered to account for the enormous amount of material loss formed in AST measurements [18].

The model is utilized to calculate the evolution of OCV as a function of chemical membrane degradation. The OCV is calculated by considering the oxidation of hydrogen at the cathode side resulted by the hydrogen crossover from the anode side to the cathode side. The simulated OCV decay is approximately linear primarily attributed to the increase in hydrogen crossover rate due to membrane thinning. This indicates that the model can capture the effect of membrane thinning on crossover and its induced effect on the fuel cell OCV. However, since the present model is 1-D and developed to simulate global chemical membrane degradation, it does not capture in-plane spatial variations in degradation rates nor mechanical degradation responsible for the localized membrane damage (pinholes, cracks, etc.) featured in the experimental results in the AST experiment [18]. Physical membrane damage can trigger convective flux of hydrogen gas across the membrane that greatly exceeds the potential rates of pure diffusion and imposes a sizable reduction in the measured OCV, as observed in the COCV AST. Moreover, Pt degradation in the CL is feasible at OCV conditions [7], and its effects on OCV drop is neglected in the model.

The simulated evolution of membrane ionic resistance during the *in situ* degradation is calculated, and the calculation is based on the change of the volume fraction of the hydrophilic domain in the membrane and is presented in Appendix A. The

simulated result is compared to measured high frequency impedance data, which is dominated by membrane ionic resistance but also includes contributions from other components. The calculated resistance is shown to increase slightly during the preliminary stages of degradation known to be dominated by side chain degradation followed by a gentle decrease due to membrane thinning. A one-to-one comparison between the calculated resistance and the measured impedance cannot be made in this case without a detailed knowledge on the changes in membrane hydrophilic network after the chemical degradation, which is an important study and is currently investigated in the NG-HDFC project [12, 79]. Changes in the membrane morphology and microscopic charge density distribution in the ionomer, induced by the membrane degradation, alternate the water and proton transports. New models that describe water and proton transport phenomena in the degraded PFSA membrane are therefore required, which can be applied to link the chemical membrane degradation to the performance loss of the MEA.

2.1.3. Model Challenges and Opportunities

The developed model assumes the reaction rate in the membrane is second order reaction in which the rate depends on the concentrations of two first order reactants. However, the sensitivity of this system of reactions upon membrane structure has not been fully examined. Further NMR experiments and more results are required to determine the reaction orders of ionomer degradation processes. Several parameters are highly related with the degradation rates, for instance, the oxygen diffusivity in the ionomer phase, the rate of decomposition of hydrogen peroxide by Fe^{2+} and etc. The sensitivity analysis of these parameters can be conducted by applying the developed model to estimate their adequate ranges and to quantify their relative importance. Further experiments can be conducted for determining the temperature and water content dependence of the parameters with higher priorities. Moreover, the influences of chemical membrane degradation on these parameters should be addressed, which is considered as a future work.

CONFIDENTIAL

Binary friction membrane model (BFM2) [80] is applied in the developed model to calculate the water diffusivity and proton conductivity in the membrane. BFM2 was developed in order to provide more consistent water and proton transport over the entire range of water contents and at different temperatures for a BOL membrane. Hence, the influences of membrane morphological changes due to chemical degradation were not addressed in BFM2. A new model for coupled proton and water transport in the degraded membrane is required.

Thin-film catalyst model is applied in the model to calculate the HOR, 2e ORR, and 4e ORR in the catalyst layers. The reactant concentration in the gas phase is applied to calculate the electrochemical reaction rate. In the anode catalyst layer, the oxygen concentration in the ionomer phase sharply drops near the CCL and membrane interface, while the oxygen concentration in the gas phase is more uniform than in the ionomer. Therefore, a better prediction can be achieved by using the oxygen concentration in the ionomer phase to calculate the ORR rate in the anode catalyst layer.

2.2. Mitigation of Chemical Membrane Degradation in Fuel Cells: Understanding the Effect of Cell Voltage and Iron Ion Redox Cycle

In the previous section, the transport-reaction phenomena of membrane contaminant are not considered, and the concentration of the contaminant is assumed constant. The 1-D model developed in the previous section is extended to include the transport-reaction phenomena of $\text{Fe}^{2+}/\text{Fe}^{3+}$, and the role of transport-reaction phenomena of $\text{Fe}^{2+}/\text{Fe}^{3+}$ is investigated. The results simulated in this model are published in the paper attached in Appendix B [81].

2.2.1. Membrane Contaminants and Additives

Hydroxyl radicals can be generated from decomposition of hydrogen peroxide caused by cationic contaminants such as Fe^{2+} and Cu^+ [30, 34]. Among these contaminants, the ferrous ion (Fe^{2+}) is found to have the highest impact on the rate of chemical degradation [34]. Therefore, iron ions (ferrous/ferric ion couple) are first considered in the chemical membrane degradation model developed and presented in the journal paper attached in Appendix B.

Due to the mobility of iron ions and high ionic conductivity of the membrane, ion migration is an important transport mode expected to depend on the cell voltage. Therefore, Nernst-Planck equation is adopted here to describe the transport phenomena of iron ions in the ionomer phase:

$$J_i = -D_i \nabla c_i - u_i z_i c_i F \nabla \phi_e, \quad (1)$$

where the first term represents diffusion due to the concentration gradient and the second term represents migration due to the ionomer potential gradient across the electrolyte. Convective ion transport due to dissolved water crossover in the electrolyte is neglected. In addition, the iron redox chemistry which involves the electrochemical oxidation and reduction at the active surface area of Pt in CLs are considered and governed by Butler-Volmer kinetics.

The total initial amount of the iron ion is around 30 ppm, which is conserved during the simulation. The simulated degradation rate is a function of the initial amount of the iron ion, and faster degradation is simulated as the initial amount is increased.

2.2.2. PFSA Ionomer Degradation

The PFSA ionomer degradation model applied in this section is developed based on the previous model used in Appendix A. Continuous backbone unzipping resulting in the loss of small side chain fragments is considered to advance the previous model. The details of the model such as the kinetic equations and the parameters used in the model are presented in the paper attached in Appendix B.

2.2.3. Open Circuit Voltage

A standard AST protocol for chemical membrane degradation was established by the US Department of Energy (DOE) [82]. Fuel cell is usually operated at OCV or high cell voltage which can significantly promote the chemical degradation [18, 83]. Although the dramatic degradation rates observed in this test have been tentatively attributed to the high gas crossover under OCV conditions [1], the mechanisms involved have not been fully established. In the present work, the *in situ* chemical degradation process under OCV condition in the NG-HDFC project is first examined in terms of the ferrous ion, ferric ion, and hydrogen peroxide concentrations which are involved in hydroxyl radical formation. Other inlet operating conditions used in the simulation are also based on the conditions applied in the COCV AST [18].

In hydrogen PEFCs, the Fe^{2+} ion can be electrochemically generated from Fe^{3+} via the ferric/ferrous redox reaction at the anode CL, where the potential is near zero which is considerably negative of the redox potential for promoting the reduction of Fe^{3+} to Fe^{2+} . On the other hand, the Fe^{2+} ion is expected to be electrochemically oxidized to Fe^{3+} when exposed to high potentials on the cathode (the simulated cathodic potential is around 1 V when the cell is held at OCV). This situation gives rise to a $\text{Fe}^{2+}/\text{Fe}^{3+}$ ion concentration gradient across the membrane. In the anode CL where Fe^{3+} is reduced, a near-zero Fe^{3+} concentration and a high Fe^{2+} concentration are obtained. Meanwhile, Fe^{2+} is oxidized in the cathode CL, resulting in a near-zero Fe^{2+} concentration and a high Fe^{3+} concentration. The dominant presence of Fe^{3+} in cathode CLs has been reported [84].

CONFIDENTIAL

When the cell is held at OCV, ion migration due to the ionomer potential gradient is negligible, and hence diffusion is the dominant mode of ion transport between anode and cathode CLs that drives Fe^{2+} from anode to cathode and Fe^{3+} from cathode to anode. The Fe^{2+} ion is formed in the anode CL and diffuses into the membrane where it may react with H_2O_2 , $\cdot\text{OOH}$, and $\cdot\text{OH}$ along its path to the cathode. In the simulation, Fe^{2+} is not fully reacted in the membrane and can reach the cathode CL for oxidation. Similarly, the Fe^{3+} ion formed in the cathode CL diffuses into the membrane and onwards to the anode as indicated by the insignificant consumption rate in the membrane. Therefore, almost all Fe^{3+} formed in the cathode CL reaches the anode CL where it is reduced back to Fe^{2+} . Since zero fluxes are assumed at the MPL and CL interfaces, a redox cycle of iron is established in the MEA due to the conservation of species and charge. This demonstrates the decisive effect of the $\text{Fe}^{2+}/\text{Fe}^{3+}$ redox reaction on the distribution of $\text{Fe}^{2+}/\text{Fe}^{3+}$ in the MEA and the importance of including the $\text{Fe}^{2+}/\text{Fe}^{3+}$ redox chemistry. This iron ion redox cycle preserves a relatively high ferrous ion concentration in the membrane, which leads to the most severe chemical membrane degradation through the Fenton mechanism. This result provides fundamental evidence for the empirical rationale of using OCV conditions to accelerate the chemical membrane degradation in various ASTs [18, 82].

Besides the ferrous ion, hydrogen peroxide is also required for hydroxyl radical formation, and hence its concentration is also simulated. The anodic potential is near zero which is favorable for hydrogen peroxide formation due to two-electron ORR [85]. Therefore, a higher H_2O_2 concentration in the membrane near the anode CL is obtained. With the higher concentrations of Fe^{2+} and H_2O_2 , hydroxyl radicals are preferentially formed in the membrane near the anode CL, and hence the chemical degradation and associated reduction in sulfonic acid group concentration is faster near the anode CL, as confirmed experimentally in a recent reinforced membrane AST in the NG-HDFC project.

2.2.4. Below Open Circuit Voltage

Since iron ions are mobile and positive charge species, their distribution inside the PEFC are found highly sensitive to the applied cell voltage and play an important

CONFIDENTIAL

role in the overall degradation process. When the cell voltage is held under OCV, an ionomer potential gradient across the cathode CL, membrane, and anode CL is formed due to the regular electrochemical reactions in hydrogen PEFCs. The obtained ionomer potential decreases from the anode CL to the cathode CL which results in migration of positively charged species, including protons, Fe^{2+} ions, and Fe^{3+} ions, from the anode CL to the cathode CL across the membrane. The Fe^{3+} ion migration towards the cathode CL counteracts its diffusive transport and thereby results in a smaller Fe^{3+} flux towards the anode CL. Hence, Fe^{3+} is found to accumulate at the cathode CL. The smaller Fe^{3+} flux towards the anode CL also limits the iron ion reduction in the anode CL. Because the $\text{Fe}^{2+}/\text{Fe}^{3+}$ redox reaction is the dominant source of Fe^{2+} in the MEA, this situation suppresses the Fe^{2+} formation in the redox cycle of iron which gives rise to a lower fraction of Fe^{2+} in the membrane when compared to the OCV condition. For example, there is a dramatic decrease (-93%) in membrane Fe^{2+} ion concentration when the cell voltage is decreased from OCV to 0.7 V which is a consequence of the increased ion migration flux as identified previously. When the cell voltage is below 0.7 V, the concentration is further decreased to less than 5% of the value at OCV due to the iron ion accumulation in the cathode CL. These results demonstrate that the cell voltage has a significant effect on the Fe^{2+} concentration in the membrane.

The simulated degradation rate exhibits an exponential decay that is similar in nature to the underlying exponential decay in Fe^{2+} concentration, although the decay rate is further compounded by the moderate reduction in hydrogen peroxide concentration. When the cell voltage is decreased from OCV to 0.7 V, the membrane transitions from a severe degradation state to a modest degradation state (10-fold reduction in fluoride loss at 0.7 V) which is chiefly attributed to the critical reduction in the Fe^{2+} present in the membrane. This finding is consistent with and provides a theoretical understanding of the exponential dependence between degradation rate and current density observed experimentally during *in situ* testing [86]. As the cell voltage is further decreased below 0.7 V, the simulated degradation rate is essential negligible since there is insignificant Fe^{2+} in the membrane to catalyze the formation of hydroxyl radicals.

The degradation profile is also found dependent to the strength of iron ion redox cycle. When the redox cycle is strong, more ferrous ions are accumulated in the membrane near the anode CL leading hydroxyl radicals are preferentially formed there. On the other hand, when the strength of redox cycle is reduced at lower cell voltages, more ferrous ions are located in the membrane near the cathode CL. This results in the shift of faster degradation zone from the anode to the cathode side.

2.2.5. Further Discussion

The underlying ion migration in PEFCs is expected to have similar effects on the distribution of other membrane contaminants, for instance, $\text{Cu}^+/\text{Cu}^{2+}$ couple, which also promote the Fenton reaction [34]. The standard electrode potential of $\text{Cu}^+/\text{Cu}^{2+}$ couple is 0.159 V, which is higher than the cell potential at the anode CL (similar to the case in iron ion couple). It is expected that an ion redox cycle is formed at the higher cell voltages which maintains a relatively high Cu^+ for membrane degradation. The strength of the cycle is also expected to be reduced in the low cell voltages due to the ion migration. Overall, the degradation related with $\text{Cu}^+/\text{Cu}^{2+}$ couple is expected to have similar cell voltage dependence to $\text{Fe}^{2+}/\text{Fe}^{3+}$ couple, *i.e.*, the degradation rate reduces with decreasing cell voltage. Therefore, the mitigation effect due to reduced cell voltage suggested in this section is expected to be generally applicable for PEFC operation.

In the model, constant $\text{Fe}^{2+}/\text{Fe}^{3+}$ mobility is applied. Since the mobility can depend on the temperature, water content, and $\text{Fe}^{2+}/\text{Fe}^{3+}$ concentration in the membrane, it is important to conduct a sensitivity analysis on the mobility to determine its role in iron ion transport in the membrane and in the chemical membrane degradation.

2.3. In situ modeling of chemical membrane degradation mitigation in ceria-supported fuel cells

Cerium ions are considered to be one of the most effective $\cdot\text{OH}$ scavengers, and thus they are used to protect the membrane from chemical degradation due to $\cdot\text{OH}$ attack. Although it is known that cerium ions can prevent chemical membrane degradation at OCV conditions [57], its effectiveness during fuel cell duty operation has not been evaluated. Therefore, chemical mitigation induced by the cerium additives are simulated based on the conditions applied in the COCV AST under various cell voltages, and the details of the results are reported in the paper attached in Appendix C. In this section, a brief presentation is given.

2.3.1. Open Circuit Voltage

Radical scavenging is proposed to mitigate the chemical damage by quenching the radicals before they attack the ionomer membrane. One of the most promising additives to quench $\cdot\text{OH}$ in fuel cells is CeO_2 , which can effectively protect the ionomer membrane under OCV conditions [53, 55, 56, 57].

The cumulative fluoride release in the baseline and ceria-supported MEAs as a function of operational time at OCV based on the proposed model is simulated. The simulated results are compared and evaluated against measured data from COCV AST experiments [57]. The proposed model successfully simulates the significant mitigating effect found in the ceria-supported MEA, which is illustrated by the coinciding fluoride emission trends of the simulated and experimental data in both baseline and ceria-supported MEAs.

In the ceria-supported MEA, the $\cdot\text{OH}$ formation rate is 14% lower than that in the baseline MEA because of the hydrogen peroxide quenching provided by Ce^{4+} . Unfortunately, this difference is not significant enough for resolving the enormous reduction in the membrane degradation rate, and hence the lower $\cdot\text{OH}$ formation rate could not be the primary mitigating mechanism produced by the ceria additive.

CONFIDENTIAL

Instead, it is found that the chemical stabilization mechanism is highly related with the suppression of ionomer damage due to $\cdot\text{OH}$ attack. In the baseline MEA, the damage rate is almost two orders of magnitude higher than in the ceria-supported MEA because about 93% of the $\cdot\text{OH}$ reacts with the ionomer. On the other hand, once ceria is introduced in MEA, only 1% of $\cdot\text{OH}$ attacks the ionomer due to almost all $\cdot\text{OH}$ formed are quenched by Ce^{3+} before they can attack the membrane. The fast $\cdot\text{OH}$ scavenging by Ce^{3+} therefore represents the principal mitigating mechanism provided by the ceria additive.

In hydrogen PEFCs, electrochemical reduction of Ce^{4+} via the $\text{Ce}^{3+}/\text{Ce}^{4+}$ redox reaction is favorable at the anode and cathode CLs. Hence, Ce^{4+} can be efficiently reduced in the anode and cathode CLs by hydrogen and water, respectively [23]. As a result, Ce^{3+} is the dominant oxidation state in the CLs. In the membrane, it is found that Ce^{4+} can effectively be reduced back to Ce^{3+} by hydrogen peroxide which is continuously generated in the MEA via the two-electron ORR. Overall, Ce^{3+} is predominant in MEA.

2.3.2. Below Open Circuit Voltage

During duty operation, fuel cells are normally operated below OCV in order to generate power for practical purposes. The cell voltage is therefore an important parameter for evaluating the chemical stabilization of the membrane. The effectiveness of the ceria additive on mitigating chemical degradation under practical fuel cell operating voltages is thus explored in this section.

In the baseline MEA, the simulated fluoride emission rate (FER) decreases with decreasing cell voltage which is attributed to the reduced magnitude of the iron redox cycle and hydrogen peroxide concentration within the MEA leading to a lower $\cdot\text{OH}$ formation rate. Generally, the ceria-supported MEA has a lower simulated FER than the baseline MEA. Interestingly, the FER increases when the cell voltage decreases from OCV to 0.6 V and then levels off, which is in stark contrast to the decreasing FER trend of the baseline. The FER differential between the ceria-supported and baseline MEAs is thus descending rapidly with decreasing cell voltage from OCV to 0 V, which suggests

CONFIDENTIAL

that the ceria additive provides the strongest mitigation at OCV, but its strength cannot be sustained when the cell voltage is held below OCV.

The simulated scavenging ratio decreases significantly when the cell voltage is reduced from OCV, revealing that fewer $\cdot\text{OH}$ are quenched by Ce^{3+} . More $\cdot\text{OH}$ are then available to attack the ionomer in the membrane. When the cell voltage is below OCV, Ce^{3+} still prevails in the membrane because Ce^{4+} can be effectively reduced to Ce^{3+} by hydrogen peroxide in the membrane or via the redox reaction in both CLs. Since zero fluxes are assumed at the MPL and CL interfaces, the total amount of Ce^{3+} is therefore stable in the MEA with respect to changes in cell voltage. On the same token, the reduction in the total amount of Ce^{3+} due to oxidation or leakage is found to not be an appropriate mechanism for the drop in $\cdot\text{OH}$ scavenging rate.

The significant reduction in the mitigation effectiveness and the increased FER observed in the ceria stabilized MEA are in fact highly related to the Ce^{3+} distribution in the MEA rather than the total amount of Ce^{3+} present. When the cell is held at OCV, there is no current or ionomer potential gradient across the MEA. Ion migration due to the ionomer potential gradient is therefore negligible, and diffusion is the dominant mode of cerium ion transport between anode and cathode CLs. Diffusion drives Ce^{3+} from high concentration to low concentration, and hence a uniform equilibrium distribution in the MEA is formed. The stable Ce^{3+} supply in the membrane secures the $\cdot\text{OH}$ scavenging which results in the strongest mitigation observed at OCV.

When the fuel cell is operated at cell voltages below OCV, an ionomer potential gradient across the MEA is formed by the regular electrochemical reactions in hydrogen PEFCs. The obtained ionomer potential decreases from anode to cathode. As Ce^{3+} is a positively charged species, it migrates from the anode CL to the cathode CL across the membrane. This Ce^{3+} ion migration leads to considerable Ce^{3+} accumulation in the cathode CL.

When the cell voltage is reduced from OCV to 0.5 V, the ionomer potential gradient across the membrane increases dramatically due to the faster HOR and four-

electron ORR. The resulting potential gradient drives more Ce^{3+} from the membrane to the cathode CL, and thereby the Ce^{3+} concentration in the membrane is largely reduced. Without enough Ce^{3+} in the membrane, the influence of $\cdot\text{OH}$ scavenging is diminished, and thereby the mitigation effectiveness indicated by the ratios of the FER and membrane thinning rate of the baseline MEA to those of the ceria-supported MEA are largely suppressed. For example, a ten-fold reduction in mitigation effectiveness is simulated under low cell voltages ($V < 0.7$ V). Therefore, a close correlation between the observed trends in reduced mitigation effectiveness and the reduced Ce^{3+} concentration in the membrane is found at these cell voltages.

A near zero Ce^{3+} membrane concentration is obtained when the cell voltage is held at 0.5 V, which suggests that further reductions in cell voltage may have limited effect. Indeed, the Ce^{3+} membrane concentration almost levels off even when the cell voltage is further decreased from 0.5 V to 0 V. The corresponding mitigation effect at low cell voltages is thus relatively constant and insignificant compared to the cases at high cell voltages. Fortunately, the overall rates of chemical degradation at these cell voltages are substantially lower than those at OCV conditions as discussed in the previous section. Therefore, although the mitigation effects are insignificant, the FERs are considerably lower than those at OCV conditions without ceria additive.

2.4. Simulation of Performance Tradeoffs in Ceria Supported Polymer Electrolyte Fuel Cells

Ceria-supported MEAs can effectively protect the membrane at OCV conditions; however, performance tradeoffs have been observed experimentally with the use of membrane additives [62]. In this section, a comprehensive, transient *in situ* membrane durability model for ceria-supported MEAs is developed and applied to investigate the fundamental mechanisms of the performance tradeoffs. A brief summary is presented in this section, and the details of the simulation results are given in Appendix D.

2.4.1. Model Assumptions

The model simulating the mitigating effect of ceria-supported MEA is the previous section is extended to capture the proton diffusion. In order to solve all the species of interest in the model, principle of electroneutrality is assumed. Moreover, the change in ionomer structure due to cerium ion exchange is neglected.

2.4.2. Beginning of Life (BOL) MEA Performance

Lower fuel cell performance in ceria-supported MEA is found from 0.9 V to 0.6 V, which represents the usual operating cell voltages in fuel cell applications in which kinetic and ohmic losses are dominant. The simulated voltage loss is compared to the experimental results [62], and the simulated result successfully predicts the magnitude of the voltage loss within a few millivolts and captures the increasing trend of the voltage loss with operating current density. The results confirm that the ceria additive has negative impact on fuel cell performance, and that the impact becomes more severe at higher current densities.

When the cell voltage is held below OCV (the simulated OCV is ~ 1.0 V), an ionomer potential gradient across the cathode CL, membrane, and anode CL is formed due to the regular electrochemical reactions in hydrogen PEFCs. The obtained ionomer potential decreases from the anode CL to the cathode CL, which results in migration of positively charged species, including protons, $\text{Ce}^{3+}/\text{Ce}^{4+}$ ions, and $\text{Fe}^{2+}/\text{Fe}^{3+}$ ions, from the anode CL to the cathode CL across the membrane. Since transport of Ce^{3+} ions across the MPL-CL interfaces is neglected, Ce^{3+} is accumulated at the cathode CL. As the cell voltage decreases, *e.g.*, from 0.8 V to 0.6 V, the ion migration becomes more dominant because the ionomer potential gradient increases due to the enhanced HOR and four-electron ORR. The simulated Ce^{3+} accumulation at the cathode CL consequently becomes more severe at lower cell voltages. Due to the electroneutrality condition, *i.e.*, $c_{\text{H}^+} + 3 c_{\text{Ce}^{3+}} \approx c_{\text{SO}_3}$, the increase in Ce^{3+} concentration results in a three times more significant reduction in proton concentration ($\Delta c_{\text{H}^+} \approx -3 \Delta c_{\text{Ce}^{3+}}$). Hence, a

CONFIDENTIAL

notable reduction in local proton concentration is observed in the cathode CL when the Ce^{3+} concentration is high, as in the case of 0.6 V.

The proton starvation leads to low four-electron ORR rate and low proton conductivity in the cathode CL which results in sizable kinetic and ohmic performance losses for the ceria-supported MEA. In general for the ceria-supported MEAs, the obtained proton conductivity in the cathode CL is lower than in the anode CL and membrane, which is also supported by the high cathode CL ionic resistance measured experimentally [62]. The low conductivity is attributed to the low proton concentration because of the Ce^{3+} accumulation, since the proton conductivity is proportional to the proton concentration according to the Nernst-Planck equation [75]. As the cell voltage is decreased from 0.8 to 0.6 V, the decay in proton concentration counteracts the increase in water content, leading to a reduction in proton conductivity. The poor proton conductivity results in an additional ohmic resistance in the ceria-supported MEA, and the corresponding ohmic loss is increased with current density.

The rate of the four-electron ORR is not uniform across the cathode CL with the peak ORR rate is obtained near the CL-membrane interface in the baseline MEA. The higher ORR rate is due to the more negative overpotential because of the more positive ionomer potential near the CL-membrane interface. When the ceria additive is introduced into the MEA, the ORR rate becomes more uneven. The lack of protons near the cathode CL-MPL interface hinders the ORR rate because the proton, which is required for the four-electron ORR, is absent in the ionomer phase even though the oxygen concentration and overpotential are comparable to the baseline MEA. In order to generate the same current density as for the baseline MEA, a lower cathode potential is required to achieve a more negative overpotential to compensate for the effect of proton starvation. This is the source of the kinetic loss that contributes to the performance tradeoff.

2.4.3. Membrane Durability and Fuel Cell Performance

The voltage losses predicted for ceria-supported MEAs are expected to counteract the durability benefits and may possibly even outweigh the motivation for the use of radical scavengers unless care is taken to analyze the interplay between membrane stability and MEA performance. The MEA performance decay due to the presence of ceria additive is mainly attributed to the cerium accumulation in the cathode CL under nonzero current densities. This accumulation could potentially be mitigated by increasing the ionomer loading in the CL or decreasing the ceria additive loading in the MEA. In this section, the effects of the ionomer and ceria additive loadings on the performance and durability combination are therefore addressed.

In general, the simulated results indicate that the negative performance impact can be partially mitigated when the ionomer loading is increased or the ceria additive amount is decreased in the BOL MEA. The obtained improvements are attributed to the reduction in local Ce^{3+} concentration in the cathode CL. For example, when the initial Ce^{3+} loading is reduced from 100 to 25 mol m^{-3} , it is clear that the Ce^{3+} accumulation is also reduced. The corresponding proton conductivity in the ionomer phase of the cathode CL is increased when the initial cerium ion concentration is reduced from 100 to 25 mol m^{-3} . The reduction in Ce^{3+} concentration also increases the ORR rate in the cathode CL, which leads to a reduction in the kinetic voltage loss.

An increase in the ionomer loading of the cathode CL reduces the Ce^{3+} accumulation in the cathode CL because higher ionomer loading can reduce the local concentration. Hence the diminished simulated proton conductivity of the cathode CL increases with increasing ionomer volume fraction. Moreover, with less cerium ion interference at the cathode, the kinetic voltage loss associated with the ORR is also reduced.

The initial Ce^{3+} concentration and ionomer loading could be optimized to mitigate the performance decay observed in the ceria-supported MEAs. For the optimization of the initial Ce^{3+} concentration, the most critical concern is the mitigation effectiveness of

CONFIDENTIAL

the chemical membrane degradation, which may otherwise cause lifetime-limiting hydrogen leaks across the membrane [57]. The cumulative fluoride loss is therefore simulated as a function of initial Ce^{3+} concentration under accelerated conditions for chemical membrane degradation at OCV [57]. As expected, the results demonstrate that the fluoride release rate increases with decreasing Ce^{3+} concentration. Fortunately, the fluoride release is less sensitive at higher concentrations which was also observed with ceria-supported MEAs subjected to the *ex situ* Fenton's durability test [54]. For example, when the initial concentration of cerium ion decreases from 50 mol m^{-3} to 25 mol m^{-3} , the total fluoride loss increases by 0.29 mol m^{-2} which is almost 10x higher than the increase of fluoride loss when the concentration decreases from 100 mol m^{-3} to 75 mol m^{-3} . This property of the ceria additive makes it feasible to reduce the additive loading while still achieving a desirable mitigation of chemical membrane degradation. For instance, approximately 40x reduction in the fluoride emission rate can be achieved with a mere initial Ce^{3+} concentration of 50 mol m^{-3} .

As a potential power source, however, fuel cells are normally operated below OCV to provide power during duty operation. The mitigation effectiveness is therefore more important under realistic operating conditions than for idle OCV conditions. The cumulative fluoride release of MEAs with various initial cerium ion loadings is hence simulated at 0.8 V. In general, the fluoride release is less sensitive to the initial Ce^{3+} concentration when compared to the OCV condition. This suggests that the performance tradeoff can be minimized without compromising membrane durability by reducing the initial Ce^{3+} concentration from 100 to 50 mol m^{-3} , which was also observed to be acceptable under the more stressful OCV condition. On the other hand, the durability mitigation effectiveness of ceria is slightly reduced at 0.8 V compared with the effectiveness simulated at OCV. The reduction in effectiveness is related with the cerium ion accumulation in the cathode CL which results in a lower Ce^{3+} concentration in the membrane that reduces the $\cdot\text{OH}$ quenching rate, as discussed in the previous section. Moreover, the proton starvation near the cathode CL-MPL interface reduces the current density due to the kinetic and ohmic losses. This results in less negative ionomer potential in CCL with increasing the ceria loading. Since the overpotential for $\text{Fe}^{2+}/\text{Fe}^{3+}$ couple is calculated by: $\eta = \phi_s - \phi_e - 0.695$, where ϕ_s and ϕ_e are local potential of solid

CONFIDENTIAL

carbon and ionomer, the calculated overpotential becomes more negative with increasing ceria loading which is favor for Fe^{3+} reduction. Therefore, the amount of harmful Fe^{2+} increases with ceria loading, which results in a higher remaining Fe^{2+} concentration in the membrane. The simulated results indicate that the addition of 100 mol m^{-3} ceria can effectively double the iron ion concentration in the membrane under these conditions.

When the cell voltage is further reduced to 0.6 V, the cerium ion accumulation at the cathode CL becomes more significant due to the enhanced ORR, in which the current densities increased from $\sim 0.23 \text{ A cm}^{-2}$ at 0.8 V to 0.85 - 1.0 A cm^{-2} at 0.6 V under the present conditions. This effect magnifies the influence of the ceria loading on the ionomer potential gradient and the Fe^{2+} concentration in the membrane. The ceria induced increase in Fe^{2+} concentration in the membrane is notable, in contrast to the baseline MEA without ceria which had essentially zero iron ion concentration in the membrane at this cell voltage. This alters the chemical membrane degradation rates quantified by the simulated fluoride release, even to the extent where a ceria-supported MEA may have a *higher* degradation rate than the ceria-free baseline MEA. At this cell voltage, the baseline MEA is therefore deemed to have the best overall durability and performance combination since it has a membrane durability equivalent to the MEA with 50 mol m^{-3} ceria without the associated performance tradeoffs.

Overall, the simulated results demonstrate that an optimized ceria loading can successfully provide MEA durability management at high cell voltages in terms of enhanced membrane durability and MEA performance stability. However, this approach becomes more convoluted at low cell voltages. The role of the cathode CL is more critical at low cell voltages because of cerium ion accumulation, which suggests that both performance and durability issues should be addressed simultaneously in the engineering design of the cathode CL. Based on the present simulation results, joint optimization of the ionomer volume fraction in the cathode CL and the ceria additive loading could be feasible in order to enhance the overall MEA durability across the entire range of cell voltages.

Chapter 3. Conclusions and Future Research

The work presented in this thesis addresses perfluorosulfonic acid (PFSA) membrane degradation by developing an *in situ* chemical degradation model in hydrogen polymer electrolyte fuel cells (PEFCs). The model is developed under the support of recent experimental findings suggesting PFSA ionomer degradation through a series of linked chemical degradation events during operation of PEFCs. The net action of the overall degradation mechanism is simulated using a 1-D membrane electrode assembly (MEA) based modeling framework that allowed multiscale coupling between microscopic phenomena such as radical attack and ionomer degradation processes and macroscopic attributes such as transport phenomena of iron ions and cerium ions, which are significantly related with membrane degradation and mitigation strategies. The model demonstrates the capability to simulate the evolution of ionomer molecular structure and various degradation metrics in good overall agreement with measured degradation rates in AST, which is indicated by the thinning rate of the membrane, the fluoride release rate, and the reduction in sulfonic acid group in the membrane.

Interrelated effects of damaging cations (*e.g.*, $\text{Fe}^{2+}/\text{Fe}^{3+}$) and assisting cations (*e.g.*, $\text{Ce}^{3+}/\text{Ce}^{4+}$) transport-reaction phenomena on the chemical membrane degradation and mitigation strategies are generally neglected in the membrane degradation research. Their roles in membrane degradation are investigated by applying the developed model and shown to play key roles in the overall degradation process. The state and distribution of reactive iron ions inside the PEFC are found to highly sensitive to the applied cell voltage. An iron ion redox cycle is generated in the MEA to preserve a relatively high Fe^{2+} concentration in the membrane at high cell voltages such as open circuit voltage (OCV). The magnitude of the redox cycle is shown to be strongest which probably lead to the most severe chemical membrane degradation through the OH radical formation due to the decomposition of hydrogen peroxide by Fe^{2+} in the

CONFIDENTIAL

membrane at OCV conditions. When the cell voltage is reduced, the redox cycle is weakened because of the ion migration suppressing the iron ion reduction in the anode CL through the iron ion accumulation in the cathode CL. The resulted Fe^{2+} concentration in the membrane is therefore decreased exponentially as the cell voltage is reduced. Without this active metal-ion catalyst, the harmful hydroxyl radical formation is greatly suppressed, which elucidates the mitigating effect of reduced cell voltage on the chemical membrane degradation. The simulated tenfold reduction in the cumulative fluoride release suggests that intermediate cell voltage operation provides a practical mitigation strategy for chemical membrane degradation through the Fenton mechanism, which is common and cannot be effectively eliminated in PEFCs.

The *in situ* chemical stabilization mechanism of ceria-supported MEAs in hydrogen PEFCs was investigated. The majority state of the cerium ions are found to be the desired Ce^{3+} oxidation state, which is a combined result of hydrogen peroxide supported regeneration of Ce^{3+} in the membrane and electrochemical regeneration of Ce^{3+} in CLs by hydrogen (in anode) and water (in cathode). These continuously regenerations mitigate the overall chemical degradation in ceria stabilized MEAs by supplying Ce^{3+} ; however, they are not stabilized in the membrane across the entire range of cell voltages. When the cell voltage is held at high cell voltages, Ce^{3+} is more uniformly distributed in the ionomer phase of the MEA and thus maintains a high Ce^{3+} concentration in the membrane. Despite the high Fe^{2+} concentration in the membrane at high cell voltages, abundant Ce^{3+} ions are available in the membrane to quench OH radical leading an effective protection of the membrane. When the cell voltage is decreased, most of the Ce^{3+} migrate into the cathode CL due to the ion migration, and the remaining Ce^{3+} concentration in the membrane is found to decrease exponentially. Without an adequate amount of Ce^{3+} in the membrane, the protection is significantly reduced at low cell voltages due to the suppression in the OH radical scavenging. The simulated ten-fold reduction in mitigation effectiveness is found under low cell voltages ($V < 0.7 \text{ V}$).

The tradeoff between the membrane durability and fuel cell performance in ceria-supported MEAs was analyzed by extending the developed model to include proton

diffusion and effects of proton distribution in MEAs on PEFCs. The cathode CL of ceria-supported MEAs is found to experience proton starvation due to cerium ion migration across the membrane. The inadequate supply of protons in the ionomer phase of the cathode CL reduces the proton conductivity as well as the oxygen reduction reaction kinetics, which contributes to the performance tradeoff in terms of ohmic and kinetic voltage losses. Increased ionomer volume fraction in the cathode CL and reduced Ce^{3+} concentration in the MEA are found to be effective strategies to reduce the performance tradeoffs in ceria stabilized MEAs. Overall durability management is shown to be possible at high cell voltages by optimizing the ceria loading in the MEA; however, at low cell voltages additional steps must be taken to achieve a useful combination of membrane durability and cathode CL performance stability in order to address proton starvation in the cathode CL without compromising membrane durability. The drops in FC performance due to cerium ion accumulation in the cathode CL at low cell voltages suggests that the membrane durability and CL performance stability ought to be jointly addressed by optimization of the MEA design.

3.1. Challenges and Opportunities

The developed membrane durability model is based on MEA performance model in order to associate with the transport phenomena in PEFCs. The most recent developments in MEA performance model can be adopted and applied to improve the predicted capability of the present model. Mesoscale modeling of MEA components such as GDL substrate and CL provides a better understanding on the morphology of those media. For example, stochastic microstructural modeling [87, 88] and 3-D image based morphological characterization [89] have been applied to reconstruct and characterize a realistic 3-D structure of carbon fiber paper based GDL substrate in PEFCs. A reconstruction of CL is also achieved based on 3-D dual-beam FIB/SEM characterization [90]. Those recent developments provide a practical dataset of transport parameters for PEFCs which can be adopted in the developed model for achieving

CONFIDENTIAL

realistic distribution of reactants and water (dissolved water, liquid water, and water vapor) in PEFCs, and sequentially realistic current density distribution in MEAs.

Several assumptions applied in the model could be relaxed in order to achieve a better predicted capacity. For instance, heat transfer and two-phase water transport can be included to describe temperature and liquid water saturation variations which can have important influences in the rate of local electrochemical reactions in the CLs and the rate of local chemical reactions in the membrane. The present model focuses on the chemical membrane degradation in a fresh MEA in which the radical formation is originated from the Fenton reaction. However, the radical formation from the Pt in the membrane could be important in CL degraded MEAs. However, the exact distribution and form of Pt in the membrane during MEA operation have not yet been fully addressed. Developing a model to account for Pt transport in MEA could be useful in determining the role of Pt in chemical membrane degradation.

The present model is 1-D and developed to simulate global chemical membrane degradation, it does not capture in-plane spatial variations in degradation rates nor mechanical degradation responsible for the localized membrane damage (pinholes, cracks, etc.) featured in the experimental results [18, 19]. For example, the variations in current distribution and ionomer potential gradient due to non-uniformity of membrane and CLs thicknesses and non-uniformity of reactant distribution in gas channel and land could result in variation of local degradation rates. This suggests the present model should be extended to 2-D/3-D in order to include in-plane spatial dimensions which makes the integration of finite element based mechanical models [14, 15] feasible to simulate the distribution of mechanical stress in the membrane as a function of dynamic change in operating conditions.

The present model is validated with experimental data and focuses on the influences of cell voltage on membrane chemical degradation; however, it is also important to explore the range of model validity by simulating and analyzing a comprehensive set of operating conditions, for instance, temperature, oxygen concentration, and relative humidity.

CONFIDENTIAL

Recent *in-situ* accelerated stress test data suggest that coupled chemical and mechanical degradation is the dominant degradation process during membrane fracture initiation and propagation which leads to *in-situ* membrane failures [18]. Without a coupled durability modeling approach to integrate the chemical and mechanical degradation processes, it is very challenging to accurately predict the lifetime of the MEA. However, there is still a considerable gap in the scientific literature on the development of coupled membrane durability models. Modeling of the coupling effects of chemical and mechanical degradation would be a significant future work.

References

- [1] M. P. Rodgers, L. J. Bonville, H. R. Kunz, D. K. Slattery and J. M. Fenton, "Fuel Cell Perfluorinated Sulfonic Acid Membrane Degradation Correlating Accelerated Stress Testing and Lifetime," *Chemical Reviews*, vol. 112, no. 11, pp. 6075-6103, 2012.
- [2] C. S. Gittleman, F. D. Coms and Y. -H. Lai, "Membrane Durability: Physical and Chemical Degradation," in *Polymer Electrolyte Fuel Cell Degradation*, M. Mench, E. Kumbur and T. Veziroglu, Eds., Boston, Academic Press, 2012, pp. 15-88.
- [3] Y. Wang, K. S. Chen, J. Mishler, S. C. Cho and X. C. Adroher, "A review of polymer electrolyte membrane fuel cells: Technology, applications, and needs on fundamental research," *Applied Energy*, vol. 88, no. 4, pp. 981-1007, 2011.
- [4] T. Hua, R. Ahluwalia, L. Eudy, G. Singer, B. Jermer, N. Asselin-Miller, S. Wessel, T. Patterson and J. Marcinkoski, "Status of hydrogen fuel cell electric buses worldwide," *J. Power Sources*, vol. 269, pp. 975 - 993, 2014.
- [5] "Hyundai first to offer hydrogen FCEVs to the Canadian public," *Fuel Cells Bulletin*, vol. 12, pp. 2-3, 2014.
- [6] R. Borup, J. Meyers, B. Pivovar, Y. S. Kim, R. Mukundan, N. Garland, D. Myers, M. Wilson, F. Garzon, D. Wood, P. Zelenay, K. More, K. Stroh, T. Zawodzinski, J. Boncella, J. E. McGrath, M. Inaba, K. Miyatake, M. Hori, K. Ota, Z. Ogumi, S. Miyata, A. Nishikata, Z. Siroma, Y. Uchimoto, K. Yasuda, K. , K.-i. Kimijima and N. Iwashita, "Scientific Aspects of Polymer Electrolyte Fuel Cell Durability and Degradation," *Chem. Rev.*, vol. 107, no. 10, pp. 3904-3951, 2007.

CONFIDENTIAL

- [7] J. Wu, X. Z. Yuan, J. J. Martin, H. Wang, J. Zhang, J. Shen, S. Wu and W. Merida, "A review of PEM fuel cell durability: Degradation mechanisms and mitigation strategies," *J. Power Sources*, vol. 184, no. 1, pp. 104-119, 2008.
- [8] A. A. Topalov, S. Cherevko, A. Zeradjanin, a. R., J. C. Meier, I. Katsounaros and K. J. J. Mayrhofer, "Towards a comprehensive understanding of platinum dissolution in acidic media," *Chem. Sci.*, vol. 5, no. 2, pp. 631-638, 2014.
- [9] K. Yasuda, A. Taniguchi, T. Akita, T. Ioroi and Z. Siroma, "Platinum dissolution and deposition in the polymer electrolyte membrane of a PEM fuel cell as studied by potential cycling," *Phys. Chem. Chem. Phys.*, vol. 8, no. 6, pp. 746-752, 2006.
- [10] E.-k. Ahmad and G. P. Bruno, "Chapter 4 - Gas Diffusion Media and their Degradation," in *Polymer Electrolyte Fuel Cell Degradation*, Boston, Academic Press, 2012, pp. 215-247.
- [11] F. A. de Bruijn, V. A. T. Dam and G. J. M. Janssen, "Review: Durability and Degradation Issues of PEM Fuel Cell Components," *Fuel Cells*, vol. 8, no. 1, pp. 3-22, 2008.
- [12] M. -A. Goulet, S. Arbour, M. Lauritzen and E. Kjeang, "Water sorption and expansion of an ionomer membrane constrained by fuel cell electrodes," *J. Power Sources*, vol. 274, pp. 94-100, 2015.
- [13] M. -A. Goulet, R. M. H. Khorasany, C. De Torres, M. Lauritzen, E. Kjeang, G. G. Wang and N. Rajapakse, "Mechanical properties of catalyst coated membranes for fuel cells," *J. Power Sources*, vol. 234, pp. 38-47, 2013.
- [14] R. M. H. Khorasany, M. -A. Goulet, A. Sadeghi Alavijeh, E. Kjeang, G. G. Wang and R. K. N. D. Rajapakse, "On the constitutive relations for catalyst coated membrane applied to in-situ fuel cell modeling," *J. Power Sources*, vol. 252, pp. 176-188, 2014.
- [15] R. M. H. Khorasany, E. Kjeang, G. G. Wang and R. K. N. D. Rajapakse, "Simulation of ionomer membrane fatigue under mechanical and hygrothermal loading conditions," *J. Power Sources*, vol. 279, pp. 55-63, 2015.

CONFIDENTIAL

- [16] R. M. H. Khorasany, A. Sadeghi Alavijeh, E. Kjeang, G. G. Wang and R. K. N. D. Rajapakse, "Mechanical degradation of fuel cell membranes under fatigue fracture tests," *J. Power Sources*, vol. 274, pp. 1208-1216, 2015.
- [17] A. Sadeghi Alavijeh, R. Khorasany, A. Habisch, G. Wang and E. Kjeang, "Creep Properties of Catalyst Coated Membranes for Polymer Electrolyte Fuel Cells," *J Power Sources*, vol. 285, pp. 16-28, 2015.
- [18] C. Lim, L. Ghassemzadeh, F. Van Hove, M. Lauritzen, J. Kolodziej, G. G. Wang, S. Holdcroft and E. Kjeang, "Membrane degradation during combined chemical and mechanical accelerated stress testing of polymer electrolyte fuel cells," *J. Power Sources*, vol. 257, pp. 102-110, 2014.
- [19] N. Macauley, A. Alavijeh Sadeghi, M. Watson, J. Kolodziej, M. Lauritzen, S. Knights, G. G. Wang and E. Kjeang, "Accelerated Membrane Durability Testing of Heavy Duty Fuel Cells," *J. Electrochem. Soc.*, vol. 162, no. 1, pp. F98-F107, 2015.
- [20] A. Sadeghi Alavijeh, M. -A. Goulet, R. M. H. Khorasany, J. Ghataurah, C. Lim, M. Lauritzen, E. Kjeang, G. G. Wang and R. K. N. D. Rajapakse, "Decay in Mechanical Properties of Catalyst Coated Membranes Subjected to Combined Chemical and Mechanical Membrane Degradation," *Fuel Cells*, vol. 15, no. 1, pp. 204-213, 2015.
- [21] E. Endoh, S. Terazono, H. Widjaja and Y. Takimoto, "Degradation Study of MEA for PEMFCs under Low Humidity Conditions," *Electrochem. Solid-State Lett.*, vol. 7, no. 7, pp. A209-A211, 2004.
- [22] J. Healy, C. Hayden, T. Xie, K. Olson, R. Waldo, M. Brundage, H. Gasteiger and J. Abbott, "Aspects of the Chemical Degradation of PFSA Ionomers used in PEM Fuel Cells," *Fuel Cells*, vol. 5, no. 2, pp. 302-308, 2005.
- [23] F. D. Coms, H. Liu and J. E. Owejan, "Mitigation of Perfluorosulfonic Acid Membrane Chemical Degradation Using Cerium and Manganese Ions," *ECS Trans.*, vol. 16, no. 2, pp. 1735-1747, 2008.
- [24] L. Ghassemzadeh, K. -D. Kreuer, J. Maier and K. Muller, "hemical Degradation of Nafion Membranes under Mimic Fuel Cell Conditions as Investigated by

CONFIDENTIAL

Solid-State NMR Spectroscopy," *J. Phys. Chem. C*, vol. 114, no. 34, pp. 14635-14645, 2010.

- [25] L. Ghassemzadeh and S. Holdcroft, "Quantifying the Structural Changes of Perfluorosulfonated Acid Ionomer upon Reaction with Hydroxyl Radicals," *J. Am. Chem. Soc.*, vol. 135, no. 22, pp. 8181-8184, 2013.
- [26] M. Danilczuk, F. D. Coms and S. Schlick, "Visualizing Chemical Reactions and Crossover Processes in a Fuel Cell Inserted in the ESR Resonator: Detection by Spin Trapping of Oxygen Radicals, Nafion-Derived Fragments, and Hydrogen and Deuterium Atoms," *J. Phys. Chem. B*, vol. 113, no. 23, pp. 8031-8042, 2009.
- [27] M. Spulber and S. Schlick, "Fragmentation of Perfluorinated Membranes Used in Fuel Cells: Detecting Very Early Events by Selective Encapsulation of Short-Lived Fragments in β -Cyclodextrin," *J. Phys. Chem. B*, vol. 115, no. 43, pp. 12415-12421, 2011.
- [28] Y. Nosaka, K. Ohtaka, N. Ohguri and A. Y. Nosaka, "Detection of OH Radicals Generated in Polymer Electrolyte Membranes of Fuel Cells," *J. Electrochem. Soc.*, vol. 158, no. 4, pp. B430-B433, 2011.
- [29] L. Gubler, S. M. Dockheer and W. H. Koppenol, "Radical (HO•, H• and HOO•) Formation and Ionomer Degradation in Polymer Electrolyte Fuel Cells," *J. Electrochem. Soc.*, vol. 158, no. 7, pp. B755-B769, 2011.
- [30] M. Inaba, T. Kinumoto, M. Kiriake, R. Umebayashi, A. Tasaka and Z. Ogumi, "Gas crossover and membrane degradation in polymer electrolyte fuel cells," *Electrochim. Acta*, vol. 51, no. 26, pp. 5746-5753, 2006.
- [31] U. A. Paulus, T. J. Schmidt, H. A. Gastegier and R. Behm, "Oxygen reduction on a high-surface area Pt/Vulcan carbon catalyst: a thin-film rotating ring-disk electrode study," *J. Electroanal. Chem.*, vol. 495, no. 2, pp. 134-145, 2001.
- [32] M. Inaba, H. Yamada, J. Tokunaga and A. Tasaka, "Effect of Agglomeration of Pt/C Catalyst on Hydrogen Peroxide Formation," *Electrochem. Solid-State Lett.*, vol. 7, no. 12, pp. A474-A476, 2004.

CONFIDENTIAL

- [33] A. B. LaConti, M. Hamdan and R. C. McDonald, "Mechanisms of membrane degradation," in *Handbook of Fuel Cells*, John Wiley & Sons, Ltd, 2003.
- [34] A. B. LaConti, H. Liu, C. Mittelsteadt and R. McDonald, "Polymer Electrolyte Membrane Degradation Mechanisms in Fuel Cells - Findings Over the Past 30 Years and Comparison with Electrolyzers," *ECS Trans.*, vol. 1, no. 8, pp. 199-219, 2006.
- [35] M. Aoki, H. Uchida and M. Watanabe, "Decomposition mechanism of perfluorosulfonic acid electrolyte in polymer electrolyte fuel cells," *Electrochem. Commun.*, vol. 8, no. 9, pp. 1509-1513, 2006.
- [36] C. Chen, G. Levitin, D. W. Hess and T. F. Fuller, "XPS investigation of Nafion® membrane degradation," *J. of Power Sources*, vol. 169, no. 2, pp. 288 - 295, 2007.
- [37] T. Madden, D. Weiss, N. Cipollini, D. Condit, M. Gummalla, S. Burlatsky and V. Atrazhev, "Degradation of Polymer-Electrolyte Membranes in Fuel Cells: I. Experimental," *J. Electrochem. Soc.*, vol. 156, no. 5, pp. B657-B662, 2009.
- [38] M. Gummalla, V. V. Atrazhev, D. Condit, N. Cipollini, T. Madden, N. Y. Kuzminyh, D. Weiss and S. F. Burlatsky, "Degradation of Polymer-Electrolyte Membranes in Fuel Cells: II. Theoretical model," *J. Electrochem. Soc.*, vol. 157, no. 11, pp. B1542-B1548, 2010.
- [39] Y. Nosaka, K. Ohtaka, M. Kitazawa, S.-y. Kishioka and A. Nosaka, "Spin-Trapping ESR Detection of OH Radicals Generated in the Electrode Reactions for PEFCs," *Electrochemical and Solid-State Letters*, vol. 12, no. 2, pp. B14-B17, 2009.
- [40] N. Macauley, L. Ghassemzadeh, C. Lim, M. Watson, J. Kolodziej, M. Lauritzen, S. Holdcroft and E. Kjeang, "Pt Band Formation Enhances the Stability of Fuel Cell Membranes," *ECS Electrochem. Lett.*, vol. 2, no. 4, pp. F33-F35, 2013.
- [41] M. J. Eslamibidgoli, P. -E. A. Melchy and M. H. Eikerling, "Modeling the local potential at Pt nanoparticles in polymer electrolyte membranes," *Phys. Chem. Chem. Phys.*, vol. 17, no. 15, pp. 9802-9811, 2015.

CONFIDENTIAL

- [42] D. E. Curtin, R. D. Lousenberg, T. J. Henry, P. C. Tangeman and M. E. Tisack, "Advanced materials for improved PEMFC performance and life," *J. Power Sources*, vol. 131, no. 1, pp. 41-48, 2004.
- [43] T. Xie and C. A. Hayden, "A kinetic model for the chemical degradation of perfluorinated sulfonic acid ionomers: Weak end groups versus side chain cleavage," *Polymer*, vol. 48, no. 19, pp. 5497-5506, 2007.
- [44] A. A. Shah, T. R. Ralph and F. C. Walsh, "Modeling and Simulation of the Degradation of Perfluorinated Ion-Exchange Membranes in PEM Fuel Cells," *J. Electrochem. Soc.*, vol. 156, no. 4, pp. B465-B484, 2009.
- [45] T. Ishimoto, R. Nagumo, T. Ogura, T. Ishihara, B. Kim, A. Miyamoto and M. Koyama, "Chemical Degradation Mechanism of Model Compound, $\text{CF}_3(\text{CF}_2)_3\text{O}(\text{CF}_2)_2\text{OCF}_2\text{SO}_3\text{H}$, of PFSA Polymer by Attack of Hydroxyl Radical in PEMFCs," *J. Electrochem. Soc.*, vol. 157, no. 9, pp. B1305-B1309, 2010.
- [46] T. H. Yu, Y. Sha, W. -G. Liu, B. V. Merinov, P. Shirvanian and W. A. Goddard, "Mechanism for Degradation of Nafion in PEM Fuel Cells from Quantum Mechanics Calculations," *J. Am. Chem. Soc.*, vol. 133, no. 49, pp. 19857-19863, 2011.
- [47] A. M. Dreizler and E. Roduner, "Reaction Kinetics of Hydroxyl Radicals with Model Compounds of Fuel Cell Polymer Membranes," *Fuel Cells*, vol. 12, no. 1, pp. 132-140, 2012.
- [48] M. Kumar and S. J. Paddison, "Side-chain degradation of perfluorosulfonic acid membranes: An ab initio study," *J. Mater. Res.*, vol. 27, no. 15, pp. 1982-1991, 2012.
- [49] L. Ghassemzadeh, T. J. Peckham, T. Weissbach, X. Luo and S. Holdcroft, "Selective Formation of Hydrogen and Hydroxyl Radicals by Electron Beam Irradiation and Their Reactivity with Perfluorosulfonated Acid Ionomer," *J. Am. Chem. Soc.*, vol. 135, no. 42, pp. 15923-15932, 2013.
- [50] C. Zhou, M. A. Guerra, Z. -M. Qiu, T. A. Zawodzinski and D. A. Schiraldi, "Chemical Durability Studies of Perfluorinated Sulfonic Acid Polymers and Model

CONFIDENTIAL

Compounds under Mimic Fuel Cell Conditions," *Macromolecules*, vol. 40, no. 24, pp. 8695-8707, 2007.

- [51] M. Ghelichi, P. -É. A. Melchy and M. H. Eikerling, "Radically Coarse-Grained Approach to the Modeling of Chemical Degradation in Fuel Cell Ionomers," *J. Phys. Chem. B*, vol. 118, no. 38, pp. 11375-11386, 2014.
- [52] E. Endoh, "Development of Highly Durable PFSA Membrane and MEA for PEMFC Under High Temperature and Low Humidity Conditions," *ECS Trans.*, vol. 16, no. 2, pp. 1229-1240, 2008.
- [53] P. Trogadas, J. Parrondo and V. Ramani, "Degradation Mitigation in Polymer Electrolyte Membranes Using Cerium Oxide as a Regenerative Free-Radical Scavenger," *Electrochem. Solid-State Lett.*, vol. 11, no. 7, pp. B113-B116, 2008.
- [54] Z. Wang, H. Tang, H. Zhang, M. Lei, R. Chen, P. Xiao and M. Pan, "Synthesis of Nafion/CeO₂ hybrid for chemically durable proton exchange membrane of fuel cell," *J. Membrane Sci.*, Vols. 421-422, pp. 201-210, 2012.
- [55] B. P. Pearman, N. Mohajeri, R. P. Brooker, M. P. Rodgers, D. K. Slattery, M. D. Hampton, D. A. Cullen and S. Seal, "The degradation mitigation effect of cerium oxide in polymer electrolyte membranes in extended fuel cell durability tests," *J. Power Sources*, vol. 225, pp. 75-83, 2013.
- [56] L. Wang, S. G. Advani and A. K. Prasad, "Degradation reduction of polymer electrolyte membranes using CeO₂ as a free-radical scavenger in catalyst layer," *Electrochim. Acta*, vol. 109, pp. 775-780, 2013.
- [57] C. Lim, A. Sadeghi Alavijeh, M. Lauritzen, J. Kolodziej, S. Knights and E. Kjeang, "Fuel Cell Durability Enhancement with Cerium Oxide under Combined Chemical and Mechanical Membrane Degradation," *ECS Electrochem. Lett.*, vol. 4, no. 4, pp. F29-F31, 2015.
- [58] B. P. Pearman, N. Mohajeri, D. K. Slattery, M. D. Hampton, S. Seal and D. A. Cullen, "The chemical behavior and degradation mitigation effect of cerium oxide nanoparticles in perfluorosulfonic acid polymer electrolyte membranes," *Polym. Degrad. Stabil.*, vol. 98, no. 9, pp. 1766 - 1772, 2013.

CONFIDENTIAL

- [59] S. A. Hayes, P. Yu, T. J. O'Keefe, M. J. O'Keefe and J. O. Stoffer, "The Phase Stability of Cerium Species in Aqueous Systems: I. E-pH Diagram for the Ce-HClO₄-H₂O System," *J. Electrochem. Soc.*, vol. 149, no. 12, pp. C623-C630, 2002.
- [60] S. M. Stewart, D. Spornjak, R. Borup, A. Datye and F. Garzon, "Cerium Migration through Hydrogen Fuel Cells during Accelerated Stress Testing," *ECS Electrochem. Lett.*, vol. 3, no. 4, pp. F19-F22, 2014.
- [61] D. Banham, S. Ye, T. Cheng, S. Knights, S. M. Stewart, M. Wilson and F. Garzon, "Effect of CeO_x Crystallite Size on the Chemical Stability of CeO_x Nanoparticles," *J. Electrochem. Soc.*, vol. 161, no. 10, pp. F1075-F1080, 2014.
- [62] T. T. H. Cheng, S. Wessel and S. Knights, "Interactive Effects of Membrane Additives on PEMFC Catalyst Layer Degradation," *J. Electrochem. Soc.*, vol. 160, no. 1, pp. F27-F33, 2013.
- [63] T. Okada, Y. Ayato, M. Yuasa and I. Sekine, "The Effect of Impurity Cations on the Transport Characteristics of Perfluorosulfonated Ionomer Membranes," *J. Phys. Chem. B*, vol. 103, no. 17, pp. 3315-3322, 1999.
- [64] T. Okada, H. Satou and M. Yuasa, "Effects of Additives on Oxygen Reduction Kinetics at the Interface between Platinum and Perfluorinated Ionomer," *Langmuir*, vol. 19, no. 6, pp. 2325-2332, 2003.
- [65] B. Kienitz, B. Pivovar, T. Zawodzinski and F. H. Garzon, "Cationic Contamination Effects on Polymer Electrolyte Membrane Fuel Cell Performance," *J. Electrochem. Soc.*, vol. 158, no. 9, pp. B1175-B1183, 2011.
- [66] X. Huang, R. Solasi, Y. Zou, M. Feshler, K. Reifsnider, D. Condit, S. Burlatsky and T. Madden, "Mechanical endurance of polymer electrolyte membrane and PEM fuel cell durability," *J. Polym. Sci. B Polym. Phys.*, vol. 44, no. 16, pp. 2346-2357, 2006.
- [67] P.-E. A. Melchy and E. M. H., "Physical theory of ionomer aggregation in water," *Phys. Rev. E*, vol. 89, p. 032603, 2014.

CONFIDENTIAL

- [68] A. A. Shah, K. H. Luo, T. R. Ralph and F. C. Walsh, "Recent trends and developments in polymer electrolyte membrane fuel cell modelling," *Electrochim. Acta*, vol. 56, no. 11, pp. 3731 - 3757, 2011.
- [69] L. Gubler and W. H. Koppenol, "Kinetic Simulation of the Chemical Stabilization Mechanism in Fuel Cell Membranes Using Cerium and Manganese Redox Couples," *J. Electrochem. Soc.*, vol. 159, no. 2, pp. B211-B218, 2011.
- [70] S. Xiao, H. Zhang, C. Bi, Y. Zhang, Y. Zhang, H. Dai, Z. Mai and X. Li, "Degradation location study of proton exchange membrane at open circuit operation," *J. Power Sources*, vol. 195, no. 16, pp. 5305 - 5311, 2010.
- [71] R. Coulon, W. Bessler and A. A. Franco, "Modeling Chemical Degradation of a Polymer Electrolyte Membrane and its Impact on Fuel Cell Performance," *ECS Trans.*, vol. 25, no. 35, pp. 259-273, 2010.
- [72] B. L. Kienitz, H. Baskaran and T. A. Zawodzinski Jr, "Modeling the steady-state effects of cationic contamination on polymer electrolyte membranes," *Electrochim. Acta*, vol. 54, no. 6, pp. 1671-1679, 2009.
- [73] A. Z. Weber and C. Delacourt, "Mathematical Modelling of Cation Contamination in a Proton-exchange Membrane," *Fuel Cells*, vol. 8, no. 6, pp. 459-465, 2008.
- [74] T. A. Greszler, T. E. Moylan and H. A. Gasteiger, "Modeling the impact of cation contamination in a polymer electrolyte membrane fuel cell," in *Handbook of Fuel Cells*, John Wiley and Sons, Ltd, 2010.
- [75] M. F. Serincan, U. Pasaogullari and T. Molter, "Modeling the cation transport in an operating polymer electrolyte fuel cell (PEFC)," *Int. J. Hydrogen Energy*, vol. 35, no. 11, pp. 5539 - 5551, 2010.
- [76] M. B. Satterfield and J. B. Benziger, "Non-Fickian Water Vapor Sorption Dynamics by Nafion Membranes," *J Phys Chem B*, vol. 112, no. 12, pp. 3693-3704, 2008.
- [77] K. H. Wong and E. Kjeang, "Macroscopic In-Situ Modeling of Chemical Membrane Degradation in Polymer Electrolyte Fuel Cells," *J. Electrochem. Soc.*, vol.

CONFIDENTIAL

161, no. 9, pp. F823-F832, 2014.

- [78] C. Siegel, "Review of computational heat and mass transfer modeling in polymer-electrolyte-membrane (PEM) fuel cells," *Energy*, vol. 33, no. 9, pp. 1331 - 1352, 2008.
- [79] M. Safiollah, P. -E. A. Melchy, P. Berg and M. Eikerling, "Model of Water Sorption and Swelling in Polymer Electrolyte Membranes: Diagnostic Applications," *Submitted*, 2015.
- [80] J. Fimrite, B. Carnes, H. Struchtrup and N. Djilali, "Transport Phenomena in Polymer Electrolyte Membranes," *J Electrochem Soc*, vol. 152, no. 9, pp. A1815-A1823, 2005.
- [81] K. H. Wong and E. Kjeang, "Mitigation of Chemical Membrane Degradation in Fuel Cells: Understanding the Effect of Cell Voltage and Iron Ion Redox Cycle," *ChemSusChem*, vol. 8, no. 6, pp. 1072-1082, 2015.
- [82] N. Garland, T. Benjamin and J. Kopasz, "DOE Fuel Cell Program: Durability Technical Targets and Testing Protocols," *ECS Trans.*, vol. 11, no. 1, pp. 923-931, 2007.
- [83] W. Liu and M. Crum, "Effective Testing Matrix for Studying Membrane Durability in PEM Fuel Cells: Part I. Chemical Durability," *ECS Trans.*, vol. 3, no. 1, pp. 531-540, 2006.
- [84] N. Ohguri, A. Nosaka and Y. Nosaka, "Detection of OH Radicals Formed at PEFC Electrodes by Means of a Fluorescence Probe," *Electrochem. Solid-State Lett.*, vol. 12, no. 6, pp. B94-B96, 2009.
- [85] V. A. Sethuraman, J. W. Weidner, A. T. Haug, S. Motupally and L. V. Protsailo, "Hydrogen Peroxide Formation Rates in a PEMFC Anode and Cathode," *J. Electrochem. Soc.*, vol. 155, no. 1, pp. B50-B57, 2008.
- [86] H. Liu, J. Zhang, F. Coms, W. Gu, B. Litteer and H. A. Gasteiger, "Impact of Gas Partial Pressure on PEMFC Chemical Degradation," *ECS Trans.*, vol. 3, no. 1, pp. 493-505, 2006.

CONFIDENTIAL

- [87] M. El Hannach and E. Kjeang, "Stochastic Microstructural Modeling of PEFC Gas Diffusion Media," *J. Electrochem. Soc.*, vol. 161, no. 9, pp. F951-F960, 2014.
- [88] M. El Hannach, R. Singh, N. Djilali and E. Kjeang, "Micro-porous layer stochastic reconstruction and transport parameter determination," *J. Power Sources*, vol. 282, pp. 58 - 64, 2015.
- [89] A. Nanjundappa, A. Sadeghi Alavijeh, M. El Hannach, D. Harvey and E. Kjeang, "A customized framework for 3-D morphological characterization of microporous layers," *Electrochim. Acta*, vol. 110, pp. 349 - 357, 2013.
- [90] R. Singh, A. R. Akhgar, P. C. Sui, K. J. Lange and N. Djilali, "Dual-Beam FIB/SEM Characterization, Statistical Reconstruction, and Pore Scale Modeling of a PEMFC Catalyst Layer," *J. Electrochem. Soc.*, vol. 161, no. 4, pp. F415-F424, 2014.

Appendix A: Macroscopic In-Situ Modeling of Chemical Membrane Degradation in Polymer Electrolyte Fuel Cells

(Reprinted with permission from J. Electrochem. Soc., 161, F823 (2014). Copyright 2014, The Electrochemical Society)



Macroscopic In-Situ Modeling of Chemical Membrane Degradation in Polymer Electrolyte Fuel Cells

Ka Hung Wong* and Erik Kjeang**^z

School of Mechatronic Systems Engineering, Simon Fraser University, Surrey, BC V3T0A3, Canada

Chemical membrane degradation is a major limiting factor for polymer electrolyte fuel cell (PEFC) durability and lifetime. While the main degradation mechanisms are established in the literature, the in-situ trends of their action are often only known qualitatively. This motivates the development of a comprehensive in-situ chemical membrane degradation model addressed in this work. The numerical algorithms developed are strategically designed to be compatible with state-of-the-art computational membrane electrolyte assembly (MEA) performance models; here, we emphasize the integration of the developed degradation model into a 1-D MEA transport-reaction model to determine the linkages between the MEA macroscopic phenomena, in-situ operating conditions, and the temporal membrane degradation process. Concentrations of hydrogen peroxide, radical, and degraded ionomer species are modeled to interrogate the evolution of ionomer molecular structure with respect to the chemical membrane degradation. The proposed degradation mechanism includes the initiation and propagation of side chain degradation culminating in main chain scission and fragmentation, and demonstrates a good agreement with the most recent experimental findings. The integrated MEA model is further applied to simulate the macroscopic effects of chemical membrane degradation characterized in a recent accelerated stress test. Comparisons between the numerical and experimental results are discussed.

© 2014 The Electrochemical Society. [DOI: 10.1149/2.0031409jes] All rights reserved.

Manuscript submitted March 5, 2014; revised manuscript received May 9, 2014. Published May 21, 2014.

Perfluorosulfonic acid (PFSA) ionomer membranes are the industry standard electrolyte material in low temperature polymer electrolyte fuel cells (PEFCs). The high fuel cell performance achieved with these materials is attributed to their thin-film structure with high proton conductivity at low temperatures, superior electrical insulation, and relatively low reactant permeation. However, despite of its chemically stable perfluorinated main chain, the ionomer membrane can undergo various forms of degradation in the fuel cell environment,^{1,2} which is one of the main technical challenges to achieve the durability standards required for PEFCs commercialization.³ Highly durable membranes and advanced technologies targeted at membrane lifetime and reliability improvements are therefore essential.

The durability of PFSA ionomer membranes is primarily constrained by chemical and mechanical degradation processes.^{1,2} When confined in the membrane electrode assembly (MEA), mechanical stress is generated by the changes in membrane water sorption induced by hygrothermal fluctuations.^{4,5} Although pure mechanical failures are possible for membranes subjected to repeated hygrothermal cycles,^{1,2} the chemical degradation is a primary factor that dramatically weakens membrane physicochemical properties, which has been observed in accelerated stress tests (ASTs).⁶⁻⁸

Reactions of highly reactive radicals with the PFSA ionomer molecular structure is generally considered to be the initial progress of chemical membrane degradation in PEFCs.⁹⁻¹³ This hypothesis is corroborated by the in-situ detection of hydroxyl (OH·), hydroperoxyl (OOH·), and hydrogen (H·) radicals and degraded ionomer species comprising oxygen and carbon centered radicals by utilizing an electron spin resonance (ESR) spectrometer^{14,15} or a fluorescence probe.¹⁶ The hydroxyl radical is the "usual suspect" responsible for the chemical degradation^{10,12} and can initiate the formation of hydroperoxyl and hydrogen radicals.¹² Hydroxyl radicals can be generated from decomposition of hydrogen peroxide via transition metal cations, e.g., Fe²⁺,¹⁷ and from the reaction of hydrogen and oxygen on the surface of platinum.¹¹ Radical attack on the carboxylic acid end group on the main chain has been discussed and modeled.^{12,18,19} However, more recent studies focused on side chain degradation^{13,20-24} that has become more important in developing mitigation strategies for chemical membrane degradation since the carboxylic acid group concentration of recent industry standard membranes is significantly reduced.²⁵

Two possible initiations of side chain degradation, C-S bond and ether bond cleavages, were suggested in the literature. C-S bond cleavage was proposed in the literature^{11,21,23} and supported by density

functional theory (DFT) calculations.^{21,23} However, ether bond cleavage was shown to be more favorable in other DFT calculations²⁰ and supported by several experiments.^{13,24} Moreover, side chain unzipping initialized from ether bond cleavage was recently reported based on nuclear magnetic resonance (NMR) results of membranes subjected to the ex-situ Fenton's test.¹³

The PEFC modeling capabilities developed over the past several decades have become a powerful tool for analysis of the interrelated and complex phenomena occurring during operation.^{26,27} However, only a few models developed to date^{18,19,27-30} have considered the chemical membrane degradation, despite its critical role in the design cycle of durable membrane and fuel cell technologies. Xie et al. developed a chemical kinetic model to study the characteristics of the side chain cleavage and the main chain carboxylic acid unzipping reactions in order to quantitatively distinguish them.¹⁸ A transient degradation model was developed by Shah et al. to study the evolution of hydrogen peroxide, hydroxyl radical, and carboxylic acid group concentrations under various operating conditions and types of degradation mechanisms (i.e., with or without side chain degradation).¹⁹ Gummalla et al. focused on the hydroxyl radical decomposition and generation on platinum as a function of platinum size and spacing in order to study the role of platinum in the membrane during chemical membrane degradation.²⁸ Kunda et al. developed an empirical model to relate the cumulative fluoride release and the open circuit voltage (OCV) drop with the chemical membrane degradation.²⁹ Coulon et al. established a feedback between the proton conductivity and the sulfonic acid group concentration in the chemically degraded membrane.³⁰ However, despite the importance and complexity of the chemical membrane degradation,^{1,2} simplified mechanisms based on a single chemical reaction between the ionomer (the side chain group) and the hydroxyl radical were generally considered in previous models. In contrast, recent experimental reports^{8,13} suggest that the membrane degradation process involves the initiation and unzipping along the side chain. Therefore, a more comprehensive mechanism of the chemical membrane degradation ought to be included.

The objective of the present work is to develop a 1-D macroscopic MEA model with a comprehensive membrane degradation algorithm for simulation of the in-situ macroscopic effects of chemical membrane degradation. The degradation algorithm is based on the experiential findings in Refs. 8 and 13 that are generally neglected or simplified in previous PEFC degradation models. In this context, complete predictions of the evolution of ionomer molecular structure and macroscopic properties, hydrogen peroxide, and hydroxyl radicals with respect to the degradation initiation and propagation are achieved. The simulated ionomer molecular structure is compared and validated with recent experimental results.⁸ Moreover, the numerical

*Electrochemical Society Student Member.

**Electrochemical Society Active Member.

^zE-mail: ekjeang@sfu.ca

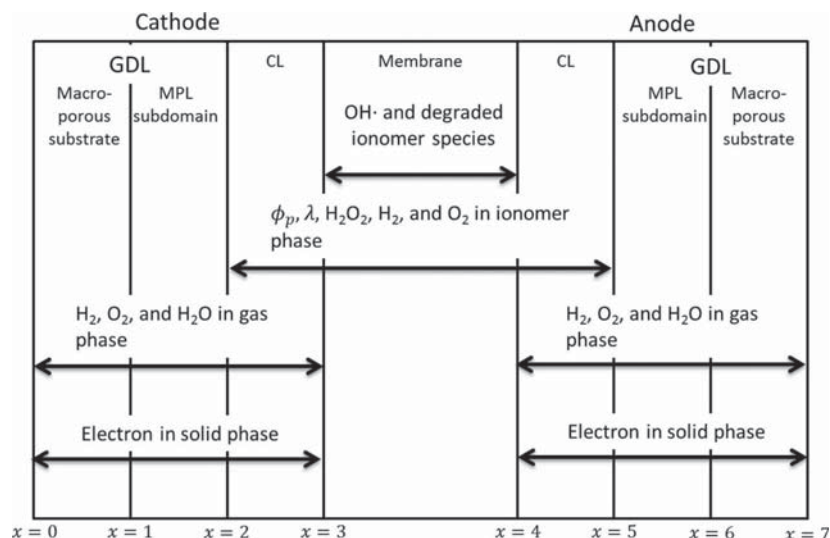


Figure 1. Schematic of the computational domain, including membrane, catalyst layers (CLs), and gas diffusion layers (GDLs; consisting of a macroporous substrate and a microporous layer). The x -axis represents the through-plane direction and starts at the cathode gas channel (GC) and GDL interface. Gas and electron transport is considered in GDLs and CLs, and transport in the ionomer phase is considered in the CLs and membrane. Chemical degradation is considered in the membrane.

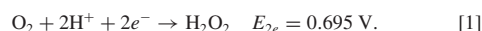
algorithms developed in the model are designed to be compatible with state-of-the-art computational MEA and fuel cell performance models in order to provide a linkage among macroscopic phenomena, in-situ operating conditions, and the membrane degradation. The model is further applied in a 1-D MEA domain to simulate the macroscopic effects of chemical membrane degradation on membrane thinning, fluoride release rates, ionic resistance, and open circuit voltage during accelerated stress test (AST) of PEFCs.⁸ A comparison of numerical and experimental results is provided, and the overall capabilities of the model are discussed.

Model Formulation and Governing Equations

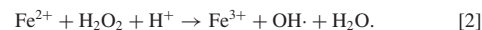
The present modeling framework is based on in-situ chemical degradation of non-reinforced PFSA ionomer membranes. The degradation model involves the radical formation, the mechanisms of membrane degradation, and their effects on the membrane physicochemical properties. The ionomer degradation in the catalyst layers is not considered in the present model because no evidence was found for ionomer degradation in the catalyst layers in our accelerated stress tests.^{7,8} In order to simulate degradation in a realistic fuel cell environment, the degradation model is integrated into a 1-D MEA performance model. The MEA model describes the macroscopic transport phenomena governed by the conservation equations of mass and species which are generally described by a diffusion-reaction system.²⁶ The system of equations is solved in a computational domain comprising of membrane, catalyst layers (CLs), and gas diffusion layers (GDLs) with separate macroporous substrate and microporous layer (MPL) subdomains, as illustrated schematically in Figure 1. The x -axis represents the through-plane direction and starts at the cathode gas channel (GC) and GDL interface. The MEA dimensions and physical parameters used in the model are listed in Table I. All MEA layers are normalized by thickness. Three distinct phases are considered in the model: the gas phase and solid phase in GDLs and CLs, and the ionomer phase in CLs and membrane. The schematic also indicates the various species and transport phenomena considered in the model.

Radical formation.— In PEFCs, hydrogen peroxide (H_2O_2) can be formed electrochemically via the two-electron oxygen reduction

reaction (ORR) in the CLs:³¹



The H_2O_2 formed at the electrodes may diffuse into the membrane and decompose into $\text{OH}\cdot$ via the Fenton's reaction mechanism in the presence of ferrous iron, Fe^{2+} :¹⁷



The common presence of ferrous iron traces in fuel cell membranes is usually a result of contamination during fabrication and/or operation. The mechanism of the contamination and the role of other, secondary types of radicals (e.g., hydroperoxyl and hydrogen radicals) are beyond the scope of the present article.

Mechanisms of membrane degradation.— The PFSA ionomer consists of a polytetrafluoroethylene (PTFE) backbone decorated with sulfonic acid side chains, as depicted in Figure 2, using Nafion as an example. The basic ionomer properties are listed in Table II. A pure PTFE backbone is assumed in the model, provided that main chain

Table I. Structural and physical parameters used in the model.

Parameter	Symbol	Value (Unit)
Thickness of:		
GDL macroporous substrate	L_{GDL}	250 (μm)
MPL subdomain	L_{MPL}	25 (μm)
CL	L_{CL}	10 (μm)
BOL Membrane	$L_{\text{M,0}}$	30 (μm)
Porosity of:		
GDL macroporous substrate	ϵ_{GDL}	0.78 ⁴²
MPL subdomain	ϵ_{MPL}	0.65 ⁴²
CL	ϵ_{CL}	0.4 ⁴³
Ionomer fraction in membrane	ϵ_{M}	0.3 ⁴⁴
Faraday's constant	F	96485 (C mol^{-1})
Gas constant	R	8.314 ($\text{J K}^{-1} \text{mol}^{-1}$)
Molar volume of water	V_w	1.8×10^{-5} ($\text{m}^3 \text{mol}^{-1}$) ⁴⁵
Molar mass of Fe	M_{Fe}	0.056 (kg)
Water concentration	c_w	5.56×10^4 (mol m^{-3})

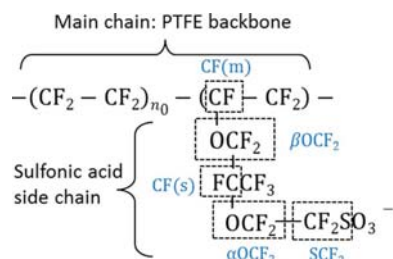
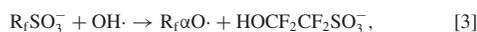


Figure 2. The molecular structure of Nafion ($n_0 = 6.5$ for an equivalent weight (EW) around 1.1 kg mol^{-1}).

defects have been effectively eliminated by ionomer manufacturers.²⁵ Therefore, the membrane degradation is assumed to be dominated and initiated by side chain degradation. The side chain degradation mechanism applied in the model is consistent with recent experimental results,^{8,13} and the details are summarized in Figures 3 and 4. First, the $\text{OH}\cdot$ radical attacks the side chain ether bond in the αOCF_2 group to form an oxygen centered radical that is labeled as $\text{R}_f\alpha\text{O}\cdot$ in Figure 3:



where it is assumed four hydrogen fluoride are released from the degradation of $\text{HOFC}_2\text{CF}_2\text{SO}_3^-$. Further side chain unzipping degradation on the $\text{R}_f\alpha\text{O}\cdot$ triggered by three hydroxyl radicals¹¹ forms another oxygen centered radical labeled as $\text{R}_f\beta\text{O}\cdot$ in Figure 3:

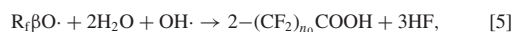


Main chain scission is also feasible in stabilized PFSA ionomer membranes, as evidenced by characterization of degraded material samples subjected to hydrogen peroxide vapor test.³² One appropriate

Table II. Ionomer parameters used in the model.

Parameters	Symbol	Value (Unit)
Nafion properties:		
Dry membrane density	ρ_M	$1980 \text{ (kg m}^{-3}\text{)}^{39}$
BOL equivalent weight	EW_0	$1.093 \text{ (kg mol}^{-1}\text{)}$
BOL average number of CF_2 per SO_3	$2n_0$	13
BOL molar volume of ionomer	$V_{M,0}$	$\text{EW}_0/\rho_M \text{ (m}^3 \text{mol}^{-1}\text{)}$
Average molecular weight of:		
R_fSO_3	$M_{\text{R}_f\text{SO}_3}$	$1.093 \text{ (kg mol}^{-1}\text{)}$
$\text{R}_f\alpha\text{O}\cdot$	$M_{\text{R}_f\alpha\text{O}\cdot}$	$0.913 \text{ (kg mol}^{-1}\text{)}$
$\text{R}_f\beta\text{O}\cdot$	$M_{\text{R}_f\beta\text{O}\cdot}$	$0.747 \text{ (kg mol}^{-1}\text{)}$
CF_2 group	M_{CF_2}	$0.05 \text{ (kg mol}^{-1}\text{)}$
$(\text{CF}_2)_j\text{COOH}$	$M_{(\text{CF}_2)_j\text{COOH}}$	$nM_{\text{CF}_2} + 0.045 \text{ (kg mol}^{-1}\text{)}$
Main chain fragment	M_{MC}	$0.75 \text{ (kg mol}^{-1}\text{)}$

mechanism for main chain scission is the proceeding degradation of the backbone induced by the side chain degradation,^{11,18} as described by:



in which the backbone is cleaved and two carboxylic acid end groups, $-\text{COOH}$, are formed. Although the side chain positioning along the main chain is determined by the copolymerization process, it is reasonable to assume that the side chains are uniformly distributed such that each carboxylic acid group is flanked by n_0 CF_2 groups after the main chain scission event, where $2n_0$ represents the average number of main chain CF_2 groups per side chain in the pristine ionomer. The carboxylic acid groups created by this mechanism can be further attacked by hydroxyl radicals, as described by the well-established main chain unzipping reaction:^{18,25}

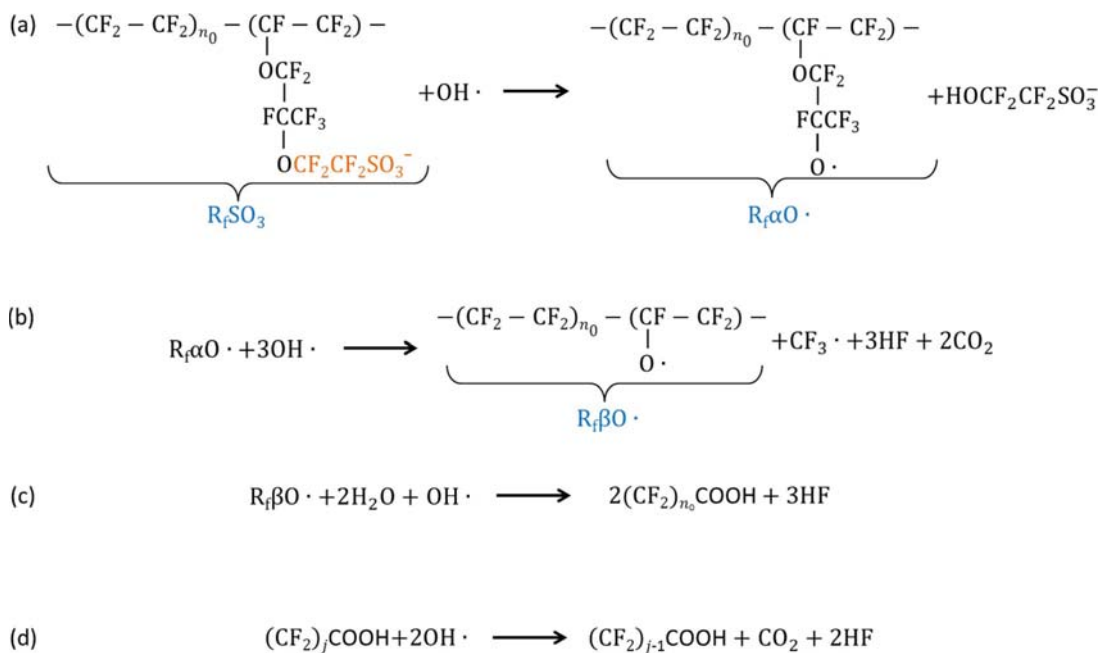
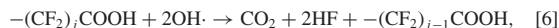


Figure 3. Schematic of the side chain degradation mechanism due to hydroxyl radical attack. Side chain cleavage is initiated by hydroxyl radical attack at the second ether group in the side chain (a), followed by stepwise propagation along the side chain (b). Main chain scission occurs by hydroxyl radical attack of the $\beta\text{O}\cdot$ intermediate ionomer species (c). The carboxylic acid groups formed after the main chain scission degrades via the unzipping reaction (d).

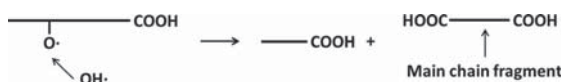


Figure 4. Symbolical illustration of the main chain mass loss due to main chain fragmentation induced by recurrent side chain degradation.

in which the number of carboxylic acid groups is conserved while the number of the CF_2 groups is reduced.

The degradation mechanism considered in Figure 3 mainly induces mass and fluorine losses from the side chain. However, as the degradation progresses, widespread main chain scission events induced by side chain degradation in multiple locations may also result in the loss of small main chain fragments from the membrane. This process, in which the ionomer breaks up into smaller fragments, is illustrated symbolically in Figure 4. Main chain fragmentation triggers additional material loss when the fragments become sufficiently small to be released out of the membrane.

The in-situ evolution of membrane physicochemical properties is calculated in terms of the chemical membrane degradation mechanism illustrated in Figures 3 and 4. The total dry weight of the degraded membrane per unit volume can be expressed to capture the total material removed from the membrane:

$$W_{\text{total}} = \sum_i c_i M_i - c_{\text{MC}} M_{\text{MC}} \quad [7]$$

$$i = \text{R}_f\text{SO}_3, \text{R}_f\alpha\text{O}, \text{R}_f\beta\text{O}, \text{ and } (\text{CF}_2)_n\text{COOH},$$

where c_i and M_i represent the concentration and molecular weight of the ionomer species i .

The average molecular weights of the R_fSO_3 , $\text{R}_f\alpha\text{O}$, and $\text{R}_f\beta\text{O}$ species are constant according to their molecular structures depicted in Figure 3, with corresponding data listed in Table II. The average molecular weight of the $-(\text{CF}_2)_n\text{COOH}$ species, $M_{(\text{CF}_2)_n\text{COOH}}$, depends on the average number of CF_2 groups, described by:

$$n = \frac{c_{\text{CF}_2}}{c_{(\text{CF}_2)_n\text{COOH}}}, \quad [8]$$

where c_{CF_2} is the concentration of CF_2 groups. The material loss due to main chain scission is captured by the last term in Eq (7), where c_{MC} and M_{MC} denote the concentration and average molecular weight of the main chain fragments released from the membrane.

Equivalent weight (EW) is defined as the ratio between the total dry weight of the membrane per unit volume and the concentration of

sulfonic acid groups:

$$\text{EW} = \frac{W_{\text{total}}}{c_{\text{R}_f\text{SO}_3}}. \quad [9]$$

The ion exchange capacity (IEC), which is the reciprocal of EW, is highly correlated with the proton conductivity and water diffusivity because of its significant influence on the volume fraction of the hydrophilic domain in the membrane. The hydrophilic domain formed by the sulfonic acid groups and water enables proton and water transport in the humidified membrane.³³ The volume fraction of the hydrophilic domain is defined as the total volume of sorbed water divided by the total volume of the humidified membrane, which is a function of water content (λ) and IEC as shown by:³³

$$\varepsilon_w = \frac{\lambda V_w}{\lambda V_w + V_M}, \quad [10]$$

where V_w is the molar volume of water and V_M is the molar volume of ionomer that equals $1/\text{IEC}\rho_M$ where ρ_M is the density of dry ionomer. The dissolved water diffusivity and proton conductivity, denoted by $D_{w,M}$ and σ_p , are related to the volume fraction through a power law dependency according to percolation theory:³³⁻³⁵

$$\sigma_p \propto D_{w,M} \propto (\varepsilon_w - \varepsilon_{w,\text{th}})^q \quad [11]$$

in which the water and protons are mobile only if the volume fraction exceeds the threshold volume fraction, $\varepsilon_{w,\text{th}}$.

Governing equations in the gas phase.—The conservation of species equation governing the gas phase transport phenomena is briefly expressed as a reaction-diffusion equation:⁴⁶

$$\nabla \cdot (-D_{i,G}^{\text{eff}} \nabla c_{i,G}) = S_{i,G}, \quad [12]$$

in which subscript G represents the gas phase. Gas diffusion is assumed to be the dominant mechanism as the convection in the through-plane direction is minimal and can be neglected. The correlations between the effective diffusivity, $D_{i,G}^{\text{eff}}$, and the bulk diffusivity, $D_{i,G}$, in the GDLs^{36,37} and CLs are given by:

$$\frac{D_{i,G}^{\text{eff}}}{D_{i,G}} = \begin{cases} 0.407 & \text{in GDL macroporous substrate} \\ 0.18 & \text{in MPL subdomain} \\ \varepsilon_G^{1.5} & \text{in CL,} \end{cases} \quad [13]$$

where ε_G is the porosity. The bulk diffusivity can be approximated by the binary diffusivity, and its calculation is shown in Table III.

Table III. Constitutive relationships and parameters associated with calculation of gas diffusivity.

Description	Symbol	Expression (Unit)
HF diffusivity	D_{HF}	$2.6 \times 10^{-5} (\text{m}^2 \text{s}^{-1})^{46}$
H_2O_2 diffusivity	$D_{\text{H}_2\text{O}_2}$	$1.88 \times 10^{-5} (\text{m}^2 \text{s}^{-1})^{47}$
Binary diffusivity in anode	D_{i,H_2}	$3.2042 \times 10^{-4} \frac{T^{1.75} \sqrt{1/M_i + 1/M_{\text{H}_2}}}{P(v_i^{1/3} + v_{\text{H}_2}^{1/3})^2} (\text{m}^2 \text{s}^{-1})^{48}$
Binary diffusivity in cathode	D_{i,N_2}	$3.2042 \times 10^{-4} \frac{T^{1.75} \sqrt{1/M_i + 1/M_{\text{N}_2}}}{P(v_i^{1/3} + v_{\text{N}_2}^{1/3})^2} (\text{m}^2 \text{s}^{-1})^{48}$
Total pressure	P	$\sum_i c_i RT$
Molar mass of:		
H_2	M_{H_2}	0.002 (kg mol ⁻¹)
O_2	M_{O_2}	0.032 (kg mol ⁻¹)
N_2	M_{N_2}	0.028 (kg mol ⁻¹)
water vapor	M_w	0.018 (kg mol ⁻¹)
Diffusion volume of:		
H_2	v_{H_2}	7.07 ⁴⁸
O_2	v_{O_2}	16.6 ⁴⁸
N_2	v_{N_2}	17.9 ⁴⁸
water vapor	v_w	12.7 ⁴⁸

Table IV. Variables defined and used in the membrane binary friction model (BFM2).^{34, 35}

Description	Variable	Expression (Unit)
Proton conductivity	σ_p	$\frac{(\epsilon_w - \epsilon_{w,th})^{1.5} c_w F^2}{RT \lambda} \frac{D_{1M}(D_{12}\lambda + D_{2M})}{D_{12}\lambda + D_{1M}(\lambda - 1) + D_{2M}}$ (S m ⁻¹)
Water diffusivity	$D_{w,M}$	$\frac{(\epsilon_w - \epsilon_{w,th})^{1.5} c_w}{c_{SO_3}\lambda} \frac{D_{2M}D_{12}}{D_{12}\lambda + D_{1M}(\lambda - 1) + D_{2M}}$ (m ² s ⁻¹)
Electro-osmotic drag coefficient	n_d	$\frac{D_{2M}}{D_{12} + D_{2M}/\lambda}$
Effective diffusion coefficient of species-species	D_{12}	$6.5 \times 10^{-9} \exp\left(\frac{1800}{303} - \frac{1800}{T}\right)$ (m ² s ⁻¹)
species-medium	D_{1M}	$0.084 D_{12} \lambda^{0.77}$ (m ² s ⁻¹)
species-medium	D_{2M}	$0.3 D_{12} \lambda^{0.77}$ (m ² s ⁻¹)
Threshold porosity	$\epsilon_{w,th}$	$\frac{1.65 V_w}{1.65 V_w + V_{M,0}}$

Governing equations in the ionomer phase.— In PEFCs, proton conduction, dissolved water diffusion, and electro-osmotic drag are the dominant mechanisms that govern the proton and water transport phenomena in the ionomer phase of the membrane and CLs:²⁶

$$\nabla \cdot (-\sigma_p^{\text{eff}} \nabla \phi_p) = S_p \text{ and} \quad [14]$$

$$\nabla \cdot (-D_{w,M}^{\text{eff}} c_{R_1SO_3} \nabla \lambda + n_d J_p) = S_{w,M}, \quad [15]$$

in which $J_p = -\sigma_p^{\text{eff}} \nabla \phi_p$ is the proton flux in the membrane. In these equations, the protonic potential, ϕ_p , and the water content, λ , in the ionomer phase are solved. The binary friction membrane model (BFM2) introduced by Fimrite et al.^{34,35} is applied to calculate the proton conductivity, water diffusivity, and electro-osmotic drag coefficient. The variables defined and used in BFM2 are listed in Table IV.

In the CLs, the effective proton conductivity and diffusivity of the ionomer phase species, σ_p^{eff} and $D_{w,M}^{\text{eff}}$, are calculated using the Bruggeman approximation, i.e.:

$$\frac{\sigma_p^{\text{eff}}}{\sigma_p} = \frac{D_{w,M}^{\text{eff}}}{D_{w,M}} = \epsilon_M^{1.5} \quad [16]$$

where ϵ_M is the volume fraction of the ionomer phase.

Diffusion is the dominant transport mechanism for hydrogen, oxygen and hydrogen peroxide species in the ionomer phase. Therefore, the governing equation can be written as:

$$\nabla \cdot (-D_i^{\text{eff}} \nabla c_i) = S_i, \quad [17]$$

where c_i , D_i^{eff} and S_i are the concentration, effective diffusivity, and source of species i . The diffusivities of the all ionomer phase species are tabulated in Table V.

The model is strategically designed to capture the transient evolution of the concentration and distribution of the hydroxyl radical, ionomer species, and hydrogen fluoride associated with the chemical degradation, i.e., distribution of $c_{OH\cdot}$, $c_{R_1SO_3}$, $c_{R_1\alpha O\cdot}$, $c_{R_1\beta O\cdot}$, $c_{(CF_2)_nCOOH}$,

c_{MC} , c_{CF_2} , and c_{HF} , which is essential to adequately simulate the degradation rate and membrane properties at various stages of membrane life. The transient term, $\partial c_i / \partial t$, is thus included in the diffusion-reaction equation:

$$\frac{\partial}{\partial t} c_i + \nabla \cdot (-D_i^{\text{eff}} \nabla c_i) = S_i. \quad [18]$$

The diffusivity of OH \cdot is assumed to be zero because of its short lifetime. Zero diffusivity is also assumed for ionomer species that are bonded to the polymer chain, including $c_{R_1SO_3}$, $c_{R_1\alpha O\cdot}$, $c_{R_1\beta O\cdot}$, $c_{(CF_2)_nCOOH}$, c_{MC} , and c_{CF_2} . Only the hydrogen fluoride, carbon dioxide, and other tiny species formed during the chemical membrane degradation diffuses from the membrane to the CL and ultimately exits the MEA.

Governing equation in the solid carbon phase.— Electron conduction in GDL substrates and CLs can be described by:

$$\nabla \cdot (-\sigma_s^{\text{eff}} \nabla V_s) = S_s, \quad [19]$$

where V_s is the potential of the solid phase (carbon/graphite). The through-plane electronic conductivity of graphite, σ_s , is 1250 S m⁻¹¹⁹ while the value in the porous media is calculated by using the Bruggeman approximation.

Reaction kinetics.— The hydrogen oxidation reaction (HOR) and four-electron ORR are the regular electrochemical reactions occurring in the anode and cathode, respectively, and their reaction rates can be described by the Butler-Volmer kinetics:²⁶

$$r_{\text{HOR}} = a i_{\text{HOR},0} \frac{c_{\text{H}_2,\text{G}}}{c_{\text{H}_2,\text{ref}}} \left[\exp\left(\frac{F \eta_{\text{HOR}}}{2RT}\right) - \exp\left(-\frac{F \eta_{\text{HOR}}}{2RT}\right) \right], \quad [20]$$

$$r_{4e} = a i_{4e,0} \frac{c_{\text{O}_2,\text{G}}}{c_{\text{O}_2,\text{ref}}} \left[\exp\left(\frac{F \eta_{4e}}{RT}\right) - \exp\left(-\frac{F \eta_{4e}}{RT}\right) \right]. \quad [21]$$

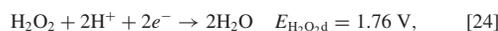
The kinetics of hydrogen peroxide formation via the two-electron ORR, as shown in Eq. 1, can also be calculated using the Butler-Volmer equation,¹⁹ depending on the nature of the CL.³⁸

$$r_{2e} = -a i_{2e,0} \frac{c_{\text{O}_2,\text{G}}}{c_{\text{O}_2,\text{ref}}} \left(\frac{c_{\text{H}^+}}{c_{\text{H}^+,\text{ref}}} \right)^2 \exp\left(-\frac{F \eta_{2e}}{2RT}\right), \quad [22]$$

where the proton concentration, c_{H^+} , is calculated by the density and equivalent weight of the ionomer in the CLs:³⁹

$$c_{\text{H}^+} = \frac{\rho_M}{EW_0} = \frac{1980 + 32.4\lambda}{(1 + 0.0648\lambda) EW_0}. \quad [23]$$

Moreover, hydrogen peroxide reduction can occur at the platinum surface in the CLs via:



with Butler-Volmer kinetics:⁴⁰

$$r_{\text{H}_2\text{O}_2/\text{d}} = 2a i_{\text{H}_2\text{O}_2/\text{d},0} \frac{c_{\text{H}_2\text{O}_2}}{c_{\text{H}_2\text{O}_2,\text{ref}}} \sinh\left(\frac{\alpha_{\text{H}_2\text{O}_2} F \eta_{\text{H}_2\text{O}_2/\text{d}}}{RT}\right). \quad [25]$$

Table V. Diffusivities of species in the ionomer phase.

Symbol	Value (m ² s ⁻¹)
$D_{\text{H}_2,\text{M}}$	$4.1 \times 10^{-7} \exp(-2602/T)^{49}$
$D_{\text{O}_2,\text{M}}$	$3.1 \times 10^{-7} \exp(-2768/T)^{50}$
$D_{\text{H}_2\text{O}_2,\text{M}}$	1.5×10^{-10}
$D_{\text{HF},\text{M}}$	1.5×10^{-10}
$D_{\text{OH},\text{M}}$	0
$D_{\text{R}_1\text{SO}_3,\text{M}}$	0
$D_{\text{R}_1\alpha\text{O},\text{M}}$	0
$D_{\text{R}_1\beta\text{O},\text{M}}$	0
$D_{(\text{CF}_2)_n\text{COOH},\text{M}}$	0
$D_{\text{MC},\text{M}}$	0
$D_{\text{CF}_2,\text{M}}$	0

Table VI. Parameters associated with calculation of reaction kinetics.

Parameter	Symbol	Value (Unit)
Local overpotential	η_i	$V_s - \phi_+ - E_i$ (V)
Active species surface area	a	10^4 (m ²)
Exchange current density of:		
HOR	$i_{\text{HOR},0}$	10^5 (A m ⁻²)
4e ORR	$i_{4e,0}$	1 (A m ⁻²)
2e ORR	$i_{2e,0}$	10^{-2} (A m ⁻²)
H ₂ O ₂ reduction	$i_{\text{H}_2\text{O}_2,\text{d},0}$	10^{-5} (A m ⁻²)
Reference concentration of:		
H ₂	$c_{\text{H}_2,\text{ref}}$	40.88 (mol m ⁻³)
O ₂	$c_{\text{O}_2,\text{ref}}$	40.88 (mol m ⁻³)
H ₂ O ₂	$c_{\text{H}_2\text{O}_2,\text{ref}}$	40.88 (mol m ⁻³)
Transfer coefficient of:		
H ₂ O ₂ reduction	$\alpha_{\text{H}_2\text{O}_2}$	0.32 at anode (0.7 at cathode)
Reaction rate of:		
Eq. 2	k_{fenton}	63×10^{-3} (mol ⁻¹ s ⁻¹) ¹²
Eq. 3	k_1	3.7×10^3 (mol ⁻¹ s ⁻¹) ²²
Eq. 4	k_2	3×10^4 (mol ⁻¹ s ⁻¹)
Eq. 5	k_3	8.5×10^4 (mol ⁻¹ s ⁻¹)
Eq. 6	k_{unzip}	10^3 (mol ⁻¹ s ⁻¹) ¹²
Equilibrium potential for:		
4e ORR	E_{4e}	$1.23 - 0.9 \times 10^{-3}$ (T-298.15) (V)
2e ORR	E_{2e}	0.695 (V)
HOR	E_{HOR}	0 (V)
H ₂ O ₂ reduction	$E_{\text{H}_2\text{O}_2}$	1.76 (V)
Ferrous ion concentration	$c_{\text{Fe}^{2+}}$	$[\text{Fe}] \frac{\text{PM}}{M_{\text{Fe}^{2+}}}$ (mol m ⁻³)
Fe ²⁺ concentration for AST	[Fe]	6 (ppm)

The kinetics of the chemical reactions associated with the radical formation and attack on the membrane are given by:

$$r_{\text{fenton}} = k_{\text{fenton}} c_{\text{H}_2\text{O}_2} c_{\text{Fe}^{2+}}, \quad [26]$$

$$r_1 = k_1 c_{\text{R}_f\text{SO}_3\text{COH}\cdot}, \quad [27]$$

$$r_2 = k_2 c_{\text{R}_f\alpha\text{O}\cdot\text{COH}\cdot}, \quad [28]$$

$$r_3 = k_3 c_{\text{R}_f\beta\text{O}\cdot\text{COH}\cdot}, \quad [29]$$

$$r_{\text{unzip}} = k_{\text{unzip}} c_{(\text{CF}_2)_n\text{COOH}\cdot\text{COH}\cdot}, \quad [30]$$

in which r_{fenton} , r_1 , r_2 , r_3 , and r_{unzip} represent the reaction rates of Eqs. 2–6, respectively. All parameters used in calculating the chemical kinetics are listed in Table VI.

Interfacial mass transport.— The interfacial transport of hydrogen, oxygen, water vapor, hydrogen peroxide and hydrogen fluoride between the ionomer and gas phases is also accounted for by the model. The rate of interfacial mass transport is assumed to be proportional to the difference between the actual ionomer phase concentration, $c_{i,M}$, and the ionomer phase concentration in equilibrium with respect to the gas phase concentration, $c_{i,\text{eq}}$, as described by:

$$r_{i,\text{MG}} = k_{i,\text{MG}} (c_{i,M} - c_{i,\text{eq}}). \quad [31]$$

All variables and parameters used in the modeling of interfacial mass transport are listed in Table VII.

Source terms.— In the model, the source terms, S_i , in the governing equations include the production and consumption due to reactions and interfacial mass transport. All the source terms considered are summarized in Table VIII. The source terms of the ionomer species associated with the chemical membrane degradation are determined according to the detailed mechanisms shown in Figures 3 and 4. It is assumed that all fluorides released during the degradation are in the form of hydrogen fluoride. The carboxylic acid group is conserved provided the backbone CF₂ group concentration is greater than the threshold value, and therefore the Heaviside step function, $H(c_{\text{CF}_2,n\text{COOH}} - c_{\text{CF}_2})$, is required to capture this effect.

Boundary conditions.— The boundary conditions are summarized in Table IX. The inlet hydrogen, oxygen, and water vapor concentrations, i.e., $c_{\text{H}_2,\text{inlet}}$, $c_{\text{O}_2,\text{inlet}}$, and $c_{w,\text{inlet}}$, respectively, are calculated according to the operating conditions presented in Ref. 8. Hydrogen peroxide and hydrogen fluoride concentrations in the gas phase are assumed to be zero at the gas channel and GDL interfaces. Zero flux is assumed at the CL and MPL interfaces ($x = 2$ and 4) for the dissolved species in the ionomer phase. For the remaining ionomer species that participate in the membrane degradation, no boundary conditions but initial conditions are required, provided that these species are fixed inside the membrane. The initial concentrations are:

$$c_{i,0} = \begin{cases} 0 & i = \text{OH}\cdot, \text{R}_f\alpha\text{O}\cdot, \text{R}_f\beta\text{O}\cdot, (\text{CF}_2)_n\text{COOH}, \text{CF}_2, \text{ and MC} \\ \rho_M/\text{EW}_0 & i = \text{R}_f\text{SO}_3 \end{cases} \quad [32]$$

Results and Discussion

The proposed 1-D macroscopic MEA model with its underlying in-situ chemical membrane degradation algorithm is applied to simulate membrane degradation in the case of a recently published cyclic open circuit voltage (COCV) accelerated stress test (AST).⁸ The COCV AST combines chemical and mechanical membrane degradation by means of a steady state OCV-hold phase to accelerate chemical degradation and periodic wet/dry cycles to apply mechanical stress. A full range of diagnostic methods were applied to provide consistent and

Table VII. Variables and parameters associated with calculation of interfacial mass transport.

Parameter	Symbol	Expression (Unit)
Mass transfer coefficient	$k_{i,\text{MG}}$	$\begin{cases} 1.3(\text{s}^{-1}) & i = \text{w} \\ 1000(\text{s}^{-1}) & \text{otherwise} \end{cases}$
Equilibrium concentration	$c_{i,\text{eq}}$	$\begin{cases} c_{i,\text{G}}RT/H_i$ (mol m ⁻³) & for H ₂ and O ₂ , \\ $c_{\text{R}_f\text{SO}_3}\lambda_{\text{eq}}$ (mol m ⁻³) & for vapor \end{cases}
Henry's constant of H ₂	H_{H_2}	$0.2584 \times 10^4 \exp(\frac{170}{T})$ (Pa m ³ mol ⁻¹) ⁵¹
Henry's constant of O ₂	H_{O_2}	$1.348 \times 10^5 \exp(\frac{-666}{T})$ (Pa m ³ mol ⁻¹) ⁵²
Henry's constant of HF	H_{HF}	$4.149 \times 10^8 \exp(\frac{-7400}{T})$ (Pa m ³ mol ⁻¹) ⁵³
Henry's constant of H ₂ O ₂	$H_{\text{H}_2\text{O}_2}$	$6.83 \times 10^7 \exp(\frac{-7379}{T})$ (Pa m ³ mol ⁻¹) ⁵⁴
Equilibrium water content	λ_{eq}	$0.043 + 17.81a_w - 39.85a_w^2 + 36a_w^3$ ⁵⁵
Water vapor activity	a_w	$c_{w,\text{G}}RT/P_{w,\text{sat}}$
Saturation pressure	$P_{w,\text{sat}}$	$-2846.4 + 411.24(T - 273.15) - 10.544(T - 273.15)^2 + 0.16636(T - 273.15)^3$ Pa ⁵⁶

Table VIII. Summary of the source terms considered in the governing equations.

	ACL	Membrane	CCL
$S_{H_2,G}$	$\frac{-r_{HOR}}{2F} + r_{H_2,MG}$	0	$\frac{-r_{HOR}}{2F} + r_{H_2,MG}$
$S_{H_2,M}$	$-r_{H_2,MG}$	0	$-r_{H_2,MG}$
$S_{O_2,G}$	$r_{O_2,MG} + \frac{r_{2e}}{2F}$	0	$\frac{r_{4e}}{4F} + \frac{r_{2e}}{2F} + r_{O_2,MG}$
$S_{O_2,M}$	$-r_{O_2,MG}$	0	$-r_{O_2,MG}$
$S_{w,M}$	$-r_{w,MG}$	0	$\frac{r_{4e}}{2F} - r_{w,MG}$
$S_{w,G}$	$r_{w,MG}$	0	$r_{w,MG}$
S_p	$r_{HOR} + r_{2e}$	0	$r_{4e} + r_{2e} + r_{HOR}$
$S_{H_2O_2,G}$	$r_{H_2O_2,MG}$	0	$r_{H_2O_2,MG}$
$S_{H_2O_2,M}$	$\frac{r_{H_2O_2,d}}{2F} - \frac{r_{2e}}{2F} - r_{H_2O_2,MG}$	$-r_{fenton}$	$\frac{r_{H_2O_2,d}}{2F} - \frac{r_{2e}}{2F} - r_{H_2O_2,MG}$
$S_{HF,G}$	$r_{HF,MG}$	0	$r_{HF,MG}$
$S_{HF,M}$	$-r_{HF,MG}$	$4r_1 + 6r_2 + 3r_3 + 2r_{unzip} + \frac{2M_{MC}}{M_{CF_2}}r_3$	$-r_{HF,MG}$
S_s	$-r_{2e} - r_{HOR}$	-	$-r_{4e} - r_{2e} - r_{HOR}$
S_{OH}	0	$r_{fenton} - r_1 - 3r_2 - r_3 - 2r_{unzip}$	0
$S_{R_1SO_3}$	0	$-r_1$	0
$S_{R_1\alpha O}$	0	$r_1 - r_2$	0
$S_{R_1\beta O}$	0	$r_2 - r_3$	0
$S_{(CF_2)_nCOOH}$	0	$2r_3 - H(C_{CF_2,nCOOH} - c_{CF_2})r_{unzip}$	0
S_{CF_2}	0	$13r_3 - r_{unzip}$	0
S_{MC}	0	r_3	0
S_{HF}	0	$4r_1 + 6r_2 + 3r_3 + 2r_{unzip} + \frac{2M_{MC}}{M_{CF_2}}r_3$	0

Table IX. Summary of the boundary conditions applied in the simulations.

Variables	$x = 0$	$x = 1$	$x = 2$	$x = 3, 4$	$x = 5$	$x = 6$	$x = 7$
$c_{O_2,G}$	$c_{O_2,inlet}$	Continuous	Continuous	No Flux	Continuous	Continuous	No Flux
$c_{H_2,G}$	No Flux	Continuous	Continuous	No Flux	Continuous	Continuous	$c_{H_2,inlet}$
$c_{w,G}$	$c_{w,inlet}$	Continuous	Continuous	No Flux	Continuous	Continuous	$c_{w,inlet}$
$c_{H_2O_2,G}$	0	Continuous	Continuous	No Flux	Continuous	Continuous	0
$c_{HF,G}$	0	Continuous	Continuous	No Flux	Continuous	Continuous	0
$c_{H_2,M}$	-	-	No Flux	Continuous	No Flux	-	-
$c_{O_2,M}$	-	-	No Flux	Continuous	No Flux	-	-
$c_{H_2,M}$	-	-	No Flux	Continuous	No Flux	-	-
λ	-	-	No Flux	Continuous	No Flux	-	-
$c_{H_2O_2,M}$	-	-	No Flux	Continuous	No Flux	-	-
$c_{HF,M}$	-	-	No Flux	Continuous	No Flux	-	-
V_s	No Flux	Continuous	Continuous	-	Continuous	Continuous	0

comprehensive information with respect to the membrane degradation process.⁸ This dataset is utilized here for systematic validation and demonstration of the present model. The scope of this article is limited to chemical degradation, while the mechanical degradation will be included in forthcoming publications.

During the COCV AST operation, hydrogen peroxide is expected to be primarily formed at the anode from crossover oxygen. The anodic potential is near zero which is considerably negative of the equilibrium potential of the two-electron ORR and provides a high overpotential (driving force) for hydrogen peroxide formation. On the other hand, when the cell voltage is held at OCV, the simulated cathodic potential is around 0.945 V which is lower than the standard potential of four-electron ORR due to the hydrogen crossover. However, this value is still substantially positive of the standard potential of the two-electron ORR. Therefore, the peroxide formation at the cathode is negligible compared to the corresponding rate at the anode which is at a much more favorable potential for two-electron ORR.^{39,40} This situation gives rise to a hydrogen peroxide concentration gradient across the membrane and associated transport by diffusion from anode to cathode which are demonstrated by the simulated hydrogen peroxide concentration profile as shown in Figure 5. When diffusing hydrogen peroxide meets ferrous ions in the membrane, it is decom-

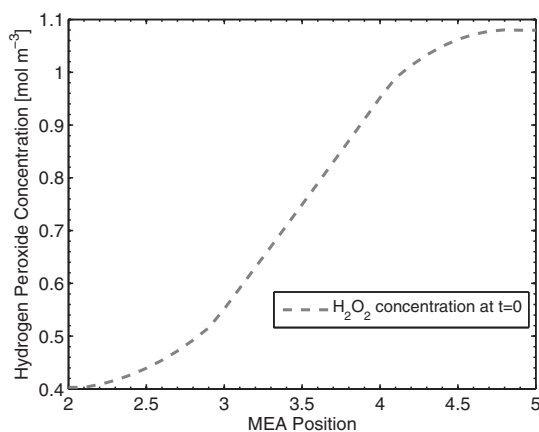


Figure 5. Simulated hydrogen peroxide concentration across the cathode CL ($2 < x < 3$), membrane ($3 < x < 4$), and anode CL ($4 < x < 5$).

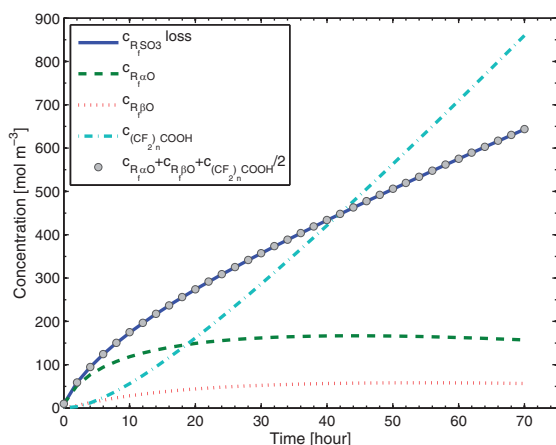


Figure 6. Simulated loss in sulfonic acid group concentration and corresponding increases in degraded ionomer species concentrations during the accelerated stress test.

posed to harmful OH· radicals that immediately attack the ionomer and thereby cause chemical membrane degradation.

The simulated concentrations of degraded ionomer species in the membrane are shown in Figure 6, which demonstrates the progression of the side chain degradation. Since all degraded ionomer species are derived from an original ionomer with a complete side chain, the loss in sulfonic acid group concentration provides an early indicator of the severity of the chemical membrane degradation. Consequently, the loss in sulfonic acid group concentration equals the sum of all degraded ionomer species concentrations divided by their corresponding stoichiometries. The results also suggest that most of the intermediate degraded ionomer species, i.e., $R_f\alpha O$ and $R_f\beta O$, are not stable in the present environment and degrade further to the carboxylic acid ionomer species, $(CF_2)_n COOH$, which is the terminal species formed according to the side chain degradation mechanism by the main chain scission event. Notably, however, main chain degradation may proceed further, as will be discussed later.

The simulated evolution of the ionomer molecular structure is compared to experimental data in Figure 7. The concentrations are normalized by the initial sulfonic acid group concentration for graphical clarity. The experimental data were obtained by solid state ^{19}F

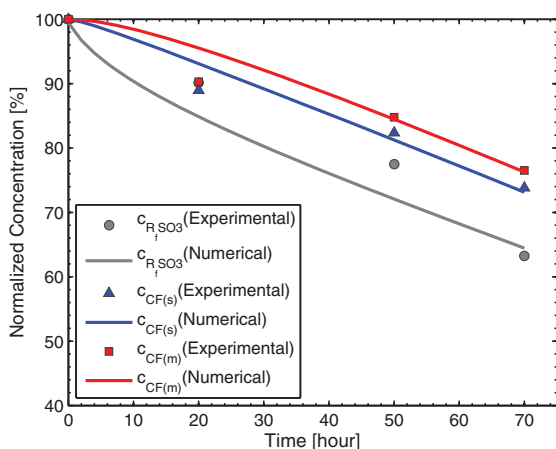


Figure 7. Simulated and measured ionomer species concentration as a function of AST operating time.

NMR measurements on partially degraded membrane samples produced and extracted during in-situ AST operation.⁸ Chemical shifts of different chemical groups containing fluorine in the ionomer were calibrated with respect to trichlorofluoromethane ($CFCl_3$) as an external standard with resonance at 0 ppm and sodium hexafluorosilicate (Na_2SiF_6) as a secondary external standard with resonance at 151.45 ppm. Then, spectral deconvolution was used to quantify the in-situ evolutions of the chemical groups, R_fSO_3 , $CF(s)$, and $CF(m)$, at various locations of the ionomer by comparing the samples before and after the COCV AST tests. According to the ionomer molecular structure shown in Figure 2, $CF(s)$ and $CF(m)$ groups represent the side chain CF and main chain CF chemical groups, respectively. In the simulation, their numerical values are calculated by:

$$c_{CF(s)} = c_{R_fSO_3} + c_{R_f\alpha O} \quad [33]$$

$$c_{CF(m)} = c_{R_fSO_3} + c_{R_f\alpha O} + c_{R_f\beta O}$$

In general, the simulation is congruous with the experimentally observed ionomer degradation: the end of the side chain is cleaved first, followed by the side chain unzipping and release of the side chain and main chain CF chemical groups. Specifically, the simulated degradation rates of the three different ionomer groups are compatible with the degradation rates observed in the NMR results, which is important for estimating the evolution of the macroscopic membrane properties with respect to fuel cell operating conditions.

In the overall chemical membrane degradation mechanism, the mass losses from side chain cleavage and unzipping, carboxylic acid group unzipping, and main chain fragmentation contribute to the dry weight reduction manifested in the measured membrane thinning and fluoride release data.⁸ The dry membrane thickness can be calculated from the dry weight of the degraded membrane by assuming a constant membrane density during degradation, i.e.,

$$L_M = \frac{W_{total}}{EW_{c_{R_fSO_3}}} L_{M,0} \quad [34]$$

where $L_{M,0}$ is the initial dry membrane thickness. The simulated evolution of membrane thickness is illustrated in Figure 8, in which the experimental membrane thickness measured by scanning electron microscope (SEM) is also shown. The linear approximation of the simulated membrane thinning rate is $0.0041t$, which results in a predicted total thinning (i.e., thickness reduction) of 53% at the end of life. The simulation quantitatively matches the experimental data, where significant membrane thinning was observed in the degraded MEA samples. In the modeling calculations, however, the individual effect of the main chain fragmentation, which is proposed to be included

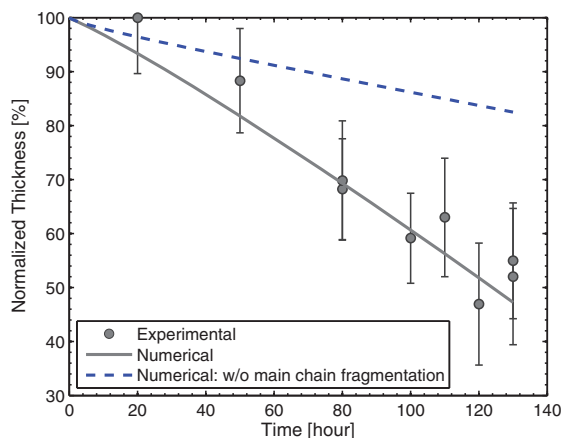


Figure 8. Simulated and measured membrane thickness as a function of AST operating time.

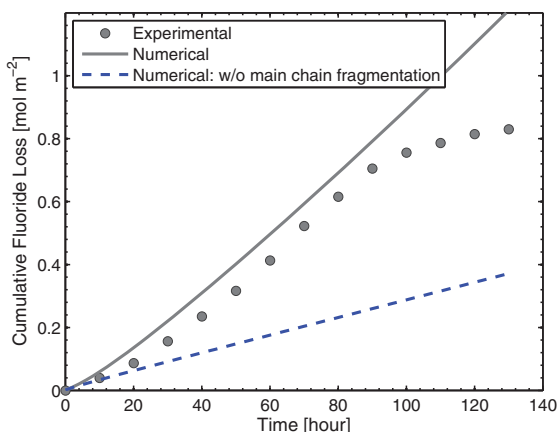


Figure 9. Simulated and measured cumulative fluoride release as a function of AST operating time.

in the overall membrane degradation mechanism, cannot be clearly shown. Therefore, the simulation of membrane thinning is repeated without main chain fragmentation and compared against the previous results in Figure 8. In this case, the simulated thinning rate is reduced to $0.00134t$ - merely one-third of the previously simulated and measured rates even though the mass losses due to side chain cleavage and unzipping, and carboxylic acid group unzipping are considered. Notably, the predicted thickness evolution highly underestimates the membrane thinning when the main chain fragmentation is ignored, thereby justifying the use of the overall degradation mechanism proposed in this work.

The predicted cumulative fluoride release (CFL) is calculated by the time integral of the HF source term in the membrane:

$$\text{CFL} = \iint S_{\text{HF}} dx dt. \quad [35]$$

Experimentally, the fluoride release rate was measured in the effluent water from the stack.⁸ The obtained numerical and experimental cumulative fluoride release is depicted in Figure 9. The simulated fluoride release shows a good agreement with experimental data across the majority of the degradation process; however, a slight deviation is observed near the end of life, beyond 100 hours of AST operation. This deviation is likely caused by the increasing hydrogen leaks across the membrane and reduced driving force for chemical membrane degradation⁸ which is not captured in the present model. The fluoride release originating from the side chain and the carboxylic acid group unzipping is also calculated and shown in the figure. Without considering the main chain fragmentation, the calculated fluoride release underestimates the fluorine loss in the membrane. This confirms that main chain fragmentation contributes a significant portion of the mass loss observed in the AST.

The simulated evolution of membrane ionic resistance during the in-situ degradation process is shown in Figure 10. The simulated results are compared in this figure to measured high frequency impedance data, representing the combined ohmic resistance per cell in the AST stack, which is dominated by membrane ionic resistance but also includes contributions from other components.⁸ The calculated resistance is shown to increase slightly during the preliminary stages of degradation known to be dominated by side chain degradation followed by a gentle decrease due to membrane thinning. These trends are qualitatively similar to the trends observed in the measured impedance, although a one-to-one comparison cannot be made in this case. It is noteworthy that despite the dramatic loss of sulfonic acid groups (40% loss after 7 AST cycles) expected to reduce the proton conductivity of the membrane, the rates of membrane thinning and

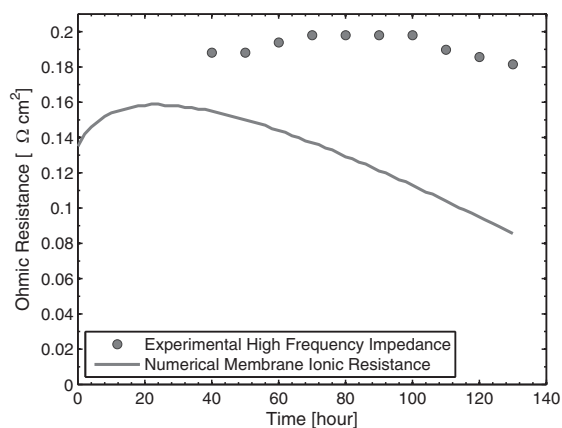


Figure 10. Comparison of simulated membrane ionic resistance and measured high frequency cell impedance as a function of AST operating time.

mass loss appear to be more significant and lead to reduced rather than increased ionic resistance as the degradation propagates from side chain to main chain.⁸

The model is also utilized to calculate the evolution of open circuit voltage (OCV) as a function of chemical membrane degradation, with results presented in Figure 11. The simulated OCV decay is approximately linear with a decay rate of 0.17 mVh^{-1} primarily attributed to the increase in hydrogen crossover rate due to membrane thinning. Specifically, the simulated crossover rate is inversely proportional to the simulated membrane thickness, i.e., $1/(1 - 0.0041t)$. This indicates that the model can capture the effect of membrane thinning on crossover and its induced effect on the fuel cell OCV. However, since the present model is 1-D and developed to simulate global chemical membrane degradation, it does not capture in-plane spatial variations in degradation rates nor mechanical degradation responsible for the localized membrane damage (pinholes, cracks, etc.) featured in the experimental results.⁸ Physical membrane damage can trigger convective flux of hydrogen gas across the membrane that greatly exceeds the potential rates of pure diffusion and imposes sizable reductions in measured OCV, as observed in the COCV AST. Recently, an ex-situ Fenton's test indicates a nonlinear dependence of chemical membrane degradation on mechanical stressors⁴¹ which

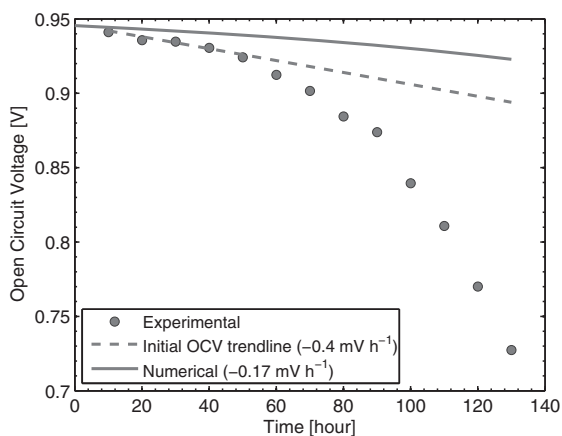


Figure 11. Simulated and measured open circuit voltage (OCV) decay during AST operation.

suggests a coupling of chemical and mechanical degradation. Simulation of mechanical degradation and combined chemical and mechanical degradation is subject to further work and will be communicated in future publications by our group.

Conclusions

An in-situ chemical membrane degradation model was developed under the auspices of recent experimental findings suggesting perfluorosulfonic acid (PFSA) ionomer degradation through a series of linked chemical degradation events during operation of polymer electrolyte fuel cells. The net action of the overall degradation mechanism was simulated using a 1-D membrane electrode assembly (MEA) based modeling framework that allowed multiscale coupling between molecular and macroscopic attributes and direct comparison with the diagnostics conducted in recent accelerated stress tests. The model demonstrated the capability to simulate the evolution of ionomer molecular structure and physicochemical membrane properties in good overall agreement with experimental data. Specifically, the effects of chemical membrane degradation on ionomer species concentrations, membrane thinning, fluoride release rates, ionic resistance, and open circuit voltage were successfully predicted by the model. The modeling analysis supports a complex chemical membrane degradation mechanism initiated by side chain cleavage and propagation toward main chain scission and fragmentation that unlocks the ability of the model to simulate macroscopic properties and trends that are difficult or impossible to measure during operation. For example, the model is capable of capturing local degradation rates due to spatial variations in hydrogen peroxide, radical, and ionomer species concentrations along the through-plane direction in the membrane and can adequately resolve their linkages with the chemical membrane degradation and real-time operating conditions. Due to its generality, the present model can be applied to examine different membrane degradation mitigation strategies and may be suitably modified to consider other types of ionomer membranes. Although the present model is implemented with a 1-D formulation, it can also be extended to capture in-plane degradation variations by 2-D/3D extensions combined with MEA performance simulations.

Acknowledgments

This research was supported by Ballard Power Systems and the Natural Sciences and Engineering Research Council of Canada through an Automotive Partnership Canada (APC) grant. The authors thank Dr. Randhir Singh, Dr. Pang-Chieh Sui, Dr. Ned Djilali, Dr. Pierre-Éric Alix Melchy, Dr. Lida Ghassemzadeh, and our colleagues at SFU FCReL and Ballard for their valuable comments and advices.

References

- M. P. Rodgers, L. J. Bonville, H. R. Kunz, D. K. Slattery, and J. M. Fenton, *Chem. Rev.*, **112**(11), 6075 (2012).
- C. S. Gittleman, F. D. Coms, and Y.-H. Lai, in *Polymer Electrolyte Fuel Cell Degradation* M. Mench, E. C. Kumbur, and T. N. Veziroglu, Editors, p. 15, Academic Press, Boston (2012).
- N. R. Andrews, S. D. Knights, K. A. Murray, S. J. McDermid, S. M. MacKinnon, and S. Ye, *U.S. Pat. 7537857*, B2 (2009).
- M.-A. Goulet, R. M. Khorasany, C. D. Torres, M. Lauritzen, E. Kjeang, G. G. Wang, and N. Rajapakse, *J. Power Sources*, **234**(0), 38 (2013).
- R. M. Khorasany, M.-A. Goulet, A. S. Alavijeh, E. Kjeang, G. G. Wang, and R. Rajapakse, *J. Power Sources*, **252**(0), 176 (2014).
- X. Huang, R. Sofasi, Y. Zou, M. Feshler, K. Reifsnider, D. Condit, S. Burlatsky, and T. Madden, *J. Polym. Sci. B Polym. Phys.*, **44**(16), 2346 (2006).
- N. Macaulay, L. Ghassemzadeh, C. Lim, M. Watson, J. Kolodziej, M. Lauritzen, S. Holdcroft, and E. Kjeang, *ECS Electrochem. Lett.*, **2**(4), F33 (2013).
- C. Lim, L. Ghassemzadeh, F. V. Hove, M. Lauritzen, J. Kolodziej, G. Wang, S. Holdcroft, and E. Kjeang, *J. Power Sources*, **257**(0), 102 (2014).
- E. Endoh, S. Terazono, H. Widjaja, and Y. Takimoto, *Electrochem. Solid-State Lett.*, **7**(7), A209 (2004).
- J. Healy, C. Hayden, T. Xie, K. Olson, R. Waldo, M. Brundage, H. Gasteiger, and J. Abbott, *Fuel Cells*, **5**(2), 302 (2005).
- L. Ghassemzadeh, K.-D. Kreuer, J. Maier, and K. Müller, *J. Phys. Chem. C*, **114**(34), 14635 (2010).
- L. Gubler, S. M. Dockheer, and W. H. Koppenol, *J. Electrochem. Soc.*, **158**(7), B755 (2011).
- L. Ghassemzadeh and S. Holdcroft, *J. Am. Chem. Soc.*, **135**(22), 8181 (2013).
- M. Damićzuk, F. D. Coms, and S. Schlick, *J. Phys. Chem. B*, **113**(23), 8031 (2009).
- M. Spulber and S. Schlick, *J. Phys. Chem. B*, **115**(43), 12415 (2011).
- Y. Nosaka, K. Ohtaka, N. Ohguri, and A. Y. Nosaka, *J. Electrochem. Soc.*, **158**(4), B430 (2011).
- M. Inaba, T. Kinumoto, M. Kiriake, R. Umebayashi, A. Tasaka, and Z. Ogumi, *Electrochim. Acta*, **51**(26), 5746 (2006).
- T. Xie and C. A. Hayden, *Polymer*, **48**(19), 5497 (2007).
- A. A. Shah, T. R. Ralph, and F. C. Walsh, *J. Electrochem. Soc.*, **156**(4), B465 (2009).
- T. Ishimoto, R. Nagumo, T. Ogura, T. Ishihara, B. Kim, A. Miyamoto, and M. Koyama, *J. Electrochem. Soc.*, **157**(9), B1305 (2010).
- T. H. Yu, Y. Sha, W.-G. Liu, B. V. Merinov, P. Shirvanyan, and W. A. Goddard, *J. Am. Chem. Soc.*, **133**(49), 19857 (2011).
- A. M. Dreizler and E. Roduner, *Fuel Cells*, **12**(1), 132 (2012).
- M. Kumar and S. J. Paddison, *J. Mater. Res.*, **27**(8), 1982 (2012).
- L. Ghassemzadeh, T. J. Peckham, T. Weissbach, X. Luo, and S. Holdcroft, *J. Am. Chem. Soc.*, **135**(42), 15923 (2013).
- C. Zhou, M. A. Guerra, Z.-M. Qiu, T. A. Zawodzinski, and D. A. Schiraldi, *Macromolecules*, **40**(24), 8695 (2007).
- C. Siegel, *Energy*, **33**(9), 1331 (2008).
- A. A. Shah, K. H. Luo, T. R. Ralph, and F. C. Walsh, *Electrochim. Acta*, **56**(11), 3731 (2011).
- M. Gummalla, V. V. Atrazhev, D. Condit, N. Cipollini, T. Madden, N. Y. Kuzminykh, D. Weiss, and S. F. Burlatsky, *J. Electrochem. Soc.*, **157**(11), B1542 (2010).
- S. Kundu, M. W. Fowler, L. C. Simon, R. Abouatallah, and N. Beydokhti, *J. Power Sources*, **183**(2), 619 (2008).
- R. Coulon, W. Bessler, and A. A. Franco, *ECS Trans.*, **25**(35), 259 (2010).
- H. S. Wroblowa, Y.-C. Pan, and G. Razumney, *J. Electroanal. Chem. Interfacial Electrochem.*, **69**(2), 195 (1976).
- M. Takasaki, Y. Nakagawa, Y. Sakiyama, K. Tanabe, K. Ookubo, N. Sato, T. Minamide, H. Nakayama, and M. Hori, *J. Electrochem. Soc.*, **160**(4), F413 (2013).
- X. Wu, X. Wang, G. He, and J. Benziger, *J. Polym. Sci. B Polym. Phys.*, **49**(20), 1437 (2011).
- J. Fimrite, B. Carnes, H. Struchtrup, and N. Djilali, *J. Electrochem. Soc.*, **152**(9), A1815 (2005).
- B. Carnes and N. Djilali, *Electrochim. Acta*, **52**(3), 1038 (2006).
- Z. Tayarani-Yoosefabad, D. Harvey, J. Bellerive, and E. Kjeang, *J. Power Sources*, Under review (2013).
- A. Nanjundappa, A. S. Alavijeh, M. E. Hannach, D. Harvey, and E. Kjeang, *Electrochim. Acta*, **110**(0), 349 (2013).
- M. Inaba, H. Yamada, J. Tokunaga, and A. Tasaka, *Electrochem. Solid-State Lett.*, **7**(12), A474 (2004).
- V. A. Sethuraman, J. W. Weidner, A. T. Haug, S. Motupally, and L. V. Protsailo, *J. Electrochem. Soc.*, **155**(1), B50 (2008).
- C. Chen and T. F. Fuller, *Electrochim. Acta*, **54**(16), 3984 (2009).
- A. Kusoglu, M. Calabrese, and A. Z. Weber, *ECS Electrochem. Lett.*, **3**(5), F33 (2014).
- C. Chan, N. Zamel, X. Li, and J. Shen, *Electrochim. Acta*, **65**(0), 13 (2012).
- J. Shen, J. Zhou, N. G. C. Astrath, T. Navessin, Z.-S. Liu, C. Lei, J. H. Rohling, D. Bessarabov, S. Knights, and S. Ye, *J. Power Sources*, **196**(2), 674 (2011).
- H. Wu, P. Berg, and X. Li, *J. Electrochem. Soc.*, **157**(1), B1 (2010).
- S. Ge, X. Li, B. Yi, and L.-M. Hsing, *J. Electrochem. Soc.*, **152**(6), A1149 (2005).
- T. Yanaka, in *Volume 27 of Studies in Environmental Science*, H. Tsunoda and M.-H. Yu, Editor, p. 81, Elsevier, New York (1986).
- R. L. McMurtrie and F. G. Keyes, *J. Am. Chem. Soc.*, **70**(11), 3755 (1948).
- E. N. Fuller, P. D. Schettler, and J. C. Giddings, *Ind. Eng. Chem.*, **58**(5), 18 (1966).
- D. M. Bernardi and M. W. Verbrugge, *J. Electrochem. Soc.*, **139**(9), 2477 (1992).
- Z. Ogumi, Z. Takehara, and S. Yoshizawa, *J. Electrochem. Soc.*, **131**(4), 769 (1984).
- R. F. Mann, J. C. Amphlett, B. A. Peppley, and C. P. Thurgood, *J. Power Sources*, **161**(2), 768 (2006).
- D. M. Bernardi and M. W. Verbrugge, *AIChE J.*, **37**(8), 1151 (1991).
- P. Brimblecombe and S. L. Clegg, *J. Atmos. Chem.*, **7**(1), 1 (1988).
- D. W. O'Sullivan, M. Lee, B. C. Noone, and B. G. Heikes, *J. Phys. Chem.*, **100**(8), 3241 (1996).
- T. E. Springer, T. A. Zawodzinski, and S. Gottesfeld, *J. Electrochem. Soc.*, **138**(8), 2334 (1991).
- M. M. Mench, *Fuel Cell Engines*, p. 93, John Wiley & Sons, New York (2008).

Appendix B: Mitigation of Chemical Membrane Degradation in Fuel Cells: Understanding the Effect of Cell Voltage and Iron Ion Redox Cycle

(Reprinted with permission from ChemSusChem, 8(6), 1072-1082 (2015). Copyright 2015, John Wiley & Sons, Inc)

Mitigation of Chemical Membrane Degradation in Fuel Cells: Understanding the Effect of Cell Voltage and Iron Ion Redox Cycle

Ka Hung Wong and Erik Kjeang^{*[a]}

Chemical membrane degradation through the Fenton's reaction is one of the main lifetime-limiting factors for polymer-electrolyte fuel cells. In this work, a comprehensive, transient membrane degradation model is developed to capture and elucidate the complex in situ degradation mechanism. A redox cycle of iron ions is discovered within the membrane electrolyte assembly, which sustains the Fe^{II} concentration and results in the most severe chemical degradation at open circuit volt-

age. The cycle strength is critically reduced at lower cell voltages, which leads to an exponential decrease in Fe^{II} concentration and associated membrane degradation rate. When the cell voltage is held below 0.7 V, a tenfold reduction in cumulative fluoride release is achieved, which suggests that intermediate cell voltage operation would efficiently mitigate chemical membrane degradation and extend the fuel cell lifetime.

Introduction

In low-temperature polymer electrolyte fuel cells (PEFCs), perfluorosulfonic acid (PFSA) ionomer membranes are currently the industrial standard material for the electrolyte component. The high performance of fuel cell achieved using these PFSA electrolytes is attributed to their high proton conductivity at low temperatures, superior electrical insulation, relatively low reactant permeation, and thin-film structure with high mechanical stability. However, the ionomer membrane can undergo various forms of degradation in the fuel cell environment, which largely deteriorates its advantages and limits the durability and lifetime of PEFCs.^[1,2] Chemical membrane degradation is a primary factor that dramatically weakens the physico-chemical properties of the membrane and initiates the overall degradation processes.^[3,4] Combined with mechanical stress induced by hygrothermal fluctuations in the membrane electrode assembly (MEA),^[5-9] physical damage has been observed and shown to cause lifetime-limiting hydrogen leaks across the membrane.^[4,10]

Reactions of highly reactive radicals with the PFSA ionomer molecular structure is generally considered to be the initial progress of chemical membrane degradation in PEFCs.^[11-15] This hypothesis is corroborated by the in situ detection of hydroxyl ([•]OH), hydroperoxyl ([•]OOH), and hydrogen (H[•]) radicals and degraded ionomer species comprising oxygen- and carbon-centered radicals utilizing an electron spin resonance (ESR) spectrometer^[16,17] or a fluorescence probe.^[18] The hydroxyl radical is the "usual suspect" responsible for the chemical degradation^[12,14] and can initiate the formation of hydroperox-

yl and hydrogen radicals.^[14] Hydroxyl radicals can be generated from decomposition of hydrogen peroxide caused by metal contaminants.^[19,20] Among these contaminants, the Fe^{II} ion is found to have the highest impact on the rate of chemical degradation.^[21] This finding is also consistent with the ex situ Fenton's test in which an increased formation of fluoride ions and hydroxyl radicals was observed in Fe^{II}-exchanged membranes compared with as-received and Pt-dispersed membranes.^[22] Indeed, a higher Fe^{II} ion concentration has a stronger impact on the degradation rate as revealed by the decomposition of CF₂ in the polymer backbone detected by means of X-ray photoelectron spectroscopy.^[23]

In fuel cell membranes, the presence of iron traces is usually a result of contamination during fabrication and/or operation,^[24] and the stable form of iron can be in either of the ferrous (Fe^{II}) or ferric (Fe^{III}) ion forms according to the Pourbaix diagram of iron.^[25] The balance between the two oxidation states of iron plays an important role in hydroxyl radical formation.^[14] Unfortunately, the concentration, transport, and formation/consumption of ferric/ferrous ions inside a fuel cell are difficult or impossible to measure quantitatively (e.g., by X-ray fluorescence spectroscopy). Modeling the transport and reactions of iron ions and their effect on chemical membrane degradation can complement the experimental findings to provide insights on the fundamental understanding and mitigation strategies. In literature, although hydroxyl radical formation caused by Fe^{II} is generally considered, iron ion transport and redox chemistry are neglected in existing membrane degradation models.^[14,26-28] To better understand the role of iron ions in PEFCs, a comprehensive, transient in situ membrane degradation model is developed in this work, which accounts for the iron ion transport (diffusion and migration), iron ion redox chemistry, and chemical membrane degradation through hydroxyl radical attack. The model is then applied to scrutinize

[a] K. H. Wong, Dr. E. Kjeang
School of Mechatronic Systems Engineering
Simon Fraser University
250-13450 102 Avenue, Surrey, BC V3T0A3 (Canada)
Fax: (+1) 778-782-7514
E-mail: ekjeang@sfu.ca

the realistic iron distribution inside the MEA with respect to operating conditions of the fuel cell. A special focus of this work is to utilize the obtained model to elucidate the enigmatic effect of the cell voltage on the chemical membrane degradation.^[4,29] Based on the simulated results, mitigation of chemical membrane degradation is also discussed.

Model Formulation and Governing Equations

The modeling framework used herein was targeted for chemical degradation of PFSA ionomer membranes in hydrogen PEFCs. The degradation model was extended from the recently established in situ chemical membrane degradation model^[28] to involve the transport and redox reactions of the Fe^{II}/Fe^{III} ions and provide more comprehensive descriptions on the radical reactions and the mechanisms of membrane degradation. To simulate the degradation in a realistic fuel cell environment, a 1D MEA performance model was derived and solved in the computational domain illustrated schematically in Figure 1. The domain represents a standard MEA consisting of a membrane, catalyst layers (CLs), and gas diffusion layers (GDLs) with separate macroporous substrate and microporous layer (MPL) subdomains. The x-axis represents the through-plane direction and starts at the cathode gas channel (GC) and GDL interface ($x=0$). All MEA layers were normalized by thickness; the MEA dimensions and physical parameters used in the model are listed in Table 1. Three distinct phases were considered in the model: the gas phase and solid phase in GDLs and CLs and the ionomer phase in CLs and membrane. The various species and transport phenomena in all MEA layers are also indicated in the schematic. Transport phenomena are governed by the conservation of mass, species, and charge:^[28]

$$\frac{\partial}{\partial t}(\epsilon c_i) + \nabla \cdot J_i = S_i \quad (1)$$

In Equation (1), c_i , J_i , and S_i represent the concentration, flux, and source of species i in the given phase, respectively, and ϵ denotes the volume fraction of the given phase.

Membrane degradation mechanism

The typical PFSA ionomer contained a polytetrafluoroethylene (PTFE) backbone decorated with sulfonic-acid side chains, as depicted in Figure 2, using Nafion as an example. The basic ionomer properties are listed in Table 2. A pure PTFE backbone was assumed in the model because main chain defects have been effectively eliminated by ionomer manufacturers.^[37] Therefore, the membrane degradation is assumed to be induced by side chain degradation due to hydroxyl radical attack, which is supported by recent experimental findings.^[4,15] The mechanism was extended

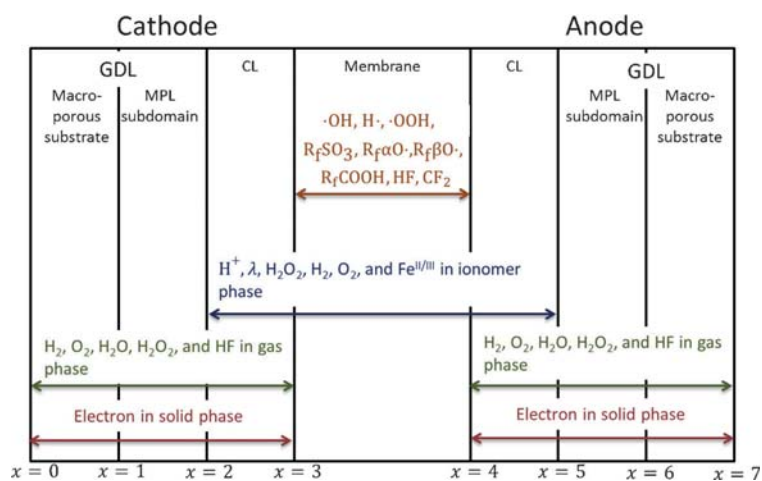


Figure 1. Schematic of the computational domain, including membrane, CLs, and GDLs (consisting of a macroporous substrate and a microporous layer). The x-axis represents the through-plane direction and starts at the GC and GDL interface. Gas and electron transport is considered in GDLs and CLs, and transport in the ionomer phase is considered in the CLs and membrane. Chemical degradation is considered in the membrane.

Table 1. Structural and physical parameters used in the model.

Parameter	Symbol	Value
Thickness [μm]		
GDL macroporous substrate	L_{GDL}	250
MPL subdomain	L_{MPL}	25
catalyst layer	L_{CL}	15
beginning of life (BOL) membrane	$L_{\text{m},0}$	30
Porosity		
GDL macroporous substrate	ϵ_{GDL}	0.78 ^[30]
MPL subdomain	ϵ_{MPL}	0.65 ^[30]
catalyst layer	ϵ_{CL}	0.4 ^[31]
ionomer fraction in membrane	ϵ_{m}	0.3 ^[32]
Molar mass [g mol^{-1}]		
hydrogen	M_{H_2}	2
oxygen	M_{O_2}	32
nitrogen	M_{N_2}	28
water vapor	M_{w}	18
Diffusion volume		
hydrogen	V_{H_2}	7.07 ^[33]
oxygen	V_{O_2}	16.6 ^[33]
nitrogen	V_{N_2}	17.9 ^[33]
water vapor	V_{w}	12.7 ^[33]
Molar volume of water [$\text{m}^3 \text{mol}^{-1}$]		
	V_{w}	1.8×10^{-5} ^[34]
Water concentration [mol m^{-3}]		
	C_{w}	5.56×10^4
Faraday's constant [C mol^{-1}]		
	F	96485
Gas constant [$\text{J K}^{-1} \text{mol}^{-1}$]		
	R	8.314

from the degradation model presented in a previous publication^[28] and is summarized in Figure 3.

First, side chain cleavage was initiated by hydroxyl radical attack at the second ether group, αOCF_2 , in the side chain to form an oxygen-centered radical, $\text{R}_f\alpha\text{O}^\cdot$. Stepwise degradation propagated along the side chain through the unzipping reaction until main

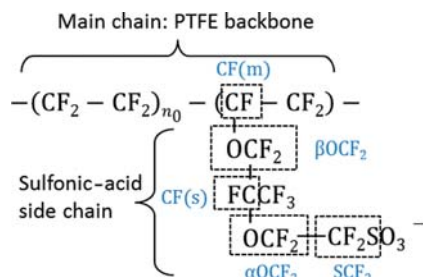


Figure 2. The molecular structure of Nafion (the average number of $\text{CF}_2\text{-CF}_2$ in the main chain, n_0 , is 6.5 for an equivalent weight (EW) of roughly 1.1 kg mol^{-1}).

Table 2. Ionomer parameters used in the model.			
Parameter	Symbol	Value	Unit
Nafion properties			
dry membrane density	ρ_m	1980 ^[35]	$[\text{kg m}^{-3}]$
BOL equivalent weight	EW_0	1.093	$[\text{kg mol}^{-1}]$
BOL average number of CF_2 per SO_3	$2n_0 + 1$	14	
BOL molar volume of ionomer	$V_{m,0}$	$\frac{\text{EW}_0}{\rho_m}$	$[\text{m}^3 \text{mol}^{-1}]$
BOL backbone concentration	$c_{\text{backbone},0}$	20 ^[36]	$[\text{mol m}^{-3}]$
Average molecular weight $[\text{g mol}^{-1}]$			
R_iSO_3	$M_{\text{R}_i\text{SO}_3}$	1093	
$\text{R}_i\alpha\text{O}^\bullet$	$M_{\text{R}_i\alpha\text{O}^\bullet}$	913	
$\text{R}_i\beta\text{O}^\bullet$	$M_{\text{R}_i\beta\text{O}^\bullet}$	747	
CF_2 group	M_{CF_2}	50	
COOH	M_{COOH}	45	

chain scission occurred by hydroxyl radical attack of the βO^\bullet intermediate ionomer species.^[13,38] The carboxylic acid groups formed after the main chain scission further degraded through the well-established main chain unzipping reaction (Reaction 4 in Table 3).^[35,38] Continuous backbone unzipping could result in the loss of small side chain fragments as in Figure 3 e. As the degradation progresses, widespread main chain scission events induced by side chain degradation in multiple locations might also result in the loss of main chain fragments from the membrane (Figure 3 f). The additional material loss contributed by main chain degradation

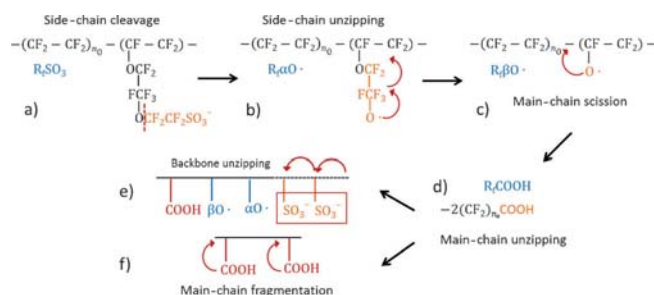


Figure 3. Schematic of the membrane degradation mechanism caused by hydroxyl radical attack. Side chain cleavage is initiated by hydroxyl radical attack at the second ether group in the side chain (a), followed by stepwise propagation along the side chain (b). Main chain scission occurs by hydroxyl radical attack of the βO^\bullet intermediate ionomer species (c). The carboxylic acid groups formed after the main chain scission event degrades through the chain-unzipping reaction (d). Continuous backbone unzipping induces e) side chain and f) main chain fragments.

Table 3. Overview of the chemical and electrochemical reactions considered in the model.

Label	Reaction
1	$\text{R}_i\text{SO}_3 + \cdot\text{OH} \rightarrow \text{R}_i\alpha\text{O}^\bullet + \text{HOFCF}_2\text{CF}_2\text{SO}_3$
2	$\text{R}_i\alpha\text{O}^\bullet + 3 \cdot\text{OH} \rightarrow \text{R}_i\beta\text{O}^\bullet + \text{CF}_3 + 3 \text{HF} + 2 \text{CO}_2$
3	$\text{R}_i\beta\text{O}^\bullet + 2 \text{H}_2\text{O} + \cdot\text{OH} \rightarrow \text{R}_i\text{COOH} + 3 \text{HF}$
4	$-(\text{CF}_2)_{2n_0}\text{COOH} + 2n_0 \cdot\text{OH} \rightarrow 2n_0 \text{CO}_2 + 4n_0 \text{HF} + \text{COOH}$
5	$\text{Fe}^{\text{II}} + \text{H}_2\text{O}_2 + \text{H}^+ \rightarrow \text{Fe}^{\text{III}} + \cdot\text{OH} + \text{H}_2\text{O}$
6	$\text{Fe}^{\text{III}} + \text{H}_2\text{O}_2 \rightarrow \text{Fe}^{\text{II}} + \cdot\text{OOH} + \text{H}^+$
7	$\text{Fe}^{\text{II}} + \cdot\text{OOH} + \text{H}^+ \rightarrow \text{Fe}^{\text{III}} + \text{H}_2\text{O}_2$
8	$\text{Fe}^{\text{III}} + \cdot\text{OOH} \rightarrow \text{Fe}^{\text{II}} + \text{H}^+ + \text{O}_2$
9	$\text{Fe}^{\text{II}} + \cdot\text{OH} + \text{H}^+ \rightarrow \text{Fe}^{\text{III}} + \text{H}_2\text{O}$
10	$\cdot\text{OH} + \text{H}_2 \rightarrow \text{H}^+ + \text{O}_2$
11	$\text{H}^+ + \text{O}_2 \rightarrow \cdot\text{OOH}$
12	$\text{Fe}^{\text{III}} + \text{e}^- \rightarrow \text{Fe}^{\text{II}} \quad E_0 = 0.77 \text{ V}$
13	$2 \text{H}^+ + 2 \text{e}^- \rightarrow \text{H}_2 \quad E_0 = 0 \text{ V}$
14	$\text{O}_2 + 4 \text{H}^+ + 4 \text{e}^- \rightarrow 2 \text{H}_2\text{O} \quad E_0 = 1.23 \text{ V}$
15	$\text{O}_2 + 2 \text{H}^+ + 2 \text{e}^- \rightarrow \text{H}_2\text{O}_2 \quad E_0 = 0.695 \text{ V}$
16	$\text{H}_2\text{O}_2 + 2 \text{H}^+ + 2 \text{e}^- \rightarrow 2 \text{H}_2\text{O} \quad E_0 = 1.76 \text{ V}$

was recently confirmed experimentally.^[4] The overall mechanism of membrane degradation can be summarized as a series of chemical equations, which are represented by Reactions 1–4 listed in Table 3. The corresponding reaction kinetics is given by Equations (2)–(5):

$$r_1 = k_1 \theta c_{\text{R}_i\text{SO}_3} c_{\cdot\text{OH}} \quad (2)$$

$$r_2 = k_2 \theta c_{\text{R}_i\alpha\text{O}^\bullet} c_{\cdot\text{OH}} \quad (3)$$

$$r_3 = k_3 \theta c_{\text{R}_i\beta\text{O}^\bullet} c_{\cdot\text{OH}} \quad (4)$$

$$r_4 = k_4 \theta c_{\text{R}_i\text{COOH}} c_{\cdot\text{OH}} \quad (5)$$

where θ accounts for the impact of membrane swelling on the concentration of dissolved ionomer species.^[26]

Iron ion transport

Iron (ferric/ferrous) ions are charged species, and hence their fluxes in the ionomer phase can be described by the Nernst–Planck equation:^[39,40]

$$J_i = -D_i \nabla c_i - u_i z_i c_i F \nabla \varphi_m \quad (6)$$

where the first term represents the ionic diffusion due to the concentration gradient and the second term represents the ion migration due to the gradient of ionomer potential, φ_m . In Equation (6), z_i denotes the charge number of species i , and the diffusivity, D_i , and mobility, u_i , of species i are related by the Nernst–Einstein relation, $D_i = u_i RT$. The Fe^{II} ion mobility was assumed to be similar to other divalent ions, that is, $1.25 \times 10^{-13} \text{ smol kg}^{-1}$, and the Fe^{III} ion mobility was $1.83 \times 10^{-14} \text{ smol kg}^{-1}$.^[41] Convective ion transport due to water crossover was neglected.

The chemical reactions involving iron ions in the membrane and CLs are shown in Table 3. Reaction 5 in Table 3 is known as the Fenton's reaction describing the metal-ion-catalyzed decomposition of hydrogen peroxide into radical species in the membrane. Reactions 6–9 in Table 3 are the reactions between iron ions, hydrogen peroxide, and radical species formed in the membrane. The kinetics of Reactions 5–9 are given by Equations (7)–(11):

$$r_5 = k_5 \theta c_{\text{Fe}^{\text{II}}} c_{\text{H}_2\text{O}_2} \quad (7)$$

$$r_6 = k_6 \theta c_{\text{Fe}^{\text{III}}} c_{\text{H}_2\text{O}_2} \quad (8)$$

$$r_7 = k_7 \theta c_{\text{Fe}^{\text{II}}} c_{\text{OOH}} \quad (9)$$

$$r_8 = k_8 \theta c_{\text{Fe}^{\text{III}}} c_{\text{OOH}} \quad (10)$$

$$r_9 = k_9 \theta c_{\text{Fe}^{\text{II}}} c_{\text{OH}} \quad (11)$$

The hydroperoxyl radical involved in the reactions formed based on reactions between hydroxyl radical, hydrogen, and oxygen as listed in Table 3 (Reactions 10 and 11).^[14] The role of the secondary types of radicals (i.e., hydroperoxyl and hydrogen radicals) in the chemical membrane degradation was neglected because they are much less reactive compared to the hydroxyl radical, which has the highest redox potential among these radicals.^[2] Reaction 12 represents the electrochemical reaction for the $\text{Fe}^{\text{II}}/\text{Fe}^{\text{III}}$ redox couple that can be either reduced or oxidized at the CLs. The kinetics of this reaction [Eq. (12)] are described by the Butler–Volmer equation:^[42,43]

$$r_{12} = a k_{12} F \sqrt{c_{\text{Fe}^{\text{II}}} c_{\text{Fe}^{\text{III}}}} \left[\exp\left(\frac{F \eta_{12}}{2RT}\right) - \exp\left(\frac{-F \eta_{12}}{2RT}\right) \right] \quad (12)$$

Parameters and variables used in calculating the chemical kinetics are listed in Table 4.

Gas species transport

Diffusion was assumed to be the dominant mechanism for gas-phase transport as the convection in the through-plane direction is minimal and can be neglected. The diffusive flux is given by:

$$J_i = -D_i^{\text{eff}} \nabla c_i \quad (13)$$

where D_i^{eff} denotes the effective diffusivity, which is related to the diffusivity D_i by:^[47,48]

$$D_i^{\text{eff}} = \begin{cases} 0.407 D_i & \text{in GDL macroporous substrate} \\ 0.18 D_i & \text{in MPL subdomain} \\ \varepsilon_g^\tau D_i & \text{in CL} \end{cases} \quad (14)$$

where ε_g is the porosity and the Bruggeman approximation,^[26,28] that is, $\tau = 1.5$, was applied. The calculation of the diffusivity is tabulated in Table 5.

The hydrogen oxidation reaction (HOR) and four-electron oxygen reduction reaction (ORR), Reactions 13 and 14 in Table 3, are the regular electrochemical reactions occurring in PEFCs, and their reaction rates can be described by the Butler–Volmer kinetics [Eqs. (15) and (16)].^[28]

$$r_{13} = a i_{13,0} \frac{c_{\text{H}_2,\text{eq}}}{c_{\text{H}_2,\text{ref}}} \left[\exp\left(\frac{F \eta_{13}}{2RT}\right) - \exp\left(\frac{-F \eta_{13}}{2RT}\right) \right] \quad (15)$$

$$r_{14} = a i_{14,0} \frac{c_{\text{O}_2,\text{eq}}}{c_{\text{O}_2,\text{ref}}} \left[\exp\left(\frac{F \eta_{14}}{RT}\right) - \exp\left(\frac{-F \eta_{14}}{RT}\right) \right] \quad (16)$$

Table 4. Parameters associated with calculation of reaction kinetics.

Parameter	Symbol	Value
Local overpotential [V]	η_i	$\varphi_s - \varphi_m - E_{i,\text{eq}}$
Volumetric specific surface area [m^{-1}]	a	10^4
Effect of membrane swelling	θ	$\frac{14(V_{m,0} + \lambda V_W)}{\lambda(V_{m,0} + 14V_W)}$
Exchange current density [A m^{-2}]		
Reaction 13 (HOR)	$i_{13,0}$	10^5
Reaction 14 ($4e^-$ ORR)	$i_{14,0}$	40
Reaction 15 ($2e^-$ ORR)	$i_{15,0}$	50
Reaction 16	$i_{16,0}$	10^{-7}
Reference concentration [mol m^{-3}]		
hydrogen	$c_{\text{H}_2,\text{ref}}$	40.88
oxygen	$c_{\text{O}_2,\text{ref}}$	40.88
hydrogen peroxide	$c_{\text{H}_2\text{O}_2,\text{ref}}$	40.88
Transfer coefficient (reaction 16)	α_{16}	0.32 ^[44]
H_2O_2 selectivity	$\chi_{\text{H}_2\text{O}_2}$	$\left[\frac{1980 + 32.4\lambda}{1167.4 \text{EW}(1 + 0.0648\lambda)} \right]^2$ ^[45]
Reaction rate constant [$\text{m}^3 \text{mol}^{-1} \text{s}^{-1}$]		
Reaction 1	k_1	3.7×10^3 ^[46]
Reaction 2	k_2	3.75×10^4
Reaction 3	k_3	7.5×10^4
Reaction 4	k_4	5.8×10^3
Reaction 5	k_5	6.3×10^{-2} ^[14]
Reaction 6	k_6	4×10^{-8} ^[14]
Reaction 7	k_7	1.2×10^3 ^[14]
Reaction 8	k_8	20 ^[14]
Reaction 9	k_9	2.5×10^5 ^[14]
Reaction 10	k_{10}	4.3×10^4 ^[14]
Reaction 11	k_{11}	1.2×10^7 ^[14]
Reaction 12	k_{12}	10^{-7} [m s^{-1}]
Process (f)	k_{mc}	0.035 [$\text{mol m}^{-3} \text{s}^{-1}$]
Nernst potential [V]		
Reaction 12 (Fe ion couple)	$E_{12,\text{eq}}$	$0.77 + \ln\left(\frac{c_{\text{Fe}^{\text{III}}}}{c_{\text{Fe}^{\text{II}}}}\right)$
Reaction 13 (HOR)	$E_{13,\text{eq}}$	0
Reaction 14 ($4e^-$ ORR)	$E_{14,\text{eq}}$	$1.23 - 0.9 \times 10^{-3}(T - 298.15)$
Reaction 15 ($2e^-$ ORR)	$E_{15,\text{eq}}$	0.695
Reaction 16	$E_{16,\text{eq}}$	1.76
Transfer coefficient (reaction 16)	α_{16}	0.32 ^[44]
H_2O_2 selectivity	$\chi_{\text{H}_2\text{O}_2}$	$\left[\frac{1980 + 32.4\lambda}{1167.4 \text{EW}(1 + 0.0648\lambda)} \right]^2$ ^[45]

The gas species (hydrogen, oxygen, water vapor, hydrogen peroxide, and hydrogen fluoride) can dissolve in the ionomer phase, which can be described by interfacial mass transport. The rate of the transport is formulated as Equation (17):

$$r_{i,\text{mg}} = k_{i,\text{m}}(c_{i,\text{m}} - c_{i,\text{eq}}) \quad (17)$$

in which $c_{i,\text{eq}}$ represents the ionomer phase concentration in equilibrium with respect to the gas phase concentration according to Henry's law. Readers are referred to a previous publication^[28] for the variables and parameters used in modeling the interfacial mass transport.

Table 5. Constitutive relationships and parameters associated with calculation of diffusivity.

Description	Expression
Gas-phase diffusivity [$10^{-5} \text{ m}^2 \text{ s}^{-1}$]	
D_{HF}	$2.6^{[49]}$
$D_{\text{H}_2\text{O}_2}$	$1.88^{[50]}$
$D_{\text{t,H}_2}$	$\frac{32.042T^{1.75} \sqrt{\frac{1}{M_i} + \frac{1}{M_{\text{H}_2}}}}{P \left(v_i^2 + v_{\text{H}_2}^2 \right)^2}$ [33]
$D_{\text{t,N}_2}$	$\frac{32.042T^{1.75} \sqrt{\frac{1}{M_i} + \frac{1}{M_{\text{N}_2}}}}{P \left(v_i^2 + v_{\text{N}_2}^2 \right)^2}$ [33]
P [Pa]	$\sum_i c_i RT$
Ionomer-phase diffusivity [$\text{m}^2 \text{ s}^{-1}$]	
$D_{\text{Fe}^{II}/\text{Fe}^{III}}^{\text{eff}}$	$\frac{u_{\text{Fe}^{II}}}{RT}$
D_{H_2}	$4.1 \times 10^{-7} \exp\left(-\frac{2602}{T}\right)$ [51]
D_{O_2}	$3.1 \times 10^{-7} \exp\left(-\frac{2768}{T}\right)$ [51]
$D_{\text{H}_2\text{O}_2}$	D_w (water diffusivity)
D_{HF}	1.5×10^{-10}
D_{OH}	0
$D_{\text{R}_2\text{SO}_3}$	0
$D_{\text{R}_4\text{HO}^+}$	0
$D_{\text{R}_4\text{BO}^+}$	0
$D_{\text{R}_2\text{COOH}}$	0
D_{CF_2}	0

Ionomer species transport

Almost all ionomer phase species (except protons, water molecules, and the $\text{Fe}^{II}/\text{Fe}^{III}$ couple) are governed by diffusive transport; thus, their fluxes are also described by Equation (13). Their diffusivities in the membrane are shown in Table 5 whereas the values in the CLs were calculated by using the Bruggeman approximation.^[26,28]

In PEFCs, proton conduction, diffusion of dissolved water in the ionomer phase, and electro-osmotic drag are the dominant mechanisms governing proton [Eq. (18)] and water transport [Eq. (19)] phenomena in the ionomer phase of the membrane and CLs.^[52]

$$J_p = -\sigma_p^{\text{eff}} \nabla \phi_m \quad (18)$$

$$J_w = -D_w^{\text{eff}} c_{\text{R}_2\text{SO}_3} \nabla \lambda + n_d J_p \quad (19)$$

Here, n_d is the electro-osmotic drag coefficient, and J_p and J_w are the proton and water flux in the ionomer phase. In these equa-

tions, the ionomer potential, ϕ_m , and the water content, λ , in the ionomer phase are solved. The binary friction membrane model (BFM2) introduced by Fimrite et al. and Carnes et al.^[53,54] was applied to calculate the proton conductivity, water diffusivity, and electro-osmotic drag coefficient. Readers are referred to the previous publication^[28] for the variables used in BFM2. In the CLs, the effective proton conductivity and water diffusivity of the ionomer phase species, σ_p^{eff} and D_w^{eff} , were calculated using the Bruggeman approximation.^[26,28]

Hydrogen peroxide can form via the two-electron ORR (Reaction 15 in Table 3) especially at low potentials and relative humidity,^[45] and its kinetics can also be calculated using the Butler-Volmer equation [Eq. (20)].^[26]

$$r_{15} = a i_{15,0} \frac{c_{\text{O}_2,\text{eq}}}{c_{\text{O}_2,\text{ref}}} \chi_{\text{H}_2\text{O}_2} \exp\left(-\frac{F \eta_{15}}{RT}\right) \quad (20)$$

where $\chi_{\text{H}_2\text{O}_2}$ denotes the selectivity of hydrogen peroxide formation, which was measured experimentally.^[45] On the other hand, hydrogen peroxide reduction (Reaction 16 in Table 3) can occur at the platinum surface in the CLs [Eq. (21)].^[44]

$$r_{16} = 2 a i_{16,0} \frac{c_{\text{H}_2\text{O}_2}}{c_{\text{H}_2\text{O}_2,\text{ref}}} \sinh\left(\frac{\alpha_{16} F \eta_{16}}{RT}\right) \quad (21)$$

Electron transport

Electron conduction in GDLs and CLs can be described by Equation (22):

$$I = -\sigma_s^{\text{eff}} \nabla \phi_s \quad (22)$$

where I and ϕ_s are the current and the potential of the solid phase (carbon/graphite), respectively. The through-plane electronic conductivity of graphite, σ_s , is 1250 S m^{-1} ^[26] whereas the values in the porous media are calculated by using the Bruggeman approximation.^[26,28]

Table 6. Summary of the source terms considered in the governing equations.

Source term	ACL ^[a]	Membrane	CCL ^[b]
$S_{\text{H}_2,\text{g}}$	$-\frac{r_{11}}{2F} + r_{\text{H}_2,\text{mg}}$	–	$\frac{r_{11}}{2F} + r_{\text{H}_2,\text{mg}}$
$S_{\text{H}_2,\text{m}}$	$-r_{\text{H}_2,\text{mg}}$	$-r_{10}$	$-r_{\text{H}_2,\text{mg}}$
$S_{\text{O}_2,\text{g}}$	$\frac{r_{15}}{2F} + r_{\text{O}_2,\text{mg}}$	–	$\frac{r_{15}}{2F} + \frac{r_{15}}{2F} + r_{\text{O}_2,\text{mg}}$
$S_{\text{O}_2,\text{m}}$	$-r_{\text{O}_2,\text{mg}}$	$r_8 + r_{10} - r_{11}$	$-r_{\text{O}_2,\text{mg}}$
$S_{\text{w,g}}$	$r_{\text{w,mg}}$	–	$r_{\text{w,mg}}$
$S_{\text{w,m}}$	$-\frac{r_{16}}{F} - r_{\text{w,mg}}$	$-r_3 + r_5 + r_9$	$-\frac{r_{16}}{2F} - \frac{r_{16}}{2F} - r_{\text{w,mg}}$
S_p	$r_{13} + r_{15} + r_{16}$	$-r_5 + r_6 - r_7 + r_8 - r_9$	$r_{13} + r_{14} + r_{15} + r_{16}$
$S_{\text{H}_2\text{O}_2,\text{g}}$	$r_{\text{H}_2\text{O}_2,\text{mg}}$	–	$r_{\text{H}_2\text{O}_2,\text{mg}}$
$S_{\text{H}_2\text{O}_2,\text{m}}$	$-\frac{r_{13}}{2F} - \frac{r_{15}}{2F} - r_{\text{H}_2\text{O}_2,\text{mg}}$	$-r_5 - r_6 + r_7$	$-\frac{r_{13}}{2F} + \frac{r_{15}}{2F} - r_{\text{H}_2\text{O}_2,\text{mg}}$
$S_{\text{HF,g}}$	$r_{\text{HF,mg}}$	–	$r_{\text{HF,mg}}$
$S_{\text{HF,m}}$	$-r_{\text{HF,mg}}$	$4r_1 + 6r_2 + 3r_3 + 4n_0 r_4 + 4n_0 r_{\text{mc}} + 11 r_{\text{sc,R}_2\text{SO}_3} + 7 r_{\text{sc,R}_4\text{HO}^+} + r_{\text{sc,R}_4\text{BO}^+}$	$-r_{\text{HF,mg}}$
S_s	$r_{12} + r_{13} + r_{15} + r_{16}$	–	$r_{12} + r_{13} + r_{14} + r_{15} + r_{16}$
S_{OH}	–	$-r_1 - 3r_2 - r_3 - 4n_0 r_4 + r_5 - r_9 - r_{11}$	–
S_{H^+}	–	$r_{10} - r_{11}$	–
S_{OOH}	–	$r_6 - r_7 - r_8 + r_{11}$	–
$S_{\text{R}_2\text{SO}_3}$	–	$-r_1 - r_{\text{sc,R}_2\text{SO}_3}$	–
$S_{\text{R}_4\text{HO}^+}$	–	$r_1 - r_2 - r_{\text{sc,R}_4\text{HO}^+}$	–
$S_{\text{R}_4\text{BO}^+}$	–	$r_2 - r_3 - r_{\text{sc,R}_4\text{BO}^+}$	–
$S_{\text{R}_2\text{COOH}}$	–	$2r_3 - r_{\text{sc,R}_2\text{COOH}} - 2r_{\text{mc}}$	–
S_{CF_2}	–	$-r_3 - 2n_0 r_4 - 2n_0 r_{\text{mc}}$	–

[a] Anode catalyst layer. [b] Cathode catalyst layer

Source terms

In the model, the source terms, S_i , in the governing equations included the generation and consumption caused by reactions and interfacial mass transport. All the source terms considered are summarized in Table 6. The source terms of the ionomer species associated with chemical membrane degradation were determined according to the detailed mechanisms shown in Figure 3. It was assumed that all fluorine released during the degradation was in the form of hydrogen fluoride. The rate of the loss of side chain fragments, $r_{sc,i}$ is related to the backbone-unzipping rate given by Equation (23):

$$r_{sc,i} = \frac{c_i r_4}{\sum_i c_i}, \quad i = R_f SO_3, R_f \alpha O^-, R_f \beta O^-, R_f COOH \quad (23)$$

while the rate of the loss of main chain fragmentation, r_{mc} is inversely proportional to the average length of the backbone in the membrane [Eq. (24)]:

$$r_{mc} = k_{mc} H \left(c_{R_f COOH} \right) \frac{\frac{c_{R_f COOH}}{2} + c_{backbone,0}}{c_{CF_2}} \quad (24)$$

where $c_{backbone,0}$ and H are the initial concentration of the backbone in the membrane and the Heaviside step function, respectively.

Initial and boundary conditions

The boundary conditions are summarized in Table 7. Hydrogen peroxide and hydrogen fluoride concentrations in the gas phase were assumed to be zero at the gas channel and GDL interfaces. Zero flux was assumed at the CL and MPL interfaces ($x=2$ and 4) for the species dissolved in the ionomer phase. The inlet hydrogen, oxygen, and water vapor concentrations, that is, $c_{H_2, \text{inlet}}$, $c_{O_2, \text{inlet}}$ and $c_{w, \text{inlet}}$, respectively, were calculated according to the operating conditions used in the accelerated stress test (AST).¹⁴

Table 7. Summary of the boundary conditions applied in the simulations (cont. = continuous).

Variable	$x=0$	$x=1$	$x=2$	$x=3\&4$	$x=5$	$x=6$	$x=7$
$c_{O_2, g}$	$c_{O_2, \text{inlet}}$	cont.	cont.	no flux	cont.	cont.	0
$c_{H_2, g}$	0	cont.	cont.	no flux	cont.	cont.	$c_{H_2, \text{inlet}}$
$c_{w, g}$	$c_{w, \text{inlet}}$	cont.	cont.	no flux	cont.	cont.	$c_{w, \text{inlet}}$
$c_{H_2O_2, g}$	0	cont.	cont.	no flux	cont.	cont.	0
$c_{HF, g}$	0	cont.	cont.	no flux	cont.	cont.	0
$c_{H_2, m}$	–	–	no flux	cont.	no flux	–	–
$c_{O_2, m}$	–	–	no flux	cont.	no flux	–	–
A	–	–	no flux	cont.	no flux	–	–
$c_{H_2O_2, m}$	–	–	no flux	cont.	no flux	–	–
$c_{HF, m}$	–	–	no flux	cont.	no flux	–	–
$c_{Fe^{II}, m}$	–	–	no flux	cont.	no flux	–	–
$c_{Fe^{III}, m}$	–	–	no flux	cont.	no flux	–	–
φ_s	no flux	cont.	cont.	–	cont.	cont.	0

For the ionomer species involved in the membrane degradation, the initial concentrations are shown in Equation (25):

$$c_{i,0} = \begin{cases} \rho_m / EW_0 & i = R_f SO_3 \\ 14 \rho_m / EW_0 & i = CF_2 \\ 0.2625 (\approx 15 \text{ppm}) & i = Fe^{II}, Fe^{III} \\ 0 & \text{all other ionomer species} \end{cases} \quad (25)$$

Results and Discussion

The transient in situ membrane degradation model developed in this work is a modified version of a 1D macroscopic MEA-based reaction-transport model, which was previously validated for chemical membrane degradation.¹⁴ The model's capability to simulate the evolution of ionomer molecular structure and physicochemical membrane properties was demonstrated, and the obtained results, for example, membrane thinning and total fluoride release, were in overall good agreement with experimental data.²⁸ Herein, the revised model was applied to simulate the role of iron ion transport and redox chemistry in membrane degradation. Due to the mobility of iron ions and high ionic conductivity of the membrane, ion migration is an important transport mode expected to depend on the cell voltage. In addition, the iron redox chemistry also depends on potential. The combined effects of iron ion reaction and transport on the membrane degradation were thus scrutinized in terms of the applied cell voltage. In addition, the sensitivity of the membrane degradation rates with respect to cell voltage was also simulated to provide insights on improving MEA durability.

Iron ion transport and reaction during membrane degradation

Open circuit voltage

A standard AST protocol for chemical membrane degradation was established by the US Department of Energy (DOE).¹⁵ In the protocol, open circuit voltage (OCV) operation is one of the stressors that can significantly promote chemical degradation.^{14,29} Although the dramatic degradation rates observed in this test have been tentatively attributed to the high gas crossover under OCV conditions,¹¹ the mechanisms involved have not been fully established. Herein, the in situ chemical degradation process under OCV is first examined in terms of the ferrous ion, ferric ion, and hydrogen peroxide concentrations involved in hydroxyl radical formation. These concentrations across the cathode CL, membrane, and anode CL are simulated and illustrated in Figure 4.

In hydrogen PEFCs, the Fe^{II} ion can be electrochemically generated from Fe^{III} through the ferric/ferrous redox reaction (in Table 3). The local potential at the anode CL, φ_s , is near zero, which is considerably lower than the redox potential for promoting the reduction of Fe^{III} to Fe^{II} , in which Fe^{III} gains an electron by oxidizing hydrogen. On the other hand, the Fe^{II} ion is expected to be electrochemically oxidized to Fe^{III} when exposed to high potentials at the cathode by donating an electron to the oxygen reduction. The simulated cathodic potential is around 1 V when the cell is held at OCV. The simulated value is lower than the standard electrode potential of the four-electron ORR due to hydrogen crossover but still positive of the Fe^{II}/Fe^{III} redox potential to promote the oxidation of Fe^{II} to Fe^{III} at the cathode CL. This situation gives rise to a Fe^{II}/Fe^{III} ion concentration gradient across the membrane. In the anode CL where Fe^{III} is reduced, a near-zero Fe^{III} concentration and

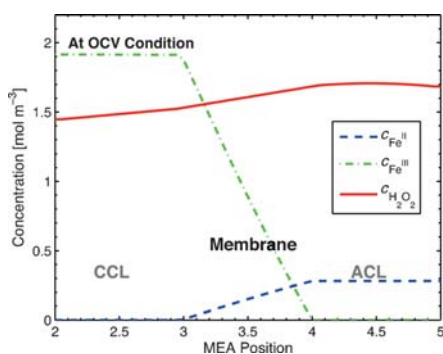


Figure 4. Simulated iron ions and hydrogen peroxide concentrations across the cathode CL ($2 < x < 3$), membrane ($3 < x < 4$), and anode CL ($4 < x < 5$) at $t = 0$ when the cell is held at OCV.

a high Fe^{II} concentration are obtained, as shown in Figure 4. In addition, Fe^{II} is oxidized in the cathode CL, resulting in a near-zero Fe^{II} concentration and a high Fe^{III} concentration. The presence of predominantly Fe^{III} in cathode CLs has been reported elsewhere.^[56]

When the cell is held at OCV, ion migration due to a potential gradient in the ionomer is negligible, and hence diffusion is the dominant mode of ion transport between anode and cathode CLs that drives Fe^{II} from anode to cathode and Fe^{III} from cathode to anode. The Fe^{II} ion is formed in the anode CL and diffuses into the membrane where it may react with H_2O_2 , $\cdot\text{OOH}$, and $\cdot\text{OH}$ along its path to the cathode. The calculated consumption rate of Fe^{II} in the membrane, that is, $\int_3^4 L_{m,0}(r_5 + r_7 + r_9)dx$, is, however, smaller than that in the cathode CL, as illustrated in Figure 5. This indicates that Fe^{II} is not fully reacted in the membrane and can reach the cathode CL for oxidation. Similarly, the Fe^{III} ion formed in the cathode CL diffuses into the membrane and onwards to the anode as indicated by the insignificant consumption rate in the membrane (Figure 5). Therefore, almost all Fe^{III} formed in the cathode CL reaches the anode CL where it is reduced back to Fe^{II} .

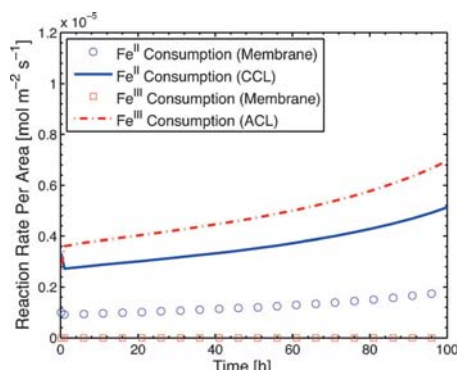


Figure 5. Simulated reaction rates of Fe^{II} and Fe^{III} in the MEA when the fuel cell is held at OCV.

As zero fluxes are assumed at the MPL and CL interfaces, a redox cycle of iron is formed in the MEA due to the conservation of species and charge. This demonstrates the decisive effect of the $\text{Fe}^{\text{II}}/\text{Fe}^{\text{III}}$ redox reaction on the distribution of $\text{Fe}^{\text{II}}/\text{Fe}^{\text{III}}$ in the MEA and the importance of including the $\text{Fe}^{\text{II}}/\text{Fe}^{\text{III}}$ redox chemistry, which was generally neglected in previous membrane degradation models.^[14,26–28] Moreover, the Fe^{III} ion has an oxidation number of +3, which is expected to have a stronger affinity to the sulfonic acid sites than the other iron ions with an oxidation number of +2, which gives rise to a lower mobility and diffusivity of Fe^{III} in the ionomer phase.^[41] This results in a higher concentration gradient for Fe^{III} than for Fe^{II} as well as a higher overall concentration (Figure 4).

In addition to the ferrous ion, hydrogen peroxide is also required for hydroxyl radical formation, and hence its concentration is also simulated and shown in Figure 4. The anodic potential is near zero, which is favorable for hydrogen peroxide formation through the two-electron ORR.^[45] Therefore, a higher H_2O_2 concentration in the membrane near the anode CL is obtained. With the higher concentrations of Fe^{II} and H_2O_2 , hydroxyl radicals are preferentially formed in the membrane near the anode CL, and hence the chemical degradation and associated reduction in sulfonic-acid-group concentration is faster near the anode CL (Figure 6).

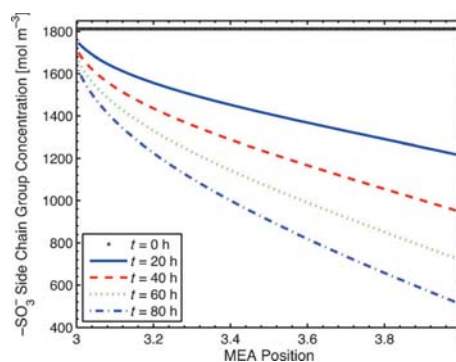


Figure 6. Simulated sulfonic-acid-group concentration in the cathode CL ($2 < x < 3$), membrane ($3 < x < 4$), and anode CL ($4 < x < 5$) as a function of degradation time at OCV.

0.9 V

When the cell voltage is held at 0.9 V, which is about 0.1 V lower than the simulated OCV at $t = 0$, an ionomer potential gradient across the cathode CL, membrane, and anode CL is formed due to regular electrochemical reactions in hydrogen PEFCs. As illustrated in Figure 7, the obtained ionomer potential decreases from the anode CL to the cathode CL, which results in migration of positively charged species (including protons, Fe^{II} ions, and Fe^{III} ions) from the anode CL to the cathode CL across the membrane. The Fe^{III} ion migration towards the cathode CL counteracts its diffusive transport and thereby results in a smaller Fe^{III} flux towards the anode CL. Hence, Fe^{III} is found to accumulate at the cathode CL, as illustrated in

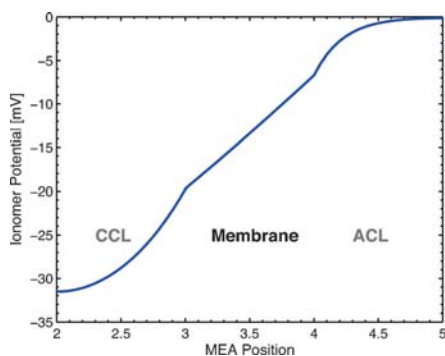


Figure 7. Simulated potential in the ionomer phase across the cathode CL ($2 < x < 3$), membrane ($3 < x < 4$), and anode CL ($4 < x < 5$) at $t=0$ when the cell voltage is held at 0.9 V.

Figure 8. Fe^{III} is the prevalent oxidation form of iron in the cathode CL because of the high cathode potential, which is positive of the standard $\text{Fe}^{\text{II}}/\text{Fe}^{\text{III}}$ redox potential. The smaller

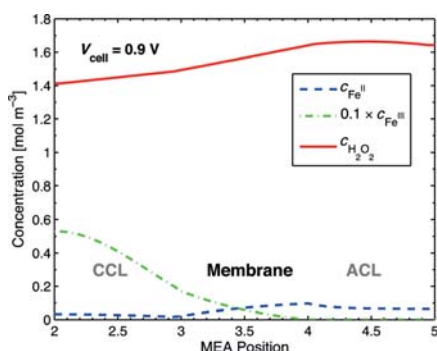


Figure 8. Simulated iron ions and hydrogen peroxide concentrations across the cathode CL ($2 < x < 3$), membrane ($3 < x < 4$), and anode CL ($4 < x < 5$) at $t=0$ when the cell voltage is held at 0.9 V.

Fe^{III} flux towards the anode CL also limits the iron ion reduction in the anode CL. Because the $\text{Fe}^{\text{II}}/\text{Fe}^{\text{III}}$ redox reaction is the dominant source of Fe^{II} in the MEA, this situation suppresses the Fe^{II} formation in the redox cycle of iron, which gives rise to a lower fraction of Fe^{II} in the membrane compared to the OCV condition. This analysis demonstrates the importance of considering ion migration during fuel cell operation at potentials below OCV.

Hydrogen peroxide is electrochemically generated at the anode CL, where the simulated overpotentials are similar between the cases when the cell is held at OCV and 0.9 V. Therefore, the obtained hydrogen peroxide concentrations in these two cases are comparable (Figures 4 and 8), which suggests that the impact of hydrogen peroxide on the chemical membrane degradation is constant in this voltage range and that the $\text{Fe}^{\text{II}}/\text{Fe}^{\text{III}}$ distribution in the MEA controls the overall degradation rate. With the lower Fe^{II} concentration in the membrane

at 0.9 V, 57% reduction in the chemical membrane degradation rate is determined in terms of the rates of sulfonic-acid-group concentration reduction, membrane thinning, and cumulative fluoride loss, as shown in Figure 9. The simulation demonstrates a strong relationship between the iron ion transport and chemical membrane degradation when the cell is held at high voltages.

0.7 V

As the cell voltage is further reduced to 0.7 V, representing a more practical fuel cell operating voltage, the ion migration becomes more dominant because the ionomer potential gradi-

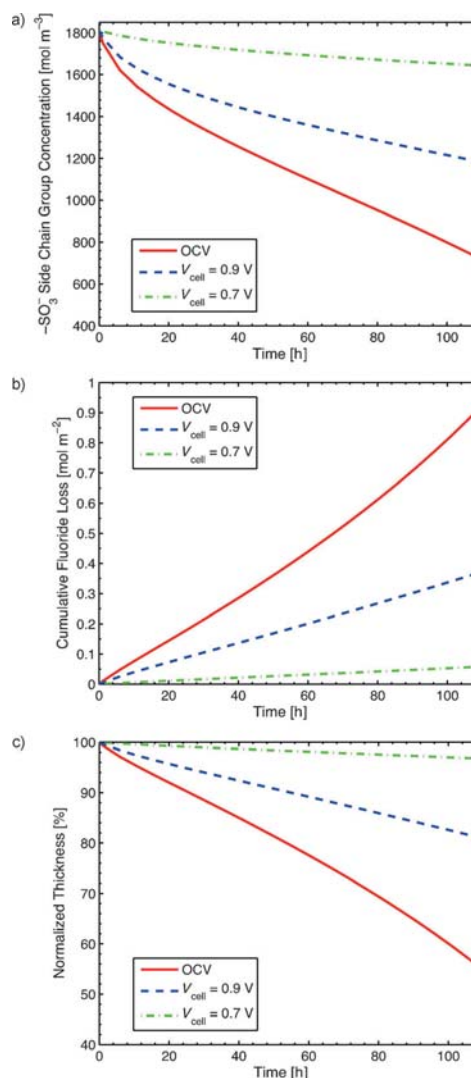


Figure 9. Simulated membrane degradation at OCV, $V_{\text{cell}}=0.9$ V, and $V_{\text{cell}}=0.7$ V. a) Average sulfonic-acid-group concentration. b) Average cumulative fluoride loss. c) Average membrane thinning.

ent increases to about 0.18 V due to the enhanced HOR and four-electron ORR. The Fe^{III} migration flux has a similar magnitude but opposite direction to its diffusion flux, resulting in a near-zero net Fe^{III} flux across the membrane. Without the Fe^{III} flux to the anode CL, the formation of Fe^{II} on this electrode cannot be sustained, which is demonstrated by the zero Fe^{II} concentration in the anode CL shown in Figure 10, even though a negative overpotential, $\varphi_s - \varphi_m - E_{12,\text{eq}}$, is calculated. In

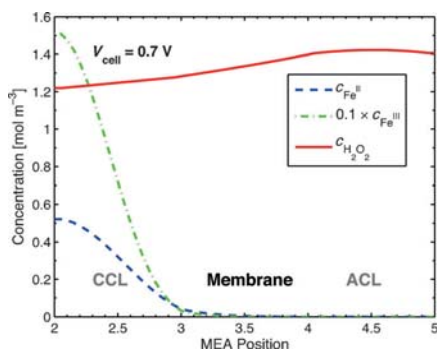


Figure 10. Simulated iron ions and hydrogen peroxide concentrations across the cathode CL ($2 < x < 3$), membrane ($3 < x < 4$), and anode CL ($4 < x < 5$) at $t=0$ when the cell voltage is held at 0.7 V.

this situation, the internal redox cycle of iron discovered at high cell potentials in the MEA is suppressed. In the cathode CL, an equilibrium between Fe^{II} and Fe^{III} is obtained as indicated by the near-zero simulated overpotential, $\varphi_s - \varphi_m - E_{12,\text{eq}}$; their concentrations are determined by the Nernst relation [Eq. (26)]:

$$\frac{C_{\text{Fe}^{\text{II}}}}{C_{\text{Fe}^{\text{III}}}} = \exp\left[\frac{F}{RT}(E_{12,\text{eq}} - 0.77)\right] \quad (26)$$

in which $E_{12,\text{eq}}$ obtained is around 0.86, resulting in a higher Fe^{II} concentration.

Due to the strong ion migration toward the cathode, the majority of the $\text{Fe}^{\text{II}}/\text{Fe}^{\text{III}}$ ions are accumulated in the cathode CL, which is illustrated by the concentration peak in Figure 10. This effect results in very low $\text{Fe}^{\text{II}}/\text{Fe}^{\text{III}}$ concentrations in the membrane and anode CL; for example, the average Fe^{II} ion concentration is now merely 0.01 mol m^{-3} in the membrane. Therefore, the membrane degradation is considerably less severe (Figure 9) when the cell is held at 0.7 V compared to the previous cases at OCV and 0.9 V even though there is still a sufficient supply of hydrogen peroxide from the anode CL, as indicated in Figure 10. Moreover, due to ion migration, the distribution of Fe^{II} is more asymmetric compared to H_2O_2 . This results in a higher chemical degradation rate near the cathode CL as indicated by the simulated sulfonic-acid-group concentration shown in Figure 11, which is opposite to the case at OCV (Figure 6). The non-uniform chemical degradation induced by the iron ion distribution is thus demonstrated to depend

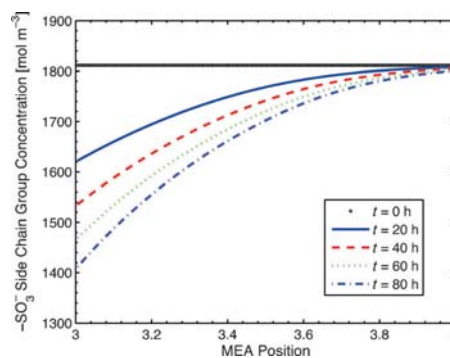


Figure 11. Simulated sulfonic-acid-group concentration across the membrane ($3 < x < 4$) as a function of degradation time at 0.7 V.

on the applied cell voltage and shift from the anode region to the cathode region as the cell voltage is reduced.

Cell voltage and membrane durability

The overall sensitivities of the hydrogen peroxide and ferrous ion concentrations to the applied cell voltage are evaluated and plotted in Figures 12 and 13, respectively. In the anode CL, the rate of two-electron ORR is related to the cell voltage and oxygen concentration. When the cell voltage is decreased from OCV, the four-electron ORR kinetics (in the cathode CL) increases because of its overpotential, which leads to a more negative ionomer potential and a smaller oxygen concentration at the anode CL–membrane interface. The hydrogen peroxide formation through two-electron ORR is, therefore, decreased. However, the overall effect of the cell voltage on the two-electron ORR rate is limited and a moderate decrease in hydrogen peroxide formation is observed (Figure 13). In contrast, the Fe^{II} concentration in the membrane has an exponential dependence on the cell voltage as shown in Figure 12. There is a dramatic decrease (−93%) in Fe^{II} ion concentration when the cell voltage is decreased from OCV to 0.7 V, which is a consequence of the increased ion migration flux as identified previously.

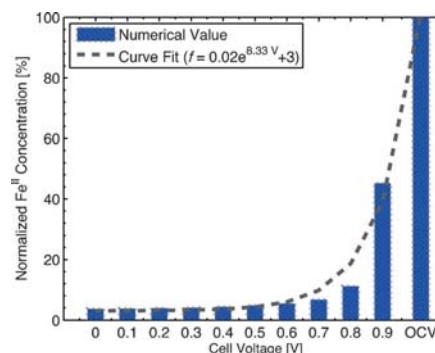


Figure 12. Simulated average Fe^{II} concentration in the membrane as a function of cell voltage at $t=0$.

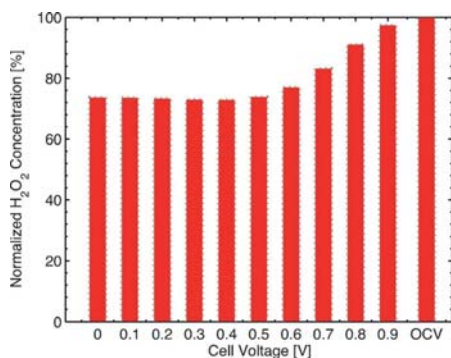


Figure 13. Simulated average hydrogen peroxide concentration in the membrane as a function of cell voltage at $t=0$.

When the cell voltage is below 0.7 V, the concentration is further decreased to less than 5% of the value at OCV due to the iron ion accumulation in the cathode CL. These results demonstrate that the cell voltage has a much stronger effect on Fe^{II} concentration than on hydrogen peroxide concentration in the membrane.

According to Reaction 5 in Table 3, the hydroxyl radical formation rate in the membrane is proportional to the product of the Fe^{II} and hydrogen peroxide concentrations. The overall chemical membrane degradation rate is thus a function of the same concentrations. The degradation rate can be quantitatively represented by the reduction of sulfonic-acid-group concentration in the membrane, thickness reduction, and cumulative fluoride loss, which are evaluated and shown in Figure 14. At the highest levels of both Fe^{II} and hydrogen peroxide concentrations the membrane experiences the most severe degradation when the cell voltage is held at OCV. This result provides fundamental evidence for the empirical rationale of using OCV conditions to accelerate the chemical membrane degradation in various ASTs.^[4,29,55] As expected from the concentration analysis, the degradation rate exhibits an exponential decay that is similar in nature to the underlying exponen-

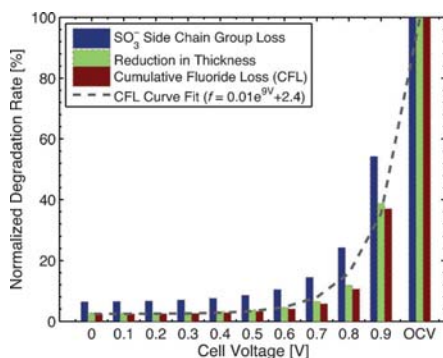


Figure 14. Simulated degradation rates in terms of normalized sulfonic-acid-group concentration loss, reduction in thickness, and cumulative fluoride loss in the membrane as a function of cell voltage.

tial decay in Fe^{II} concentration, although the decay rate is further compounded by the moderate reduction in hydrogen peroxide concentration. When the cell voltage is decreased from OCV to 0.7 V, the membrane transitions from a severe to a modest degradation state (tenfold reduction in fluoride loss at 0.7 V), which is chiefly attributed to the critical reduction in the Fe^{II} presence in the membrane. This finding is consistent with and provides a theoretical understanding of the exponential dependence between degradation rate and current density observed experimentally during in situ testing.^[29] As the cell voltage is further decreased to below 0.7 V, the simulated degradation rate is essentially negligible because there is insignificant Fe^{II} in the membrane to catalyze the formation of hydroxyl radicals.

In PEFCs, iron contamination is common and cannot be effectively eliminated because it can be introduced through MEA/system materials,^[24] be present in fuel and oxidant, and has a high affinity to the sulfonic-acid groups in the membrane.^[41] Moreover, hydrogen peroxide formation through two-electron ORR, an intermediate step of ORR, is always possible in PEFCs.^[57] Fortunately, the dependence of the Fe^I/Fe^{III} ion distribution on the cell voltage suggests that the concentration of harmful Fe^{II} can be minimized by operating PEFCs at intermediate cell voltages (i.e., voltages below 0.7 V predicted in the model), which are commonly applied in automotive applications. Without this active catalyst, the hydroxyl radical formation through Reaction 5 in Table 3 is substantially reduced even though hydrogen peroxide is formed and present in the cell, and thus the membrane durability is significantly enhanced as the main chemical membrane degradation mechanism is suppressed. The underlying ion migration in PEFCs is expected to have similar effects on the distribution of other cations, which may also catalyze the hydroxyl radical formation. Therefore, the mitigation strategy suggested here is expected to be generally applicable for PEFC operation.

Conclusions

Interrelated effects of iron ion transport and redox chemistry on the chemical membrane degradation in polymer electrolyte fuel cells (PEFCs) are established using a comprehensive, transient in situ membrane degradation model. The state and distribution of mobile and reactive iron ions inside the PEFC are found to be highly sensitive to the applied cell voltage and shown to play a key role in the overall degradation process. When the cell is held at open circuit voltage, an iron ion redox cycle is generated in the membrane electrolyte assembly to preserve a relatively high Fe^{II} concentration in the membrane, which leads to the most severe chemical membrane degradation through the Fenton mechanism. As the cell voltage is reduced, ion migration dramatically weakens the iron ion redox cycle. The iron ion reduction is suppressed in the anode catalyst layer, and most of the iron ions are accumulated in the cathode catalyst layer where an equilibrium between the Fe^I/Fe^{III} concentrations is attained. The Fe^{II} concentration in the membrane is thereby shown to decay exponentially as the cell voltage is reduced. Without this active metal-ion catalyst, the

harmful hydroxyl radical formation is greatly suppressed, which elucidates the mitigating effect of reduced cell voltage on the chemical membrane degradation. The simulated tenfold reduction in the cumulative fluoride release suggests that intermediate cell voltage operation provides a practical mitigation strategy for chemical membrane degradation through iron ion contamination and hydrogen peroxide formation, which are common and cannot be effectively eliminated in PEFCs.

Acknowledgements

This research was supported by Ballard Power Systems and the Natural Sciences and Engineering Research Council of Canada through an Automotive Partnership Canada (APC) grant. The authors wish to thank their colleagues at SFU FCReL and Ballard for providing valuable comments and advices.

Keywords: durability · fuel cells · iron · membranes · modeling

- [1] M. P. Rodgers, L. J. Bonville, H. R. Kunz, D. K. Slattery, J. M. Fenton, *Chem. Rev.* **2012**, *112*, 6075–6103.
- [2] C. S. Gittleman, F. D. Coms, Y.-H. Lai in *Polymer Electrolyte Fuel Cell Degradation* (Eds.: M. Mench, E. C. Kumbur, T. N. Veziroglu), Academic Press, Boston **2012**, pp. 15–88.
- [3] X. Huang, R. Solasi, Y. Zou, M. Feshler, K. Reifsnider, D. Condit, S. Burlatsky, T. Madden, *J. Polym. Sci. Part B* **2006**, *44*, 2346–2357.
- [4] C. Lim, L. Ghassemzadeh, F. V. Hove, M. Lauritzen, J. Kolodziej, G. Wang, S. Holdcroft, E. Kjeang, *J. Power Sources* **2014**, *257*, 102–110.
- [5] M.-A. Goulet, R. M. Khorasany, C. D. Torres, M. Lauritzen, E. Kjeang, G. G. Wang, N. Rajapakse, *J. Power Sources* **2013**, *234*, 38–47.
- [6] R. M. Khorasany, M.-A. Goulet, A. S. Alavijeh, E. Kjeang, G. G. Wang, R. Rajapakse, *J. Power Sources* **2014**, *252*, 176–188.
- [7] A. S. Alavijeh, M.-A. Goulet, R. M. Khorasany, J. Ghataurah, C. Lim, M. Lauritzen, E. Kjeang, G. G. Wang, R. Rajapakse, *Fuel Cells* **2015**, DOI: 10.1002/fuce.201400040.
- [8] R. M. Khorasany, A. S. Alavijeh, E. Kjeang, G. G. Wang, R. Rajapakse, *J. Power Sources* **2015**, *274*, 1208–1216.
- [9] R. M. Khorasany, E. Kjeang, G. G. Wang, R. Rajapakse, *J. Power Sources* **2015**, *279*, 55–63.
- [10] N. Macauley, A. S. Alavijeh, M. Watson, J. Kolodziej, S. Knights, G. G. Wang, E. Kjeang, *J. Electrochem. Soc.* **2015**, *162*, F98–F107.
- [11] E. Endoh, S. Terazono, H. Widjaja, Y. Takimoto, *Electrochem. Solid-State Lett.* **2004**, *7*, A209–A211.
- [12] J. Healy, C. Hayden, T. Xie, K. Olson, R. Waldo, M. Brundage, H. Gasteiger, J. Abbott, *Fuel Cells* **2005**, *5*, 302–308.
- [13] L. Ghassemzadeh, K.-D. Kreuer, J. Maier, K. Müller, *J. Phys. Chem. C* **2010**, *114*, 14635–14645.
- [14] L. Gubler, S. M. Dockheer, W. H. Koppenol, *J. Electrochem. Soc.* **2011**, *158*, B755–B769.
- [15] L. Ghassemzadeh, S. Holdcroft, *J. Am. Chem. Soc.* **2013**, *135*, 8181–8184.
- [16] M. Danilczuk, F. D. Coms, S. Schlick, *J. Phys. Chem. B* **2009**, *113*, 8031–8042.
- [17] M. Spulber, S. Schlick, *J. Phys. Chem. B* **2011**, *115*, 12415–12421.
- [18] Y. Nosaka, K. Ohtaka, N. Ohguri, A. Y. Nosaka, *J. Electrochem. Soc.* **2011**, *158*, B430–B433.
- [19] A. B. LaConti, M. Hamdan, R. C. McDonald, *Mechanisms of membrane degradation. Handbook of Fuel Cells*, Wiley, **2003**.
- [20] M. Inaba, T. Kinumoto, M. Kiriake, R. Umebayashi, A. Tasaka, Z. Ogumi, *Electrochim. Acta* **2006**, *51*, 5746–5753.
- [21] A. LaConti, H. Liu, C. Mittelsteadt, R. McDonald, *ECS Trans.* **2006**, *1*, 199–219.
- [22] M. Aoki, H. Uchida, M. Watanabe, *Electrochem. Commun.* **2006**, *8*, 1509–1513.
- [23] C. Chen, G. Levitin, D. W. Hess, T. F. Fuller, *J. Power Sources* **2007**, *169*, 288–295.
- [24] A. Pozio, R. Silva, M. D. Francesco, L. Giorgi, *Electrochim. Acta* **2003**, *48*, 1543–1549.
- [25] B. Beverskog, I. Puigdomenech, *Corros. Sci.* **1996**, *38*, 2121–2135.
- [26] A. A. Shah, T. R. Ralph, F. C. Walsh, *J. Electrochem. Soc.* **2009**, *156*, B465–B484.
- [27] R. Coulon, W. Bessler, A. A. Franco, *ECS Trans.* **2010**, *25*, 259–273.
- [28] K. H. Wong, E. Kjeang, *J. Electrochem. Soc.* **2014**, *161*, F823–F832.
- [29] W. Liu, M. Crum, *ECS Trans.* **2006**, *3*, 531–540.
- [30] C. Chan, N. Zamel, X. Li, J. Shen, *Electrochim. Acta* **2012**, *65*, 13–21.
- [31] J. Shen, J. Zhou, N. G. C. Astrath, T. Navessin, Z.-S. Liu, C. Lei, J. H. Rohling, D. Bessarabov, S. Knights, S. Ye, *J. Power Sources* **2011**, *196*, 674–678.
- [32] H. Wu, P. Berg, X. Li, *J. Electrochem. Soc.* **2010**, *157*, B1–B12.
- [33] E. N. Fuller, P. D. Schettler, J. C. Giddings, *Ind. Eng. Chem.* **1966**, *58*, 18–27.
- [34] S. Ge, X. Li, B. Yi, I.-M. Hsing, *J. Electrochem. Soc.* **2005**, *152*, A1149–A1157.
- [35] V. A. Sethuraman, J. W. Weidner, A. T. Haug, L. V. Protsailo, *J. Electrochem. Soc.* **2008**, *155*, B119–B124.
- [36] D. E. Curtin, R. D. Lousenberg, T. J. Henry, P. C. Tangeman, M. E. Tisack, *J. Power Sources* **2004**, *131*, 41–48.
- [37] C. Zhou, M. A. Guerra, Z.-M. Qiu, T. A. Zawodzinski, D. A. Schiraldi, *Macromolecules* **2007**, *40*, 8695–8707.
- [38] T. Xie, C. A. Hayden, *Polymer* **2007**, *48*, 5497–5506.
- [39] A. Z. Weber, C. Delacourt, *Fuel Cells* **2008**, *8*, 459–465.
- [40] M. F. Serincan, U. Pasaogullari, T. Molter, *Int. J. Hydrogen Energy* **2010**, *35*, 5539–5551.
- [41] T. Okada, Y. Ayato, M. Yuasa, I. Sekine, *J. Phys. Chem. B* **1999**, *103*, 3315–3322.
- [42] D. You, H. Zhang, J. Chen, *Electrochim. Acta* **2009**, *54*, 6827–6836.
- [43] A. Shah, M. Watt-Smith, F. Walsh, *Electrochim. Acta* **2008**, *53*, 8087–8100.
- [44] C. Chen, T. F. Fuller, *Electrochim. Acta* **2009**, *54*, 3984–3995.
- [45] V. A. Sethuraman, J. W. Weidner, A. T. Haug, S. Motupally, L. V. Protsailo, *J. Electrochem. Soc.* **2008**, *155*, B50–B57.
- [46] A. M. Dreizler, E. Roduner, *Fuel Cells* **2012**, *12*, 132–140.
- [47] Z. Tayarani-Yoosefabad, D. Harvey, J. Bellerive, E. Kjeang, unpublished results.
- [48] A. Nanjundappa, A. S. Alavijeh, M. E. Hannach, D. Harvey, E. Kjeang, *Electrochim. Acta* **2013**, *110*, 349–357.
- [49] T. Yanaka, in *Fluoride Research 1985 Selected Papers from the 14th Conference of the International Society for Fluoride Research, Vol. 27* (Eds.: H. Tsunoda, M.-H. Yu), Elsevier, **1986**, pp. 81–88.
- [50] R. L. McMurtrie, F. G. Keyes, *J. Am. Chem. Soc.* **1948**, *70*, 3755–3758.
- [51] D. M. Bernardi, M. W. Verbrugge, *J. Electrochem. Soc.* **1992**, *139*, 2477–2491.
- [52] C. Siegel, *Energy* **2008**, *33*, 1331–1352.
- [53] J. Fimrite, B. Carnes, H. Struchtrup, N. Djilali, *J. Electrochem. Soc.* **2005**, *152*, A1815–A1823.
- [54] B. Carnes, N. Djilali, *Electrochim. Acta* **2006**, *52*, 1038–1052.
- [55] N. Garland, T. Benjamin, J. Kopasz, *ECS Trans.* **2007**, *11*, 923–931.
- [56] N. Ohguri, A. Y. Nosaka, Y. Nosaka, *Electrochem. Solid-State Lett.* **2009**, *12*, B94–B96.
- [57] I. Katsounaros, W. B. Schneider, J. C. Meier, U. Benedikt, P. U. Biedermann, A. Cuesta, A. A. Auer, K. J. J. Mayrhofer, *Phys. Chem. Chem. Phys.* **2013**, *15*, 8058–8068.

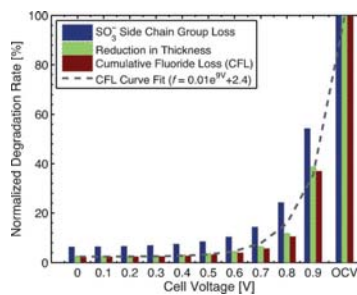
Received: September 5, 2014
Published online on ■■■ 0000

FULL PAPERS

K. H. Wong, E. Kjeang*



Mitigation of Chemical Membrane Degradation in Fuel Cells: Understanding the Effect of Cell Voltage and Iron Ion Redox Cycle



Membrane stability controlled by iron ion dynamics: An essential, yet previously missing link in the fundamental understanding of chemical membrane degradation in polymer electrolyte fuel cells is presented. An iron ion redox cycle is discovered within the membrane and catalyst layers during fuel cell operation. This redox cycle is shown to be the underlying mechanism for the cell potential dependency of the chemical degradation of the membrane, which can be mitigated by operation at intermediate cell voltages.

CONFIDENTIAL

Appendix C: In situ modeling of chemical membrane degradation and mitigation in ceria-supported fuel cells

In situ modeling of chemical membrane degradation and mitigation in ceria-supported fuel cells

Ka Hung Wong^a, Erik Kjeang^{a,*}

^a*School of Mechatronic Systems Engineering, Simon Fraser University, 250-13450 102 Avenue, Surrey, BC V3T 0A3*

Abstract

Ceria-supported membrane electrode assemblies (MEAs) have recently been proposed to address chemical membrane degradation in polymer electrolyte fuel cells. Although ceria is known to effectively protect the membrane at open circuit voltage (OCV) conditions, its effectiveness has not been demonstrated for cell voltages below OCV and associated conditions relevant for field operation. In the present work, a comprehensive, transient *in situ* chemical degradation model for ceria stabilized MEAs is developed and applied to investigate the mitigation effectiveness of ceria additive. At high cell voltages, abundant Ce^{3+} ions are available in the membrane to quench hydroxyl radicals which is the primary mitigation mechanism observed at OCV conditions. However, the mitigation is suppressed at low cell voltages, where electromigration drives Ce^{3+} ions into the cathode catalyst layer (CL). Without an adequate amount of Ce^{3+} in the membrane, the hydroxyl radical scavenging is significantly reduced, leading to a ten-fold reduction in mitigation

*Corresponding author. Tel: +1 (778) 782-8791; Fax: +1 (778) 782-7514
Email address: ekjeang@sfu.ca (Erik Kjeang)

effectiveness at cell voltages below 0.7 V. The simulated results also suggest that significant ceria precipitation may occur in the cathode CL due to the increased local Ce^{3+} concentration at low to medium cell voltages. Ceria-supported MEAs may therefore experience higher rates of chemical membrane degradation at low cell voltages than at OCV.

Keywords: fuel cell, durability, mitigation, cerium oxide, degradation, modeling

1. Introduction

Hydrogen powered polymer electrolyte fuel cells (PEFCs) generally use perfluorosulfonic acid (PFSA) ionomer membranes to separate the two electrodes in the membrane electrode assembly (MEA). Their high proton conductivity at low temperatures, relatively low reactant permeation, and superior electrical insulation lead to high fuel cell performance. However, the ionomer membrane can be degraded in the fuel cell environment which reduces its stability and limits its lifetime [1, 2]. Chemical degradation initiates the overall degradation processes [3, 4] and further damages the membrane when combined with mechanical stress, strain, and fatigue induced by hydrothermal fluctuations in the MEA [5, 6, 7, 8, 9]. The resulting physical damage in the forms of cracks and holes eventually causes hydrogen leaks across the membrane which is considered one of the main lifetime limiting failure modes in fuel cells [4, 10].

The primary chemical degradation in PEFCs is caused by reactions of

reactive radicals with the PFSA ionomer membrane [11, 12, 13, 14, 15]. For instance, hydrogen peroxide (H_2O_2) can be generated via the two-electron oxygen reduction reaction (ORR) resulting in hydroxyl radical ($\cdot\text{OH}$) formation due to decomposition of hydrogen peroxide in the presence of metal contaminants [16, 17]. The hydroxyl radical formed is highly reactive and can attack the ionomer membrane in terms of side chain cleavage and unzipping [12, 14, 15, 18, 19] which is responsible for the deteriorated physicochemical properties observed in degraded membranes. Radical scavenging is therefore proposed to mitigate the chemical damage by quenching the radicals before they attack the ionomer membrane. One of the most promising additives to quench $\cdot\text{OH}$ in fuel cells is ceria (CeO_2), which can effectively protect the ionomer membrane under open circuit voltage (OCV) accelerated stress test (AST) or *ex-situ* Fenton's durability conditions [20, 21, 22, 23, 24, 25, 26, 27].

When ceria (cerium oxide) is incorporated in the MEA, it dissolves and forms a $\text{Ce}^{3+}/\text{Ce}^{4+}$ redox couple in the ionomer phase according to the Pourbaix diagram for cerium [28]. The multivalent nature of the redox couple allows the cerium ions to alternate between the two oxidation states: Ce^{3+} and Ce^{4+} . The Ce^{3+} ion can react with $\cdot\text{OH}$ and oxidize to the Ce^{4+} ion, while the Ce^{4+} ion can be reduced to the Ce^{3+} ion by reacting with hydrogen peroxide. This Ce^{3+} regeneration is considered to be essential for the sustainable mitigation of chemical membrane degradation observed during AST conditions [20, 22, 24, 25, 26, 27]. However, this hypothesis is difficult to confirm experimentally. The distribution, transport, and formation/consumption of cerium

ions within a fuel cell would be very challenging to measure quantitatively within an operating fuel cell. For instance, while the ratio of $\text{Ce}^{3+} : \text{Ce}^{4+}$ has been measured in H_2SO_4 solution, it cannot represent the true ratio inside a fuel cell [29]. The experimental challenges and limitations of *in situ* measurements raises the importance of developing reliable fundamental models in order to analyze the mitigation processes under realistic conditions and complement the experimental findings.

Modeling of the cerium ion mitigation processes was recently pioneered by Gubler *et al.* by means of an *ex situ* kinetic simulation [30]. The model examined the chemical reaction rates between the $\text{Ce}^{3+}/\text{Ce}^{4+}$ redox couple and radicals in the membrane and concluded that the mitigation effect is based on the rapid $\cdot\text{OH}$ quenching facilitated by Ce^{3+} . However, no *in situ* models that describe this phenomenon have been published to date. The overall objective of the present work is therefore to develop and validate a comprehensive, transient *in situ* membrane model that describes the complete set of chemical/electrochemical reactions and transport phenomena of relevance for ceria induced mitigation of chemical degradation. The proposed model considers the reaction-transport phenomena of H_2O_2 and other dissolved species in the ionomer (*e.g.*, dissolved hydrogen and oxygen) which are expected to be important in simulating the membrane $\cdot\text{OH}$ concentration. For this reason, a full MEA based numerical framework [18, 19] is adopted, which has been used previously to describe the *in situ* chemical degradation process in regular, non-supported membrane during realistic fuel cell

operating conditions, and applied here for ceria-supported MEAs.

2. Model Formulation and Governing Equations

The present modeling framework primarily targets the chemical stabilization of PFSA ionomer membranes achieved in ceria-supported MEAs. The influences of the $\text{Ce}^{3+}/\text{Ce}^{4+}$ redox system on chemical degradation by hydroxyl radical ($\cdot\text{OH}$) attack are analyzed in terms of the reaction-transport phenomena of the $\text{Ce}^{3+}/\text{Ce}^{4+}$ couple in the MEA. The baseline chemical degradation algorithms developed and validated in our previous work [18, 19] are modified and applied for this purpose. The algorithms provide a comprehensive description of the *in situ* molecular degradation of PFSA ionomer membranes and the role of Fenton's reagent (iron ion and hydrogen peroxide) in the degradation process. The details of the governing equations used in modeling the molecular degradation and the transport phenomena of the gas phase species (hydrogen, oxygen, water vapor, hydrogen peroxide and hydrogen fluoride), ionomer phase species (dissolved water, hydrogen peroxide, hydrogen fluoride, $\cdot\text{OH}$, hydrogen radical, hydroperoxyl radical, Fe^{2+} , and Fe^{3+}), and electrons are described in our previous publications [18, 19]. In the present work, we emphasize the reaction-transport phenomena of $\text{Ce}^{3+}/\text{Ce}^{4+}$ and their influences on the chemical membrane degradation.

The governing equation used in the model is based on the reaction-transport formulation generally applied in PEFC modeling for conservation

of species [18, 19]:

$$\frac{\partial}{\partial t} (\varepsilon c_i) + \nabla \cdot J_i = S_i, \quad (1)$$

where c_i , J_i , and S_i represent the concentration, flux, and source of species i in the given phase, respectively, and ε denotes the volume fraction of the given phase. It describes the conservation laws in a one-dimensional computational domain comprising of a standard MEA shown in Fig. 1. The MEA domain features a membrane flanked by catalyst layers (CLs) and gas diffusion layers (GDLs) with separate macroporous substrate and micro-porous layer (MPL) subdomains. The x -axis represents the through-plane direction and starts at the cathode gas channel (GC) and GDL interface ($x = 0$). All MEA layers are normalized by thickness, and the MEA dimensions and physical parameters used in the model are listed in Table 1. Three distinct phases are considered in the model: the gas phase and solid phase in GDLs and CLs, and the ionomer phase in CLs and membrane. The various species and transport phenomena in all MEA layers are also indicated in the schematic.

2.1. Reaction-Transport Phenomena of $\text{Ce}^{3+}/\text{Ce}^{4+}$

Cerium ions ($\text{Ce}^{3+}/\text{Ce}^{4+}$) are considered as charged species dissolved in the ionomer phase with fluxes governed by the Nernst-Planck equation [34, 35]:

$$J_i = -D_i \nabla c_i - u_i z_i c_i F \nabla \phi_e, \quad (2)$$

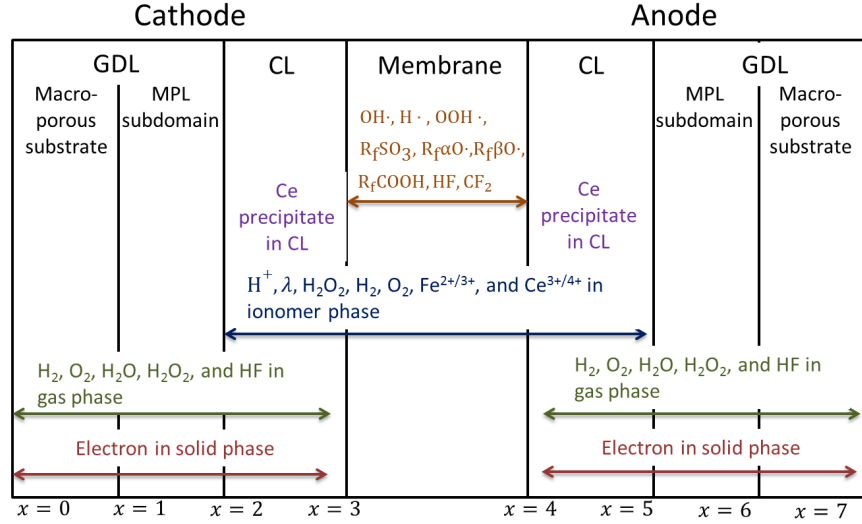


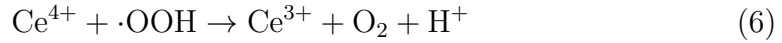
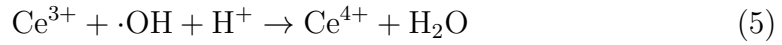
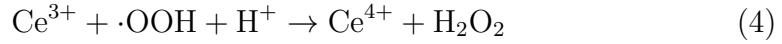
Figure 1: Schematic of the computational domain, including membrane, catalyst layers (CLs), and gas diffusion layers (GDLs; consisting of a macroporous substrate and a microporous layer). Chemical degradation is considered in the membrane. Gas and electron transport is considered in the GDLs and CLs, and transport in the ionomer phase is considered in the CLs and membrane. Cerium precipitate is considered in the pores of the CLs.

Table 1: Structural and physical parameters used in the model.

Parameter	Symbol	Value (Unit)
Thickness of:		
GDL macroporous substrate	L_{GDL}	250 (μm)
MPL subdomain	L_{MPL}	25 (μm)
CL	L_{CL}	15 (μm)
BOL Membrane	$L_{\text{m},0}$	30 (μm)
Porosity of:		
GDL macroporous substrate	ε_{GDL}	0.78 [31]
MPL subdomain	ε_{MPL}	0.65 [31]
CL	ε_{CL}	0.4 [32]
Ionomer fraction in CLs	ε_{e}	0.3 [33]
Faraday's constant	F	96485 (C mol^{-1})
Gas constant	R	8.314 ($\text{J K}^{-1} \text{mol}^{-1}$)

where the first term represents diffusion due to the concentration gradient and the second term represents migration due to the ionomer potential gradient, ϕ_e . In Eq. (2), z_i denotes the charge number of species i , and the self-diffusivity, D_i , and mobility, u_i , of species i are related by the Nernst-Einstein relation, $D_i = u_i RT$. The ionic mobility of Ce^{3+} and Ce^{4+} is assumed to be 10^{-14} and 10^{-15} s mol kg^{-1} , respectively. Convective ion transport due to water crossover is neglected.

The chemical and electrochemical reactions of the $\text{Ce}^{3+}/\text{Ce}^{4+}$ redox couple considered in the model are:



Reaction 3 shows the reaction between cerium ion and hydrogen peroxide. Reactions 4 to 6 are the reactions between cerium ions and radical species formed in the ionomer membrane. The kinetics of reactions 3 to 6 are given

by:

$$r_1 = k_1 \theta c_{\text{Ce}^{4+}} c_{\text{H}_2\text{O}_2} \quad (8)$$

$$r_2 = k_2 \theta c_{\text{Ce}^{3+}} c_{\text{O}\cdot\text{OH}} \quad (9)$$

$$r_3 = k_3 \theta c_{\text{Ce}^{3+}} c_{\cdot\text{OH}} \quad (10)$$

$$r_4 = k_4 \theta c_{\text{Ce}^{4+}} c_{\text{O}\cdot\text{OH}}, \quad (11)$$

where θ accounts for the impact of membrane swelling on the concentration of dissolved ionomer species [19, 36]. Reaction 7 presents the electrochemical reaction for the $\text{Ce}^{3+}/\text{Ce}^{4+}$ redox system at the CLs. In hydrogen PEFCs, the operating conditions favor cerium ion reduction because of its high electrochemical potential (1.44 V). The kinetics of this reaction are described by the Butler-Volmer equation [37, 38]:

$$r_5 = ai_{5,0} F \sqrt{c_{\text{Ce}^{3+}} c_{\text{Ce}^{4+}}} \left[\exp\left(\frac{F\eta_5}{2RT}\right) - \exp\left(\frac{-F\eta_5}{2RT}\right) \right]. \quad (12)$$

Details of parameters and variables used in calculating the chemical kinetics are listed in Table 2.

Cerium migration within the MEA was previously observed experimentally in the literature [27, 39]. Lim *et al.* [27] determined the distribution of cerium in ceria-supported MEAs by neutron activation analysis (NAA). The measured results indicated that cerium can migrate from the CLs into the membrane, which resulted in a higher cerium concentration in the membrane.

Table 2: Parameters associated with calculation of reaction kinetics

Parameter	Value (Unit)
Local overpotential, η_i	$\phi_s - \phi_e - E_{i,eq}$ (V)
Volumetric specific surface area, a	10^4 (m ⁻¹)
Effect of membrane swelling, θ	$\frac{14(V_{m,0} + \lambda V_w)}{\lambda(V_{m,0} + 14V_w)}$
Exchange current density of reaction 7, $i_{5,0}$	1 (A m ⁻²)
Reaction rate of [30]:	
reaction 3, k_1	$10^3 \exp\left(\frac{58000}{R} \left(\frac{1}{298} - \frac{1}{T}\right)\right)$ (mol ⁻¹ s ⁻¹)
reaction 4, k_2	$2.1 \times 10^2 \exp\left(\frac{58000}{R} \left(\frac{1}{298} - \frac{1}{T}\right)\right)$ (mol ⁻¹ s ⁻¹)
reaction 5, k_3	$3 \times 10^5 \exp\left(\frac{58000}{R} \left(\frac{1}{298} - \frac{1}{T}\right)\right)$ (mol ⁻¹ s ⁻¹)
reaction 6, k_4	$2.7 \times 10^3 \exp\left(\frac{58000}{R} \left(\frac{1}{298} - \frac{1}{T}\right)\right)$ (mol ⁻¹ s ⁻¹)
Nernst potential for reaction 7, $E_{7,eq}$	$1.44 + \ln(c_{Ce^{4+}}/c_{Ce^{3+}})$ (V)
Rate of precipitation, $k_{Ce,p}$	2×10^{-7} s ⁻¹
Rate of dissolution, $k_{Ce,d}$	2×10^{-6} s ⁻¹

Stewart *et al.* [39] used X-ray fluorescence (XRF) spectroscopy to determine the cerium profile across the MEA. Their results also suggested that cerium can migrate across the membrane. However, the cerium was finally accumulated in the anode and cathode CLs, with only a marginal amount of cerium remaining in the membrane. The inconsistent experimental findings may potentially be attributed to the different ceria loadings with the intermetallic interaction between cerium and platinum [39, 40]. The cerium loading used by Stewart *et al.*, $6.92 \mu\text{g cm}^{-2}$, is approximately 7x lower than that used by Lim *et al.* experiment. At this small amount of cerium loading, the intermetallic interaction may dominant the cerium transport in the catalyst layers, which leads a higher concentration in the catalyst layers. On the other hand, the high cerium loading used by Lim *et al.* [27] provides plenty of mobile cerium ions even though a certain portion of the

cerium ions becomes immobile due to the intermetallic interaction. Besides the intermetallic interaction, ceria is believed to be immobile due to other mechanism. Ceria is believed to dissolve in the ionomer phase because of its acidic environment. Depending on the cerium ion concentration and solubility in the ionomer these ions may exchange existing cations and thereby reduce the local proton concentration and acidity of the ionomer. According to the Pourbaix diagram for cerium [28], the level of ceria dissolution decreases with increasing pH and ceria precipitation is possible when the environment is not sufficiently acidic. Therefore, the reduction in proton concentration due to cerium ion exchange on the sulfonic acid end group could favor for ceria precipitation in which cerium ion is precipitated, *i.e.*, $2\text{Ce}^{3+} + 6\text{H}_2\text{O} \rightarrow 2\text{Ce}(\text{OH})_3 + 6\text{H}^+ \rightarrow \text{Ce}_2\text{O}_3 + 3\text{H}_2\text{O} + 6\text{H}^+$, and cerium(III) oxide can further be hydrolyzed to ceria. In the present model, the effect due to intermetallic interaction is neglected, and ceria precipitation is modeled and described as a phase change phenomenon with the rate calculated as:

$$r_{\text{Ce,ms}} = k_{\text{Ce,p}}c_{\text{Ce}^{3+/4+}} (c_{\text{Ce}^{3+/4+}} - c_{\text{Ce,sat}}) q - k_{\text{Ce,d}}c_{\text{CeO}_2} (c_{\text{Ce}^{3+/4+}} - c_{\text{Ce,sat}}) (1 - q), \quad (13)$$

where this formulation is an analogue of condensation and evaporation in two-phase flow [41]. In Eq. (13), $k_{\text{Ce,p}}$ and $k_{\text{Ce,d}}$ represent the rate of precipitation

Table 3: Summary of the source terms considered in the governing equations

	CLs	Membrane
$S_{\text{Ce}^{3+}}$	$r_3 - r_4 - r_5 + r_6 - r_7 - r_{\text{Ce}^{3+},\text{ms}}$	$r_3 - r_4 - r_5 + r_6$
$S_{\text{Ce}^{4+}}$	$-r_3 + r_4 + r_5 - r_6 + r_7 - r_{\text{Ce}^{4+},\text{ms}}$	$-r_3 + r_4 + r_5 - r_6$
S_{CeO_2}	$r_{\text{Ce}^{3+},\text{ms}} + r_{\text{Ce}^{4+},\text{ms}}$	-

and dissolution, respectively. The switching function, q , is defined as:

$$q = \frac{1 + |c_{\text{Ce}^{3+/4+}} - c_{\text{Ce,sat}}|}{2} (c_{\text{Ce}^{3+/4+}} - c_{\text{Ce,sat}}), \quad (14)$$

such that it is one when the cerium ion concentration is greater than the cerium ion saturation concentration, $c_{\text{Ce,sat}}$, and otherwise zero. In the model, the source terms, S_i , in the governing equations include the generation and consumption due to reactions and interfacial mass transport. The source terms for cerium ions are summarized in Table 3.

The cerium ions can initially be assumed to be evenly distributed throughout the ionomer phase of the MEA, since ceria dissolution has been observed after fuel cell conditioning [27, 39]. Moreover, the dissolved Ce^{4+} is electrochemically reduced to Ce^{3+} at both anode and cathode due to the high electrochemical potential of the $\text{Ce}^{3+}/\text{Ce}^{4+}$ couple [21]. It is therefore assumed that cerium exists solely in the Ce^{3+} form at the beginning of the

simulation:

$$c_{\text{Ce}^{3+},0} = 93.3 \text{ mol m}^{-3} \quad (15)$$

$$c_{\text{Ce}^{4+},0} = 0 \quad (16)$$

$$c_{\text{CeO}_2,0} = 0. \quad (17)$$

The initial cerium ion concentration is equivalent to 1.1 wt% cerium oxide relative to the polymer mass in the membrane, which is the typical concentration for CeO₂-Nafion composite membrane [20, 22, 24, 25]. Cerium washout from the MEA is neglected, and therefore zero fluxes are assumed at the CL and MPL interfaces.

3. Results and Discussion

The proposed MEA model is first validated with experimental data and applied to scrutinize the *in situ* chemical stabilization mechanism in a ceria-supported MEA subjected to the aggressive cyclic OCV AST condition [27]. However, during duty operation, fuel cells are normally operated below OCV in order to generate power for practical purposes. The cell voltage is therefore an important parameter for evaluating the chemical stabilization of the membrane. The effectiveness of the ceria additive on mitigating chemical degradation under practical fuel cell operating voltages is then explored. Finally, the influences of ceria precipitation on the cerium distribution and chemical mitigation in the ceria-supported MEA are also simulated.

3.1. Open Circuit Voltage

In order to judge the stabilization mechanism, a baseline MEA which is a standard MEA without ceria additive is set as a benchmark. The chemical degradation process in the baseline and ceria-supported MEAs can be described in terms of the reaction-transport phenomena which are simulated in this work. The obtained results are then used to investigate the mitigation effect provided by the ceria additive and describe the underlying stabilization mechanism.

Chemical degradation of PFSA ionomer membranes involves radical induced ionomer side chain cleavage and unzipping and main chain scission, unzipping, and fragmentation [4, 18, 19, 42]. Fluoride species are released from the ionomer during the various steps of the degradation processes. Since the emitted fluorides can be traced and collected during fuel cell operation, fluoride emission measurement is widely adopted to quantify the level of chemical degradation in the membrane [4, 10]. Fig. 2 shows the simulated cumulative fluoride release in the baseline and ceria-supported MEAs as a function of operational time at OCV based on the proposed model. The simulated results are compared and evaluated against measured data from cyclic OCV AST experiments [27]. The proposed model successfully simulates the mitigating effect found in the ceria-supported MEA, which is illustrated by the coinciding fluoride emission trends of the simulated and experimental data in both baseline and ceria-supported MEAs. In the simulation, it takes about 870 hours for the cumulative fluoride release to reach 0.113 mol m^{-2}

in the ceria-supported MEA. On the other hand, the baseline MEA is able to emit as much fluoride in merely 20 hours, and its cumulative fluoride release reaches 1.15 mol m^{-2} at 130 hours. The simulated fluoride emission rate (FER) which equals the cumulative fluoride release divided by the time is 68 times lower in the ceria-supported MEA than in the baseline MEA. This calculated result is in good agreement with the experimental result, in which the FER of the baseline MEA is 59 times that of the ceria-supported MEA.

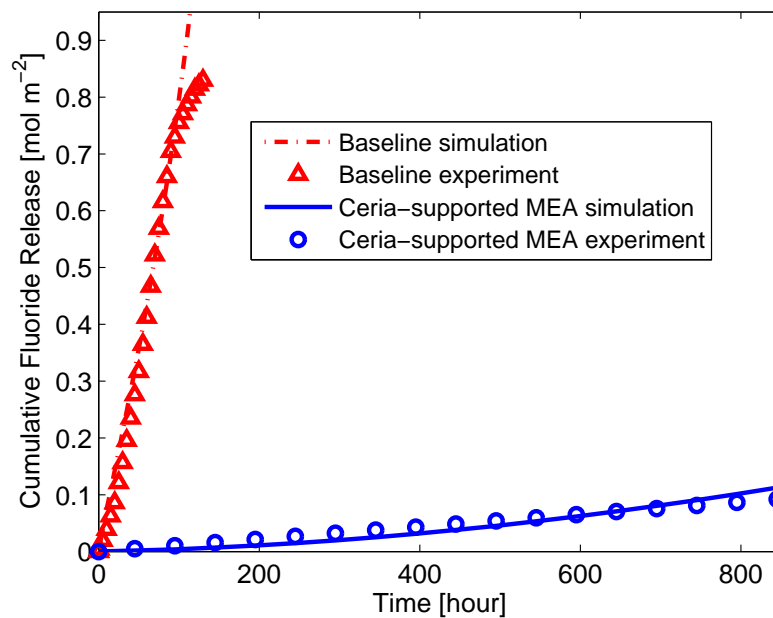


Figure 2: Measured and simulated cumulative fluoride release in the baseline and ceria-supported MEAs as a function of operational time at OCV.

The dramatic reduction of the membrane degradation observed in the ceria-supported MEA depends on the progression of hydroxyl radicals ($\cdot\text{OH}$), which are responsible for the chemical decay of the ionomer [4, 18, 42]. Given

that $\cdot\text{OH}$ can be formed from hydrogen peroxide through Fenton's reaction [15, 43], a reduced supply of hydrogen peroxide would lead to a lower $\cdot\text{OH}$ formation rate and thereby alleviate the membrane degradation.

In the ceria-supported MEA, the $\cdot\text{OH}$ formation rate is $8.6 \times 10^{-7} \text{ mol m}^{-2} \text{ s}^{-1}$ which is 14% lower than that in the baseline MEA ($10^{-6} \text{ mol m}^{-2} \text{ s}^{-1}$) because of the hydrogen peroxide quenching provided by Ce^{4+} (Reaction 3). Unfortunately, this difference is not significant enough for resolving the enormous reduction in the membrane degradation rate, and hence the lower $\cdot\text{OH}$ formation rate could not be the primary mitigating mechanism produced by the ceria additive.

Instead, the chemical stabilization mechanism is highly related with the suppression of ionomer damage due to $\cdot\text{OH}$ attack. The damage rates, calculated as the sum of all reaction rates between $\cdot\text{OH}$ and ionomer including both side and main chains, are calculated and depicted in Fig. 3. In the baseline MEA, the damage rate is almost two orders of magnitude higher than in the ceria-supported MEA because about 93% of the $\cdot\text{OH}$ reacts with the ionomer. This damage ratio is calculated by: $f_{\text{damage}} = r_{\text{damage}}/r_{\text{overall}}$, where r_{damage} represents the damage rate, and r_{overall} represents the sum of all $\cdot\text{OH}$ reaction rates. On the other hand, once ceria is introduced in MEA, the damage ratio descends to only 1.53% revealing that $\cdot\text{OH}$ attack is negligible. This minuscule damage ratio could be explained by the scavenging ratio which is defined as the fraction of $\cdot\text{OH}$ quenched: $f_{\text{scavenging}} = r_5/r_{\text{overall}}$. Under AST OCV conditions, the scavenging ratio is around 98%, indicating that almost

all $\cdot\text{OH}$ formed are quenched by Ce^{3+} (Reaction 5) before they can attack the membrane. The fast $\cdot\text{OH}$ scavenging by Ce^{3+} therefore represents the principal mitigating mechanism provided by the ceria additive.

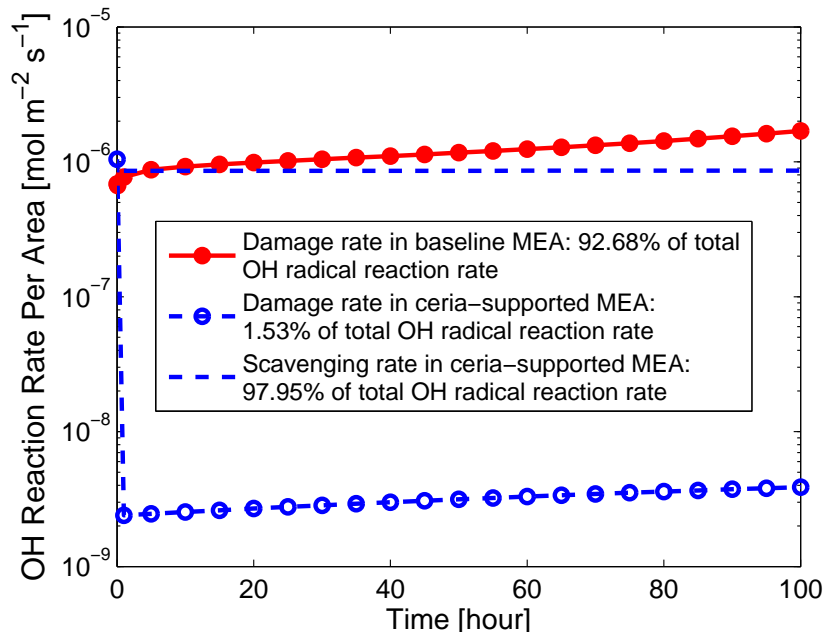


Figure 3: Simulated $\cdot\text{OH}$ reaction rates in the membrane under OCV condition.

In hydrogen PEFCs, electrochemical reduction of Ce^{4+} via the $\text{Ce}^{3+}/\text{Ce}^{4+}$ redox reaction (labeled as Reaction 7) is favorable. The local potentials at OCV conditions at the anode and cathode CLs are around zero and 1 V, respectively, which are considerably negative of the standard electrochemical potential of the $\text{Ce}^{3+}/\text{Ce}^{4+}$ redox couple (*i.e.*, 1.44 V [30]). Hence, Ce^{4+} can be efficiently reduced in the anode and cathode CLs by hydrogen and water, respectively [21]. As a result, Ce^{3+} is the dominant oxidation state which

entails more than 99% of the cerium ions in the CLs. In the membrane, there are two chemical reactions (Reactions 4 and 5) which oxidize Ce^{3+} to Ce^{4+} . Reaction 5, which executes the mitigation of chemical degradation, only contributes a small portion of the total Ce^{3+} oxidation in the membrane which is indicated by the two orders of magnitude lower reaction rate shown in Fig. 4. Indeed, the vast majority of Ce^{3+} ($> 99\%$) is oxidized to Ce^{4+} via reaction 4 by hydroperoxyl radical ($\cdot\text{OOH}$) which is a secondary radical formed in the membrane due to the reactions between $\cdot\text{OH}$ and dissolved hydrogen and oxygen [19]. Fortunately, Ce^{4+} can be reduced back to Ce^{3+} by hydrogen peroxide (Reaction 3) which is continuously generated in the MEA via the two-electron ORR. The Ce^{3+} regeneration is observed to predominantly takes place in the membrane via the H_2O_2 pathway rather than in the CLs via the redox reaction. Therefore, Ce^{4+} transport to the CLs and subsequent reduction to Ce^{3+} is not required to ensure Ce^{3+} presence in the membrane where it maintains effective membrane protection during the otherwise aggressive OCV condition.

3.2. Cell Voltages Below OCV

The *in situ* reaction-transport simulations are repeated at different cell voltages and the obtained FERs are plotted in Fig. 5. In the baseline MEA, the FER decreases with decreasing cell voltage which is attributed to the reduced magnitude of the iron redox cycle and hydrogen peroxide concentration within the MEA leading to a lower $\cdot\text{OH}$ formation rate. Further details

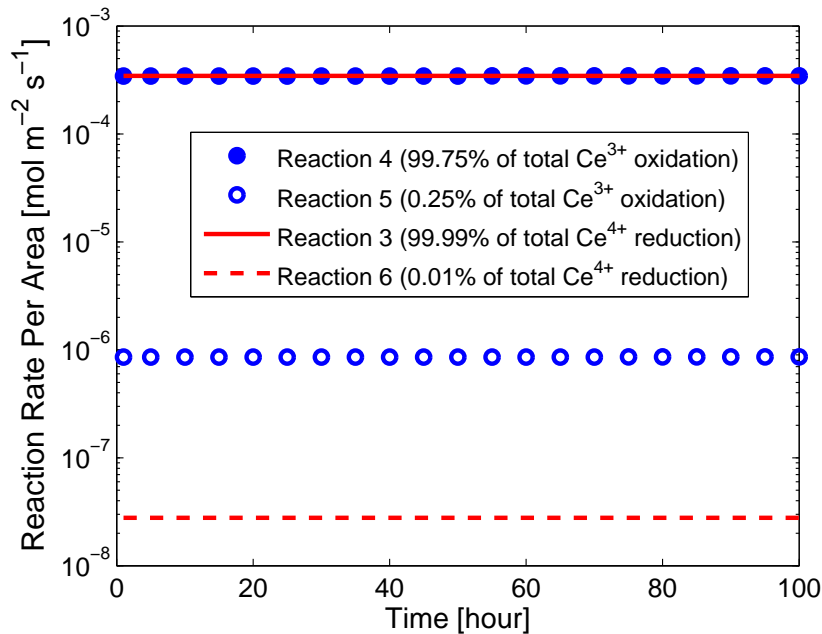


Figure 4: Simulated cerium ion reaction rates in the membrane under OCV condition.

about the underlying reason for the effect of cell voltage on the degradation rate of the baseline MEA are provided in our previous publication [19]. Generally, the ceria-supported MEA has a lower FER than the baseline MEA, as shown in Fig. 5. Interestingly, the FER increases when the cell voltage decreases from OCV to 0.6 V and then levels off, which is in stark contrast to the decreasing FER trend of the baseline. The FER differential between the ceria-supported and baseline MEAs is thus descending rapidly with decreasing cell voltage from OCV to 0 V, which suggests that the ceria additive provides the strongest mitigation at OCV, but its strength cannot be sustained when the cell voltage is held below OCV.

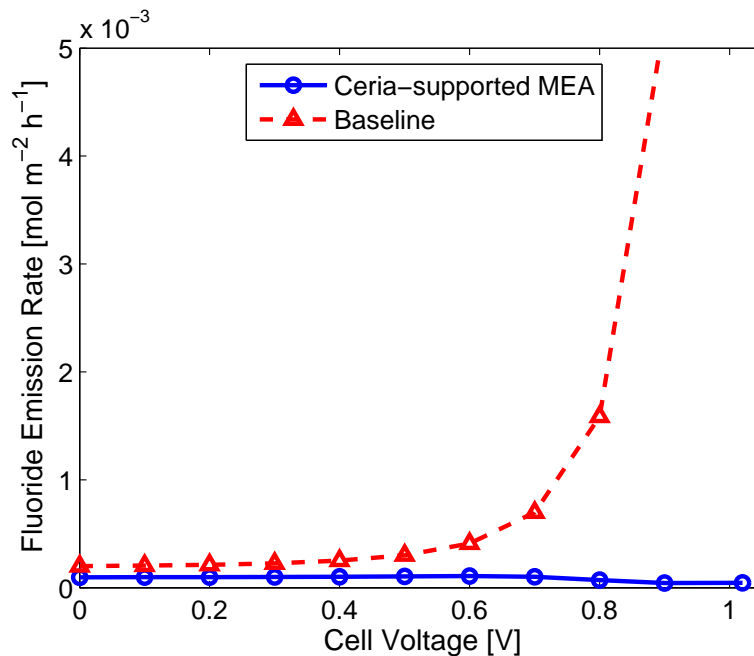


Figure 5: Simulated fluoride emission rates in the baseline and ceria-supported MEAs as a function of cell voltage.

The increasing FER of the ceria stabilized MEA at low cell voltages compared to the rate at OCV is first analyzed by calculating the damage and scavenging ratios that quantify $\cdot\text{OH}$ attack and radical scavenging. These metrics are plotted as a function of cell voltage in Fig. 6. The scavenging ratio decreases significantly when the cell voltage is reduced from OCV, revealing that fewer $\cdot\text{OH}$ are quenched by Ce^{3+} . More $\cdot\text{OH}$ are then available to attack the ionomer in the membrane, and this results in a growth of the damage ratio when the cell voltage is decreased from OCV. Ce^{3+} still prevails in the membrane, because Ce^{4+} can be effectively reduced to Ce^{3+} by hydrogen peroxide in the membrane or via the redox reaction in both CLs. Since zero

fluxes are assumed at the MPL and CL interfaces, the total amount of Ce^{3+} is therefore stable in the MEA with respect to changes in cell voltage. On the same token, the reduction in the total amount of Ce^{3+} due to oxidation or leakage is not an appropriate mechanism for the drop in $\cdot\text{OH}$ scavenging rate.

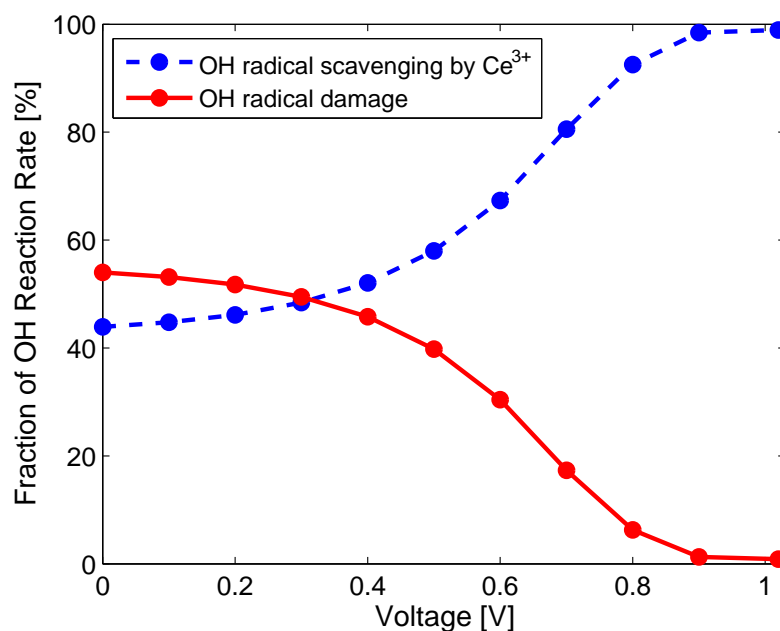


Figure 6: Simulated damage and scavenging ratios as a function of cell voltage.

The significant reduction in the mitigation effectiveness and the increased FER observed in the ceria stabilized MEA are in fact highly related to the Ce^{3+} distribution in the MEA rather than the total amount of Ce^{3+} present. When the cell is held at OCV, there is no current or ionomer potential gradient across the MEA. Ion migration due to the ionomer potential gradient

is therefore negligible, and diffusion is the dominant mode of cerium ion transport between anode and cathode CLs. Diffusion drives Ce^{3+} from high concentration to low concentration, and hence a uniform equilibrium distribution in the MEA is formed, as shown in Fig. 7. The stable Ce^{3+} supply in the membrane secures the $\cdot\text{OH}$ scavenging which results in the strongest mitigation observed at OCV.

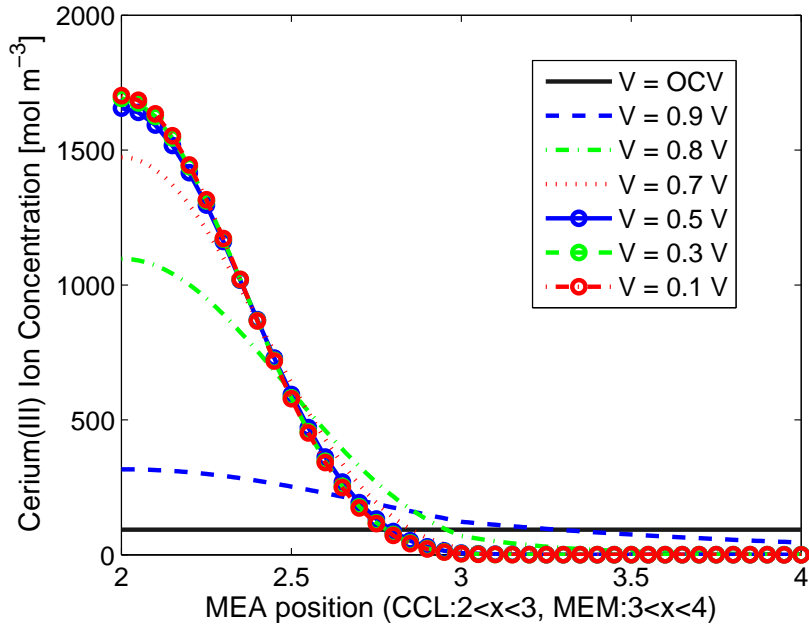


Figure 7: Simulated distribution of cerium(III) ions in the ceria-supported MEA under different cell voltages after one hour of operation ($t = 1$).

When the fuel cell is operated at cell voltages below OCV, an ionomer potential gradient across the MEA is formed by the regular electrochemical reactions in hydrogen PEFCs, *i.e.*, the hydrogen oxidation reaction (HOR) at the anode CL and the four-electron ORR at the cathode CL. The obtained

ionomer potential decreases from anode to cathode and attains its minimum at the cathode CL and MPL interface ($x = 2$). As Ce^{3+} is a positively charged species, it migrates from the anode CL to the cathode CL across the membrane. This Ce^{3+} ion migration leads to considerable Ce^{3+} accumulation in the cathode CL, as shown in Fig. 7.

When the cell voltage is reduced from OCV to 0.5 V, the ionomer potential gradient across the membrane increases dramatically due to the faster HOR and four-electron ORR. The resulted potential gradient drives more Ce^{3+} from the membrane to the cathode CL, and thereby the Ce^{3+} concentration in the membrane is largely reduced, as illustrated in Fig. 7. Without enough Ce^{3+} in the membrane, the influence of $\cdot\text{OH}$ scavenging is diluted, and thereby the mitigation effectiveness indicated by the ratios of the FER and membrane thinning rate of the baseline MEA to those of the ceria-supported MEA are largely suppressed, as shown in Fig. 8. For example, a ten-fold reduction in mitigation effectiveness is simulated under low cell voltages ($V < 0.7$ V). Therefore, a close correlation between the observed trends in reduced mitigation effectiveness and the reduced Ce^{3+} concentration in the membrane is found at these cell voltages.

A near zero Ce^{3+} membrane concentration is obtained when the cell voltage is held at 0.5 V, which suggests that further reductions in cell voltage may have limited effect. Indeed, the Ce^{3+} membrane concentration almost levels off even when the cell voltage is further decreased from 0.5 V to 0 V. The corresponding mitigation effect at low cell voltages is thus relatively

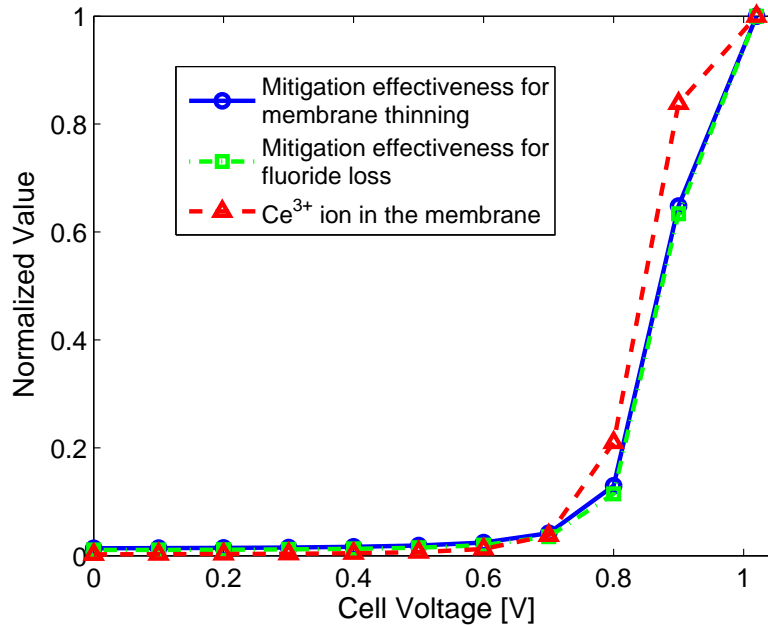


Figure 8: Mitigation effectiveness of ceria as a function of cell voltage. The values for fluoride loss and membrane thinning mitigation are normalized by the effectiveness observed at the OCV condition, where the radical scavenging ratio is close to unity. The normalized cerium(III) ion concentration in the membrane is shown for comparison.

constant and insignificant compared to the cases at high cell voltages, as shown in Fig. 8. Fortunately, the overall rates of chemical degradation at these cell voltages are substantially lower than those at OCV conditions [19]. Therefore, although the mitigation effects are insignificant, the FERs are considerably lower than those at OCV conditions without ceria additive.

3.3. Ceria Precipitation

Ceria precipitation is possible when the fuel cell is operated at cell voltages below OCV because of cerium ion migration and accumulation in the

cathode CL that reduce the acidity of the ionomer phase. Fig. 9 describes the dynamics of ceria precipitation by showing Ce^{3+} and ceria concentrations at different operating hours, *i.e.*, $t = 1$, $t = 5$, and $t = 100$. When the cell is held at 0.8 V, the developed ionomer potential gradient drives Ce^{3+} towards the cathode CL and MPL interface ($x = 2$). Since the ionomer potential strictly decreases from the anode CL and MPL interface ($x = 5$), the resulted Ce^{3+} concentration in the ionomer phase of the MEA is a gradually increasing function of x ranging from 2 (anode CL-MPL interface) to 5 (cathode CL-MPL interface). Therefore, the cathode CL can be divided into two regions: a saturated region and an unsaturated region. In the saturated region, the Ce^{3+} concentration exceeds the saturation concentration of the ionomer such that ceria precipitation occurs. On the other hand, precipitation does not occur in the unsaturated region because the Ce^{3+} concentration is below saturation. The position at which the cathode CL is divided into the saturated and unsaturated regions is denoted as the saturation front and can be defined mathematically as $x_{\text{sf}} = \arg \min |c_{\text{Ce}^{3+}}(x) - c_{\text{Ce,sat}}|$. Similarly, the cathode CL can be separated into two regions by the ceria distribution: a ceria region and a non-ceria region. The ceria region represents the part of the CL that contains ceria precipitate, while the non-ceria region represents the part of the CL that only contains cerium ions but no ceria precipitate. The boundary that separates the two regions is termed the ceria front, *i.e.*, x_{cf} .

Once ceria precipitation occurs due to ionomer saturation of Ce^{3+} , the

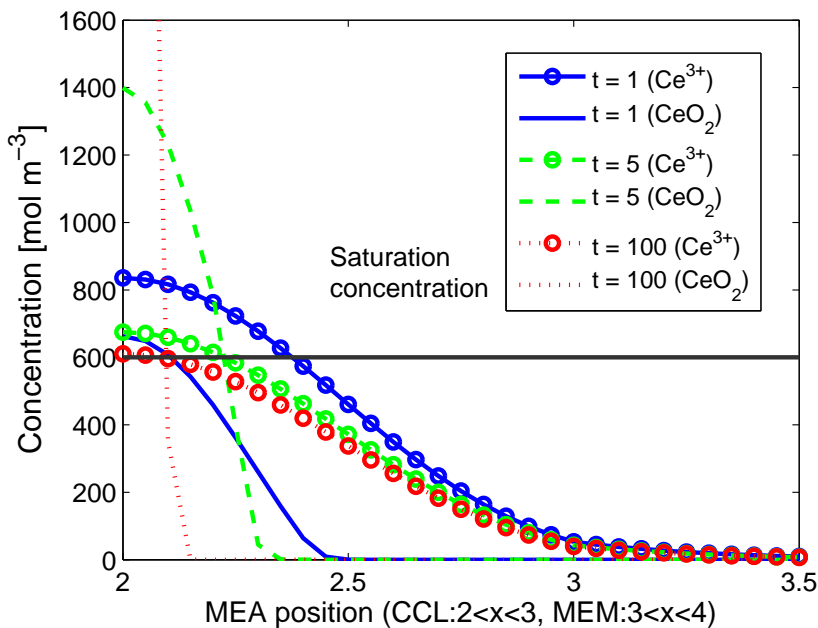


Figure 9: Simulated cerium(III) ion and ceria concentration distributions in the MEA as a function of time at 0.8 V

amount of Ce^{3+} is reduced in the saturated region, which shifts the saturation front closer to $x = 2$ than the ceria front. The ceria precipitate located between the two fronts is now in the unsaturated region, and the precipitation reaction is reversed. Therefore the precipitate dissolves back into Ce^{3+} which becomes mobile in the ionomer. The mobile Ce^{3+} redistributes in the MEA and again accumulates towards $x = 2$ according to the ionomer potential. This dissolution consumes the ceria precipitate near the ceria front, which thereby shifts the ceria front towards $x = 2$. On the other hand, the ceria in the narrowed saturated region maintains its precipitate form, and new ceria precipitate is formed because the local Ce^{3+} is saturated. The resulted ceria

concentration therefore continues to increase, and a higher peak is obtained, as shown in Fig. 9. The described precipitation and dissolution cycle results in a gradual shift in the saturation and ceria fronts, as illustrated by the Ce^{3+} and ceria concentration profiles at $t = 1$, $t = 5$, and $t = 100$ seen in Fig. 9 and results in a large, well-defined ceria precipitation peak at equilibrium after sufficient time at steady state, which is possibly related with cerium washout.

The ionomer potential plays a fundamental role in the ceria precipitate formation which is therefore a function of the cell voltage. Ce^{3+} and ceria concentration distributions in the MEA after 10 hours of operation at different cell voltages are simulated and plotted in Fig. 10. When the cell voltage is reduced from 0.9 to 0.5 V, the considerable increase in the ionomer potential gradient leads to a significant increase in the Ce^{3+} concentration in the cathode CL due to the ion migration from the membrane and anode. As the precipitation rate is proportional to the difference between the instantaneous Ce^{3+} concentration and its saturation concentration, the formation rate of ceria precipitate is elevated, resulting in a dramatic increase in ceria concentration, as illustrated in Fig. 10(a). The near zero Ce^{3+} concentration in the membrane at low cell voltages ($V < 0.5$ V) limits the further growth in the precipitation rate. The simulated ceria concentration profiles under low cell voltages are therefore nearly identical, as shown in Fig. 10(b), due to the comparable formation rates.

Ceria precipitation suppresses the chemical stabilization mechanism in

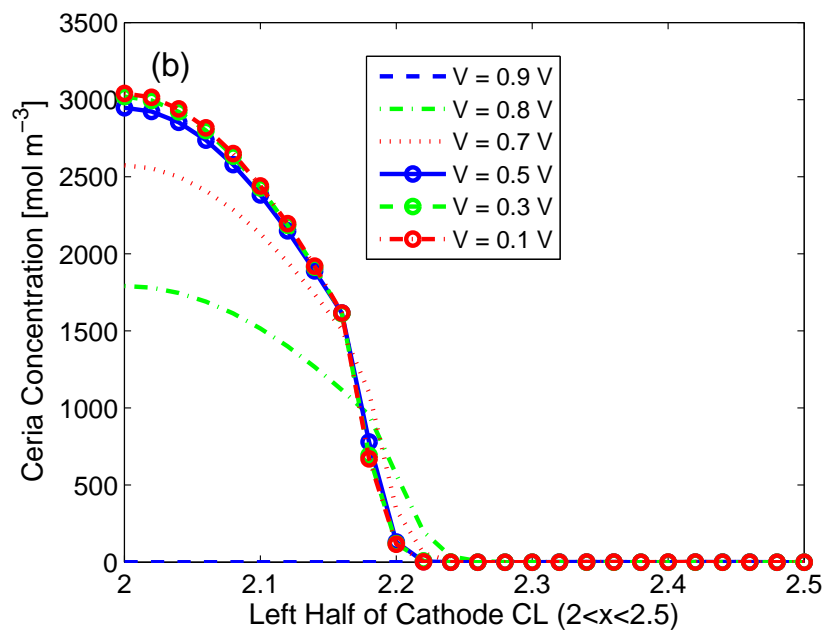
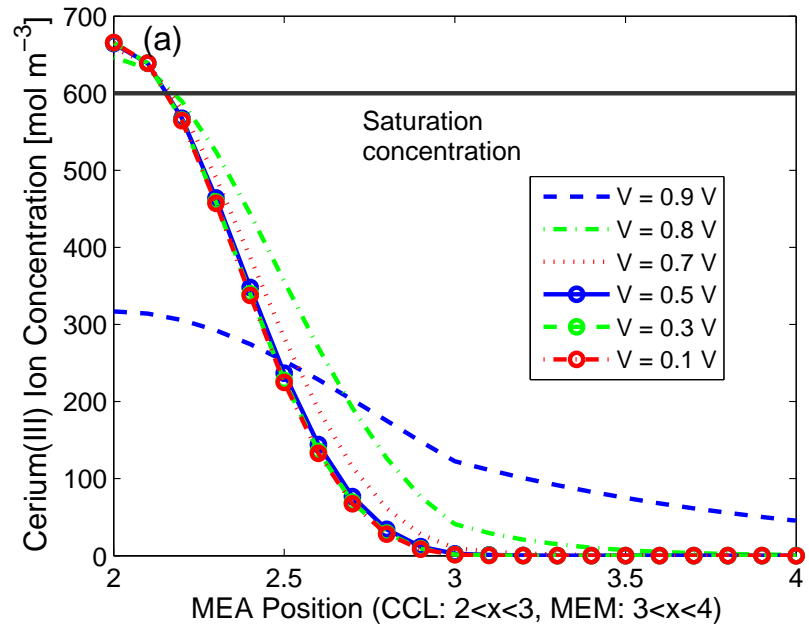


Figure 10: (a) Cerium(III) ion and (b) ceria concentration distributions in the MEA after 10 hours of operation ($t = 10$) at different cell voltages.

the ceria-supported MEA, which is demonstrated by the higher FER plotted in Fig. 11(a). Ceria precipitation removes the Ce^{3+} and limits the growth of the Ce^{3+} concentration at the cathode CL, and thereby the Ce^{3+} concentration is lower with precipitation than without precipitation, which is illustrated in Fig. 10. The back diffusion of Ce^{3+} from the cathode CL to the anode CL is diminished, and less Ce^{3+} is driven into the membrane by the diffusive transport, as indicated by the lower Ce^{3+} membrane concentration in Fig. 11(b). As a consequence, ceria precipitation greatly eliminates the benefits of ceria at cell voltages below 0.5 V by comparing the FERs in the ceria precipitated and baseline MEAs, as illustrated Fig. 11(a).

4. Conclusions

The *in situ* chemical stabilization mechanism of ceria-supported MEAs in hydrogen PEFCs is analyzed using a comprehensive, transient membrane degradation and mitigation model. The vast majority of the cerium ions are found to be in the desired Ce^{3+} oxidation state, which is a result of hydrogen peroxide supported regeneration of Ce^{3+} in the membrane. This regeneration mitigates the overall chemical degradation in ceria stabilized MEAs; however, it cannot secure the effectiveness of the ionomer membrane protection across the entire range of cell voltages experienced during fuel cell operation. When the cell voltage is held at OCV, Ce^{3+} is uniformly distributed in the ionomer phase of the MEA and thus maintains a high Ce^{3+} concentration in the membrane which leads to an effective protection of the

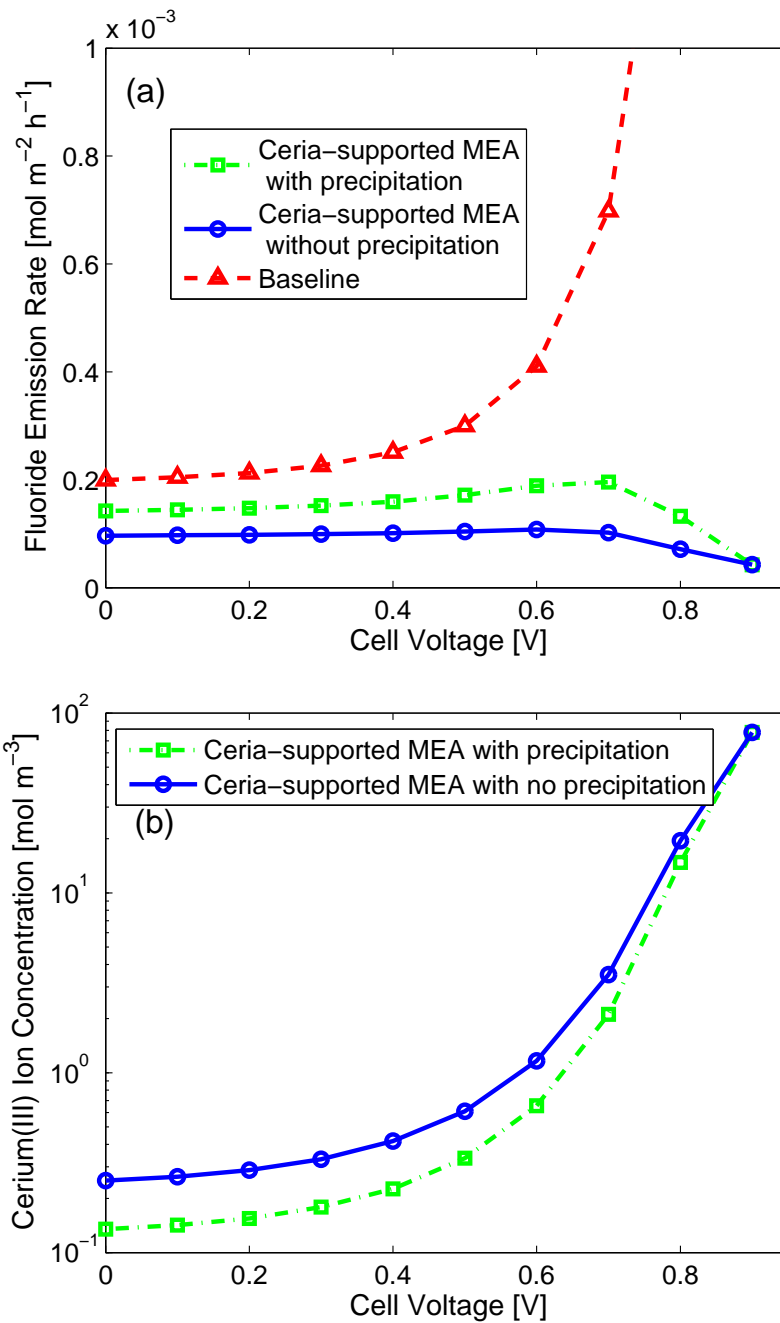


Figure 11: Simulated (a) fluoride emission rate and (b) cerium(III) ion membrane concentrations of ceria-supported MEAs with and without ceria precipitation, shown as a function of cell voltage. The simulated fluoride emission rate in the baseline MEA is shown in (a) for comparison.

membrane via $\cdot\text{OH}$ quenching. Therefore, the ceria additive is particularly effective at high cell voltages where the degradation rates are the highest. When the cell voltage is decreased, the protection is significantly reduced. Most of the Ce^{3+} migrate into the cathode CL due to the ionomer potential gradients across the MEA, and the remaining Ce^{3+} concentration in the membrane is found to decrease exponentially as the cell voltage is reduced. The $\cdot\text{OH}$ scavenging is dramatically suppressed without an adequate amount of Ce^{3+} in the membrane, resulting in a ten-fold reduction in mitigation effectiveness under low cell voltages ($V < 0.7 \text{ V}$). Interrelated effects of ceria precipitation in the CLs on the stabilization mechanism are also observed. It is found that ceria precipitation would further reduce the Ce^{3+} concentration in the membrane and may potentially eliminate the benefits of ceria at cell voltages below 0.5 V.

Acknowledgements

This research was supported by Ballard Power Systems and the Natural Sciences and Engineering Research Council of Canada through an Automotive Partnership Canada (APC) grant. The authors wish to thank their colleagues at SFU FCREL and Ballard for providing valuable comments and advices.

Reference

- [1] M. P. Rodgers, L. J. Bonville, H. R. Kunz, D. K. Slattery, J. M. Fenton, Fuel cell perfluorinated sulfonic acid membrane degradation correlating accelerated stress testing and lifetime, *Chem. Rev.* 112 (11) (2012) 6075–6103.
- [2] C. Gittleman, F. Coms, Y.-H. Lai, Chapter 2 - membrane durability: Physical and chemical degradation, in: M. Mench, E. C. Kumbur, T. N. Veziroglu (Eds.), *Polymer Electrolyte Fuel Cell Degradation*, Academic Press, Boston, 2012, pp. 15 – 88.
- [3] X. Huang, R. Solasi, Y. Zou, M. Feshler, K. Reifsnider, D. Condit, S. Burlatsky, T. Madden, Mechanical endurance of polymer electrolyte membrane and pem fuel cell durability, *J. Polym. Sci. B Polym. Phys.* 44 (16) (2006) 2346–2357.
- [4] C. Lim, L. Ghassemzadeh, F. Van Hove, M. Lauritzen, J. Kolodziej, G. G. Wang, S. Holdcroft, E. Kjeang, Membrane degradation during combined chemical and mechanical accelerated stress testing of polymer electrolyte fuel cells, *J. Power Sources* 257 (0) (2014) 102 – 110.
- [5] M.-A. Goulet, R. M. H. Khorasany, C. De Torres, M. Lauritzen, E. Kjeang, G. G. Wang, N. Rajapakse, Mechanical properties of catalyst coated membranes for fuel cells, *J. Power Sources* 234 (0) (2013) 38 – 47.

- [6] A. Sadeghi Alavijeh, M.-A. Goulet, R. M. H. Khorasany, J. Ghataurah, C. Lim, M. Lauritzen, E. Kjeang, G. G. Wang, R. K. N. D. Rajapakse, Decay in mechanical properties of catalyst coated membranes subjected to combined chemical and mechanical membrane degradation, *Fuel Cells* 15 (1) (2015) 204–213.
- [7] R. M. H. Khorasany, M.-A. Goulet, A. Sadeghi Alavijeh, E. Kjeang, G. G. Wang, R. K. N. D. Rajapakse, On the constitutive relations for catalyst coated membrane applied to in-situ fuel cell modeling, *J. Power Sources* 252 (0) (2014) 176 – 188.
- [8] R. M. H. Khorasany, A. Sadeghi Alavijeh, E. Kjeang, G. G. Wang, R. K. N. D. Rajapakse, Mechanical degradation of fuel cell membranes under fatigue fracture tests, *J. Power Sources* 274 (0) (2015) 1208 – 1216.
- [9] R. M. H. Khorasany, E. Kjeang, G. G. Wang, R. K. N. D. Rajapakse, Simulation of ionomer membrane fatigue under mechanical and hydrothermal loading conditions, *J. Power Sources* 279 (0) (2015) 55 – 63.
- [10] N. Macauley, A. Alavijeh Sadeghi, M. Watson, J. Kolodziej, M. Lauritzen, S. Knights, G. G. Wang, E. Kjeang, Accelerated membrane durability testing of heavy duty fuel cells, *J. Electrochem. Soc.* 162 (1) (2015) F98–F107.
- [11] E. Endoh, S. Terazono, H. Widjaja, Y. Takimoto, Degradation study of

- mea for pemfcs under low humidity conditions, *Electrochem. Solid-State Lett.* 7 (7) (2004) A209–A211.
- [12] J. Healy, C. Hayden, T. Xie, K. Olson, R. Waldo, M. Brundage, H. Gasteiger, J. Abbott, Aspects of the chemical degradation of pfsa ionomers used in pem fuel cells, *Fuel Cells* 5 (2) (2005) 302–308.
- [13] L. Ghassemzadeh, K.-D. Kreuer, J. Maier, K. Müller, Chemical degradation of nafion membranes under mimic fuel cell conditions as investigated by solid-state nmr spectroscopy, *J. Phys. Chem. C* 114 (34) (2010) 14635–14645.
- [14] L. Gubler, S. M. Dockheer, W. H. Koppenol, Radical HO·, H· and HOO· formation and ionomer degradation in polymer electrolyte fuel cells, *J. Electrochem. Soc.* 158 (7) (2011) B755–B769.
- [15] L. Ghassemzadeh, S. Holdcroft, Quantifying the structural changes of perfluorosulfonated acid ionomer upon reaction with hydroxyl radicals, *J. Am. Chem. Soc.* 135 (22) (2013) 8181–8184.
- [16] A. B. LaConti, M. Hamdan, R. C. McDonald, Mechanisms of membrane degradation. *Handbook of Fuel Cells*, John Wiley & Sons, Ltd, 2003.
- [17] M. Inaba, T. Kinumoto, M. Kiriake, R. Umebayashi, A. Tasaka, Z. Ogumi, Gas crossover and membrane degradation in polymer electrolyte fuel cells, *Electrochim. Acta* 51 (26) (2006) 5746–5753.

- [18] K. Wong, E. Kjeang, Macroscopic in-situ modeling of chemical membrane degradation in polymer electrolyte fuel cells, *J. Electrochem. Soc.* 161 (9) (2014) F823–F832.
- [19] K. Wong, E. Kjeang, Mitigation of chemical membrane degradation in fuel cells: Understanding the effect of cell voltage and iron ion redox cycle, *ChemSusChem* 8 (6) (2015) 1072–1082.
- [20] P. Trogadas, J. Parrondo, V. Ramani, Degradation mitigation in polymer electrolyte membranes using cerium oxide as a regenerative free-radical scavenger, *Electrochem. Solid-State Lett.* 11 (7) (2008) B113–B116.
- [21] F. D. Coms, H. Liu, J. E. Owejan, Mitigation of perfluorosulfonic acid membrane chemical degradation using cerium and manganese ions, *ECS Trans.* 16 (2) (2008) 1735–1747.
- [22] S. Xiao, H. Zhang, C. Bi, Y. Zhang, Y. Zhang, H. Dai, Z. Mai, X. Li, Degradation location study of proton exchange membrane at open circuit operation, *J. Power Sources* 195 (16) (2010) 5305 – 5311.
- [23] Z. Wang, H. Tang, H. Zhang, M. Lei, R. Chen, P. Xiao, M. Pan, Synthesis of nafion/ceo2 hybrid for chemically durable proton exchange membrane of fuel cell, *J. Membrane Sci.* 421422 (0) (2012) 201 – 210.
- [24] B. Pearman, N. Mohajeri, R. P. Brooker, M. P. Rodgers, D. K. Slattery, M. D. Hampton, D. A. Cullen, S. Seal, The degradation mitigation effect

- of cerium oxide in polymer electrolyte membranes in extended fuel cell durability tests, *J. Power Sources* 225 (0) (2013) 75 – 83.
- [25] B. P. Pearman, N. Mohajeri, D. K. Slattery, M. D. Hampton, S. Seal, D. A. Cullen, The chemical behavior and degradation mitigation effect of cerium oxide nanoparticles in perfluorosulfonic acid polymer electrolyte membranes, *Polym. Degrad. Stabil.* 98 (9) (2013) 1766 – 1772.
- [26] L. Wang, S. G. Advani, A. K. Prasad, Degradation reduction of polymer electrolyte membranes using ceo₂ as a free-radical scavenger in catalyst layer, *Electrochimica Acta* 109 (0) (2013) 775 – 780.
- [27] C. Lim, A. Sadeghi Alavijeh, M. Lauritzen, J. Kolodziej, S. Knights, E. Kjeang, Fuel cell durability enhancement with cerium oxide under combined chemical and mechanical membrane degradation, *ECS Electrochem. Lett.* 4 (4) (2015) F29–F31.
- [28] S. A. Hayes, P. Yu, T. J. O’Keefe, M. J. O’Keefe, J. O. Stoffer, The phase stability of cerium species in aqueous systems: I. e-pH diagram for the CeHClO₄H₂O system, *J. Electrochem. Soc.* 149 (12) (2002) C623–C630.
- [29] D. Banham, S. Ye, T. Cheng, S. Knights, S. M. Stewart, M. Wilson, F. Garzon, Effect of ceox crystallite size on the chemical stability of ceox nanoparticles, *J. Electrochem. Soc.* 161 (10) (2014) F1075–F1080.
- [30] L. Gubler, W. H. Koppenol, Kinetic simulation of the chemical stabi-

- lization mechanism in fuel cell membranes using cerium and manganese redox couples, *J. Electrochem. Soc.* 159 (2) (2011) B211–B218.
- [31] C. Chan, N. Zamel, X. Li, J. Shen, Experimental measurement of effective diffusion coefficient of gas diffusion layer/microporous layer in pem fuel cells, *Electrochim. Acta* 65 (0) (2012) 13–21.
- [32] J. Shen, J. Zhou, N. G. C. Astrath, T. Navessin, Z.-S. Liu, C. Lei, J. H. Rohling, D. Bessarabov, S. Knights, S. Ye, Measurement of effective gas diffusion coefficients of catalyst layers of pem fuel cells with a loschmidt diffusion cell, *J. Power Sources* 196 (2) (2011) 674–678.
- [33] H. Wu, P. Berg, X. Li, Modeling of pemfc transients with finite-rate phase-transfer processes, *J. Electrochem. Soc.* 157 (1) (2010) B1–B12.
- [34] A. Z. Weber, C. Delacourt, Mathematical modelling of cation contamination in a proton-exchange membrane, *Fuel Cells* 8 (6) (2008) 459–465.
- [35] M. F. Serincan, U. Pasaogullari, T. Molter, Modeling the cation transport in an operating polymer electrolyte fuel cell (pefc), *Int. J. Hydrogen Energy* 35 (11) (2010) 5539 – 5551.
- [36] A. A. Shah, T. R. Ralph, F. C. Walsh, Modeling and simulation of the degradation of perfluorinated ion-exchange membranes in pem fuel cells, *J. Electrochem. Soc.* 156 (4) (2009) B465–B484.
- [37] D. You, H. Zhang, J. Chen, A simple model for the vanadium redox battery, *Electrochim. Acta* 54 (27) (2009) 6827 – 6836.

- [38] A. Shah, M. Watt-Smith, F. Walsh, A dynamic performance model for redox-flow batteries involving soluble species, *Electrochim. Acta* 53 (27) (2008) 8087 – 8100.
- [39] S. M. Stewart, D. Spornjak, R. Borup, A. Datye, F. Garzon, Cerium migration through hydrogen fuel cells during accelerated stress testing, *ECS Electrochem. Lett.* 3 (4) (2014) F19–F22.
- [40] C. Baddeley, A. W. Stephenson, C. Hardacre, M. Tikhov, R. M. Lambert, Structural and electronic properties of ce overlayers and low-dimensional pt-ce alloys on pt111, *Phys. Rev. B* 56 (1997) 12589–12598.
- [41] W. He, J. Yi, T. Van Nguyen, Two-phase flow model of the cathode of pem fuel cells using interdigitated flow fields, *AIChE J.* 46 (10) (2000) 2053–2064.
- [42] M. Ghelichi, P.-. A. Melchy, M. H. Eikerling, Radically coarse-grained approach to the modeling of chemical degradation in fuel cell ionomers, *J. Phys. Chem. B* 118 (38) (2014) 11375–11386.
- [43] L. Ghassemzadeh, T. J. Peckham, T. Weissbach, X. Luo, S. Holdcroft, Selective formation of hydrogen and hydroxyl radicals by electron beam irradiation and their reactivity with perfluorosulfonated acid ionomer, *J. Am. Chem. Soc.* 135 (42) (2013) 15923–15932.

CONFIDENTIAL

Appendix D: Simulation of Performance Tradeoffs in Ceria Supported Polymer Electrolyte Fuel Cells

Simulation of Performance Tradeoffs in Ceria Supported Polymer Electrolyte Fuel Cells

Ka Hung Wong* and Erik Kjeang^{†*}

Abstract

Ceria-supported membrane electrode assemblies (MEAs) can effectively protect the membrane at open circuit voltage conditions; however, performance tradeoffs have been observed experimentally with the use of membrane additives. In the present work, a comprehensive, transient *in situ* membrane durability model for ceria-supported MEAs is developed and applied to investigate the fundamental mechanisms of the performance tradeoffs. The modeling results reveal that proton starvation may occur in the cathode catalyst layer due to local Ce^{3+} accumulation and associated reductions in proton conductivity and oxygen reduction kinetics. Significant performance tradeoffs in the form of combined ohmic and kinetic voltage losses are therefore evident and shown to increase with current density. Reduced

*School of Mechatronic Systems Engineering, Simon Fraser University, 250-13450 102 Avenue, Surrey, BC V3T0A3 Canada

[†]Email address: ekjeang@sfu.ca

ceria additive loading and increased cathode ionomer volume fraction are proposed as potential mitigation strategies to reduce the voltage losses caused by proton starvation. A lower initial Ce^{3+} concentration is demonstrated to reduce voltage losses without compromising membrane durability at high cell voltages. However, the harmful Fe^{2+} concentration in the membrane increases with the Ce^{3+} concentration, which suggests that ceria-supported MEAs can experience higher rates of degradation than baseline MEAs at low cell voltages. Strategic MEA design and optimization is recommended in order to ensure membrane durability at low cell voltages.

1 Introduction

In low temperature polymer electrolyte fuel cells (PEFCs), perfluorosulfonic acid (PFSA) ionomer membranes are the industry standard electrolyte material used to maintain effective fuel cell operation. PFSA ionomer membranes are advanced thin-film structures with superior ionic conductivity, electrical insulation, and resistance toward reactant permeation. Despite of its mechanically and chemically stable perfluorinated main chain, the ionomer membrane still undergoes various forms of degradation in fuel cell environments [1, 2]. Membrane failures that lead to lifetime limiting hydrogen leaks across the membrane electrolyte assembly (MEA) are generally observed in the presence of combined chemical and mechanical stress [3, 4].

Generation of water and heat in the cathode catalyst layer (CL) during

fuel cell operation leads to significant water content and temperature gradients in the MEA as well as considerable temporal dynamics during load changes. Additionally, both water and heat can be transferred across the membrane in both directions between the anode and cathode CLs. Hence, the membrane experiences regular variations in internal hygrothermal conditions that induce swelling and contraction, and mechanical stress due to confinement within the MEA [5]. Although pure mechanical failures are possible for membranes subjected to 10^5 repeated hygrothermal cycles [6, 7], the lifetime limiting hydrogen leaks are believed to be initiated by chemical membrane degradation. The physicochemical and mechanical properties of the membrane are dramatically deteriorated when the MEA is subjected to the conditions in which chemical membrane degradation is evaluated, further exacerbating the rate to failure [3, 4, 8, 9].

In PEFCs, hydrogen peroxide (H_2O_2) can be generated via the two-electron oxygen reduction reaction (ORR) at the anode and cathode CLs provided that the electrode potentials are sufficiently low (< 0.695 V). When metal contaminants such as Fe^{2+} and Cu^+ are present, hydrogen peroxide can decompose to hydroxyl radicals ($\cdot\text{OH}$) [10, 11, 12]. The hydroxyl radicals formed are highly reactive and can attack the ionomer membrane in terms of molecular side chain cleavage and unzipping [12, 13, 14, 15, 16, 17, 18, 19] which is responsible for the deteriorated physicochemical properties observed in degraded membranes [20].

Considering the dominant role of hydroxyl radicals in the chemical mem-

brane degradation, radical scavenging is proposed to mitigate the chemical damage by quenching the radicals before they attack the ionomer. One of the most promising additives to quench $\cdot\text{OH}$ in fuel cells is ceria (CeO_2), which has been shown to effectively protect the ionomer membrane under open circuit voltage (OCV) accelerated stress test (AST) or *ex situ* Fenton's durability test conditions [21, 22, 23, 24, 25, 26, 27]. Ceria in general can dissolve in acidic aqueous environments provided that the electrochemical potential is not too high (below 1.76 V) according to the Pourbaix diagram for cerium [28]. Due to the high proton concentration ($c_{\text{H}^+} \approx 1800 \text{ mol m}^{-3}$) and relatively low operating potentials (0 – 1 V) of PEFCs, ceria dissolves and forms a $\text{Ce}^{3+}/\text{Ce}^{4+}$ redox couple in the ionomer phase when it is incorporated in the CLs or membrane [27, 29]. The multivalent nature of the redox couple allows the cerium ions to alternate between the two oxidation states: Ce^{3+} and Ce^{4+} , which is considered a critical asset for sustainable chemical protection of the ionomer membrane from radical attack [22]. The Ce^{3+} ion can react with $\cdot\text{OH}$ and oxidize to the Ce^{4+} ion, while the Ce^{4+} ion can be reduced to the Ce^{3+} ion by reacting with hydrogen peroxide or hydrogen [13]. However, the distribution, transport, and formation/consumption of cerium ions within a fuel cell would be very challenging to measure quantitatively within an operating fuel cell [30]. The experimental challenges and limitations of *in situ* measurements suppress the technical progress in developing an effective CeO_2 based durable MEA. On the other hand, modeling platforms which predict the chemical membrane degradation and mitigation

provide an adequate tool for this purpose.

Kinetic models [15, 19, 31, 32] have been developed to investigate ionomer degradation processes under a specific environment which is not linked with the operating fuel cell conditions. Shah *et al.* [33], Coulon *et al.* [34], Gummalla *et al.* [35], and Wong *et al.* [18] developed MEA degradation models based on conservation laws to account for the transport phenomena of an operating fuel cell and their effect on membrane degradation. In these models, hydroxyl radical formation via hydrogen peroxide decomposition on Fe^{2+} (Fenton's reaction) [18, 33, 34] or on the surface of platinum deposited in the membrane [35] was assumed. However, the transport and reaction phenomena of the metal contaminants were generally neglected in the simulations. The role of the transport-reaction phenomena of $\text{Fe}^{2+}/\text{Fe}^{3+}$ was first investigated using the model developed by Wong and Kjeang [12]. The modeling investigations suggested that the concentration of the harmful and mobile Fe^{2+} in the membrane decays exponentially when the cell voltage is reduced, which elucidated the mitigating effect of reduced cell voltage on the chemical membrane degradation. Only two models developed to date have considered the use of radical scavengers [32, 36]. Gubler *et al.* [32] modeled the cerium ion mitigation process by means of an *ex situ* kinetic simulation and concluded that the mitigation effect is based on the rapid $\cdot\text{OH}$ quenching facilitated by Ce^{3+} . Wong and Kjeang [36] developed an *in situ* MEA model to include the transport-reaction phenomena of mobile $\text{Ce}^{3+}/\text{Ce}^{4+}$ and their interrelated effects on the mitigation mechanisms. The model showed that

while the mitigation effectiveness is high at high cell voltages, it is substantially reduced at low cell voltages where ion migration drives Ce^{3+} ions from the membrane into the cathode CL.

Although ceria additive can mitigate membrane degradation at OCV conditions, it has also been shown to compromise the fuel cell performance [37]. The performance drop is believed to share the same performance degradation mechanism with other cations contamination (such as iron and copper ions) which is associated with reduced proton concentration and conductivity in the membrane [38, 39, 40] since ceria can dissolve into the ionomer phase and bond to the sulfonic acid end group. In this context, several cation contamination models have been developed to explore this type of degradation [41, 42, 43, 44]; however, no *in situ* models that describe the effects of ceria additive on the fuel cell performance have been published to date. These models cannot be directly applied to study cerium ion transport and its impact on fuel cell performance since none of them simultaneously address the initial embedded ceria in the membrane during MEA fabrication, resulting in a fixed amount of cerium ions in the MEA, and the cerium ion transport in the CLs resulting in a significant cerium accumulation in the ionomer phase of the cathode CL [36, 37].

The overall objective of the present work is to develop a comprehensive, transient *in situ* MEA model to simultaneously describe both membrane durability enhancements and performance tradeoffs in ceria-supported MEAs. For this purpose, a full MEA based numerical framework [12, 18, 36]

is adopted, which has been used previously to describe the *in situ* membrane degradation and migration effects in ceria-supported MEAs, and applied here for simulating the induced fuel cell performance tradeoffs. The developed model is further applied to investigate strategies to reduce such performance tradeoffs without compromising membrane durability. Overall, the proposed model is intended to provide a flexible modeling framework for addressing the overall MEA durability which is a combination of membrane durability and CL stability.

2 Model Formulation and Governing Equations

The present modeling framework primarily targets both durability enhancements and performance tradeoffs which are experimentally observed in ceria-supported MEAs. In our previous work [36], the reaction-transport phenomena of $\text{Ce}^{3+}/\text{Ce}^{4+}$ including the reactions between cerium ions and radicals in the membrane were integrated into an *in situ* MEA membrane degradation model [12, 18]. This baseline modeling platform was used to investigate the mitigation effectiveness of ceria additive under various cell voltages [36]. To capture the performance tradeoffs, the baseline model is extended to include proton diffusion and the principle of electroneutrality for simulating the proton concentration in the ionomer phase. The obtained proton concentration is then used to determine the proton conductivity of the ionomer and the

electrochemical reaction rates in the CLs.

The details of the governing equations used in modeling the ionomer degradation processes and the transport phenomena of the gas phase species (hydrogen, oxygen, water vapor, hydrogen peroxide and hydrogen fluoride), ionomer phase species (dissolved water, hydrogen peroxide, hydrogen fluoride, hydroxyl radical, hydrogen radical, hydroperoxyl radical, Fe^{2+} , Fe^{3+} , Ce^{3+} , and Ce^{4+}), and electrons are described in our previous publications [12, 18, 36]. In the present work, we emphasize the reaction-transport phenomena of $\text{Ce}^{3+}/\text{Ce}^{4+}$ and their influences on the membrane durability and fuel cell performance.

The key governing equation used in the model is based on conservation of species generally applied in PEFC modeling [12, 18, 36]:

$$\frac{\partial}{\partial t} (\varepsilon c_i) + \nabla \cdot J_i = S_i, \quad (1)$$

where c_i , J_i , and S_i represent the concentration, flux, and source of species i in the given phase, respectively. Since gas diffusion layers (GDLs) and CLs are porous media, the volume fraction of the given phase, ε , is introduced. Eq. (1) is assumed to be applicable in all layers in the standard MEA domain shown in Fig. 1. The MEA domain includes a membrane flanked by CLs and GDLs with separate macroporous substrates and micro-porous layer (MPL) subdomains. The dimension considered in the model is the through-plane direction (x – axis), which starts at the cathode gas channel (GC) and GDL

interface ($x = 0$) and reaches across the seven-layer MEA to the opposite, anode GC-GDL interface ($x = 7$). Three different phases are considered in the model: the gas phase and solid phase in GDLs and CLs, and the ionomer phase in CLs and membrane. The various species and transport phenomena in all MEA layers are indicated in the schematic. To simplify the simulation, all MEA layers are normalized by thickness. The MEA dimensions and other physical parameters used in the model are tabulated in Table 1.

2.1 Cerium Ion Transport

Proton (H^+), cerium ions ($\text{Ce}^{3+}/\text{Ce}^{4+}$), and iron ions ($\text{Fe}^{2+}/\text{Fe}^{3+}$) are positively charged species dissolved in the ionomer phase with fluxes governed by the Nernst-Planck equation [42, 44]:

$$J_i = -D_i \nabla c_i - u_i z_i c_i F \nabla \phi_e, \quad (2)$$

where the first term represents diffusion due to the concentration gradient and the second term represents migration due to the ionomer potential gradient across the electrolyte. Convective ion transport due to dissolved water crossover in the electrolyte is neglected. In order to solve for the six variables of interest (the five cations concentrations and the ionomer potential), electroneutrality is required:

$$\sum_i z_i c_i = c_{\text{SO}_3}, \quad (3)$$

where i includes all cations considered in the model, and c_{SO_3} represents the sulfonic acid end group concentration in the ionomer phase.

In Eq. (2), z_i denotes the charge number of species i . The self-diffusivity, D_i , and mobility, u_i , of species i are related by the Nernst-Einstein relation, *i.e.*, $D_i = u_i RT$. The ionic mobility of Ce^{3+} , Ce^{4+} , Fe^{2+} , and Fe^{3+} is assumed to be 10^{-14} [36], 10^{-15} [36], 1.25×10^{-13} [12], and 1.83×10^{-14} [38] s mol kg⁻¹, respectively.

The proton mobility is related with the proton conductivity by $\sigma_{\text{H}^+} = u_{\text{H}^+} c_{\text{H}^+} z_{\text{H}^+}^2 F^2$, where the proton conductivity is calculated by using the binary friction membrane model (BFM2) [45, 46]. Readers are referred to the previous publication [18] for the variables used in BFM2.

The hydrogen oxidation reaction (HOR) and four-electron ORR are the regular electrochemical reactions occurring in the anode and cathode, respectively, and their reaction rates can be described by the Butler-Volmer kinetics [44, 47]:

$$r_{\text{HOR}} = ai_{\text{HOR},0} \frac{c_{\text{H}^+}}{c_{\text{H}^+,0}} \frac{c_{\text{H}_2,\text{G}}}{c_{\text{H}_2,\text{ref}}} \left[\exp\left(\frac{F\eta_{\text{HOR}}}{2RT}\right) - \exp\left(-\frac{F\eta_{\text{HOR}}}{2RT}\right) \right], \quad (4)$$

$$r_{4e} = ai_{4e,0} \frac{c_{\text{H}^+}}{c_{\text{H}^+,0}} \frac{c_{\text{O}_2,\text{G}}}{c_{\text{O}_2,\text{ref}}} \left[\exp\left(\frac{F\eta_{4e}}{RT}\right) - \exp\left(-\frac{F\eta_{4e}}{RT}\right) \right], \quad (5)$$

where a is the volumetric specific surface area of the electrode, i_0 is the exchange current density, and c_{H^+} is the proton concentration with reference value denoted by $c_{\text{H}^+,0}$. The factor, $c_{\text{H}^+}/c_{\text{H}^+,0}$, is introduced to account for the activation loss related to the proton starvation in the CLs [43, 44]. The

overpotential, η_i , is calculated by:

$$\eta_i = \phi_s - \phi_e - E_{i,\text{eq}}, \quad (6)$$

in which ϕ_s is the local electrode potential, ϕ_e is the local ionomer potential across the electrolyte, and $E_{i,\text{eq}}$ is the equilibrium potential for the given electrochemical reaction. The parameters used in calculating the HOR and four-electron ORR are tabulated in Table 2.

The cerium ions can initially be assumed to be evenly distributed throughout the ionomer phase of the MEA, since ceria migration from the CLs to the membrane has been observed after fuel cell conditioning [27, 29]. Moreover, the dissolved Ce^{4+} is electrochemically reduced to Ce^{3+} at both anode and cathode by hydrogen and water due to the high electrochemical potential of the $\text{Ce}^{3+}/\text{Ce}^{4+}$ couple [22, 36]. It is therefore assumed that cerium exists solely in the Ce^{3+} form in the membrane at the beginning of the simulation:

$$c_{\text{Ce}^{3+},0} = 100 \text{ mol m}^{-3} \quad (7)$$

$$c_{\text{Ce}^{4+},0} = 0. \quad (8)$$

The initial cerium ion concentration is equivalent to $0.3 \mu \text{ mol Ce cm}^{-2}$ or $\sim 0.9 \text{ wt\%}$ loading [37]. Cerium washout from the MEA is neglected, and therefore zero fluxes are assumed at the CL and MPL interfaces.

3 Results and Discussion

The proposed MEA model is first applied to simulate the performance tradeoffs in ceria-supported MEAs with different ionomer loadings in the cathode CL at the beginning of life (BOL) [37], followed by a detailed analysis on the mechanisms that cause the tradeoffs. Then, a brief section is given to discuss the overall MEA durability by means of simulating both membrane durability and fuel cell performance in ceria-supported MEA.

3.1 BOL MEA Performance

The BOL fuel cell polarization curves with and without ceria additives are simulated and plotted in Fig. 2 for two different ionomer loadings. Lower fuel cell performance in ceria-supported MEA is found from 0.9 V to 0.6 V, which represents the usual operating cell voltages in fuel cell applications in which kinetic and ohmic losses are dominant. The performance tradeoff due to the ceria additive can be represented by a voltage loss defined as the cell voltage difference between the baseline (without ceria additive) and ceria-supported MEAs at the same current density. The simulated voltage loss is compared to the experimental results [37] in Fig. 3. The simulated result successfully predicts the magnitude of the voltage loss within a few millivolts and captures the increasing trend of the voltage loss with operating current density. The results confirm that the ceria additive has negative impact on fuel cell performance, and that the impact becomes more severe at higher

current densities.

In hydrogen PEFCs, the local potentials at anode and cathode CLs are negative of the standard electrochemical potential of the $\text{Ce}^{3+}/\text{Ce}^{4+}$ redox couple (*i.e.*, 1.44 V [32]). The Ce^{4+} ions can therefore be electrochemically reduced in the anode and cathode CLs by hydrogen and water, respectively [22]. Ce^{4+} can also be reduced to Ce^{3+} by hydrogen peroxide which is continuously generated in the MEA via the two-electron ORR [36]. As a result, Ce^{3+} is the dominant oxidation state in the MEA, and almost zero Ce^{4+} concentration is obtained. This outcome with the vast majority of the cerium ions are in the desired Ce^{3+} oxidation state is one of the conditions for efficient membrane protection in ceria-supported MEAs [32, 36]. Moreover, the average concentrations of cation contaminants in the membrane such as Fe^{2+} and Fe^{3+} ($\sim 1 \text{ mol m}^{-3}$) is two orders of magnitude lower than the Ce^{3+} concentration ($\sim 100 \text{ mol m}^{-3}$). Therefore, Ce^{3+} is the main charged species susceptible to exchange the protons attached to the sulfonic acid end groups in ceria-supported MEAs.

When the cell voltage is held below OCV (the simulated OCV is ~ 1.0 V), an ionomer potential gradient across the cathode CL, membrane, and anode CL is formed due to the regular electrochemical reactions in hydrogen PEFCs. As illustrated in Fig. 4, the obtained ionomer potential decreases from the anode CL to the cathode CL which results in migration of positively charged species, including protons, $\text{Ce}^{3+}/\text{Ce}^{4+}$ ions, and $\text{Fe}^{2+}/\text{Fe}^{3+}$ ions, from the anode CL to the cathode CL across the membrane. Since

transport of Ce^{3+} ions across the MPL-CL interfaces is neglected, Ce^{3+} is accumulated at the cathode CL as revealed in Fig. 5. As the cell voltage decreases, *e.g.*, from 0.8 V to 0.6 V, the ion migration becomes more dominant because the ionomer potential gradient increases due to the enhanced HOR and four-electron ORR. The simulated Ce^{3+} accumulation at the cathode CL consequently becomes more severe at lower cell voltages, as illustrated in Fig. 5. Due to the electroneutrality condition, *i.e.*, $c_{\text{H}^+} + 3c_{\text{Ce}^{3+}} \simeq c_{\text{SO}_3}$, the increase in Ce^{3+} concentration results in a three times more significant reduction in proton concentration ($\Delta c_{\text{H}^+} \simeq -3\Delta c_{\text{Ce}^{3+}}$). Hence, a notable reduction in local proton concentration is observed in the cathode CL when the Ce^{3+} concentration is high, as in the case of 0.6 V shown in Fig. 5.

The proton starvation leads to low four-electron ORR rate and low proton conductivity in the cathode CL which results in sizable kinetic and ohmic performance losses for the ceria-supported MEA. In the baseline MEA, higher water content is obtained in cathode CL due to the water formation and the electro-osmotic drag. Hence, the simulated proton conductivity in the ionomer phase decreases from the cathode CL to the anode CL, as shown in Fig. 6. On the other hand, the high water content cannot sustain the proton conductivity in the cathode CL when ceria additive is present in the MEA. In general for the ceria-supported MEAs, the obtained proton conductivity in the cathode CL is lower than in the anode CL and membrane, as indicated in Fig. 6, which is also supported by the high cathode CL ionic resistance measured experimentally [37]. The low conductivity is attributed

to the low proton concentration because of the Ce^{3+} accumulation, since the proton conductivity is proportional to the proton concentration according to the Nernst-Planck equation [44]. As the cell voltage is decreased from 0.8 to 0.6 V, the decay in proton concentration counteracts the increase in water content, leading to a reduction in proton conductivity. Therefore, the proton conductivity at the MPL-CL interface decreases from 5.5 to 0.22 S m^{-1} when the cell voltage is reduced (*cf.*, Fig. 6). The poor proton conductivity results in an additional ohmic resistance in the ceria-supported MEA, and the corresponding ohmic loss is increased with current density.

The rate of the four-electron ORR is not uniform across the cathode CL. As illustrated in Fig. 7, the peak ORR rate is obtained near the CL-membrane interface in the baseline MEA. The higher ORR rate is due to the more negative overpotential, $\phi_s - \phi_e - E_{4e,eq}$, because of the more positive ionomer potential near the CL-membrane interface, as shown in Fig. 4. When the ceria additive is introduced into the MEA, the ORR rate becomes more uneven (Fig. 7). The lack of protons near the cathode CL-MPL interface hinders the ORR rate because the proton, which is required for the four-electron ORR, is absent in the ionomer phase even though the oxygen concentration and overpotential are comparable to the baseline MEA. In order to generate the same current density as for the baseline MEA, a lower cathode potential, ϕ_s , is required to achieve a more negative overpotential to compensate for the effect of proton starvation. This is the source of the kinetic loss that contributes to the performance tradeoff.

The magnitude of the kinetic loss due to proton starvation can be estimated from the Nernst equation, *i.e.*, $\Delta\phi_s \approx RT/F\Delta \ln c_p$ [43]. The strong positive correlation between the proton concentration and ORR rate implies that the ORR rate profile across the cathode CL is similar to the distribution of protons, although the profile is further compounded by the increase in ionomer potential.

3.2 Membrane Durability and Fuel Cell Performance

The voltage losses predicted for ceria-supported MEAs are expected to counteract the durability benefits and may possibly even outweigh the motivation for the use of radical scavengers unless care is taken to analyze the interactions between membrane stability and MEA performance. The MEA performance decay due to the presence of ceria additive is mainly attributed to the cerium accumulation in the cathode CL under nonzero current densities. This accumulation could potentially be mitigated by increasing the ionomer loading in the CL or decreasing the ceria additive loading in the MEA. In this section, the effects of the ionomer and ceria additive loadings on the performance and durability combination are therefore addressed.

In general, the simulated results in Figs. 3 and 8 indicate that the negative performance impact can be partially mitigated when the ionomer loading is increased or the ceria additive amount is decreased in the BOL MEA. The obtained improvements are attributed to the reduction in local Ce^{3+} concentration in the cathode CL shown in Fig. 9. When the initial Ce^{3+} loading is

reduced from 100 to 25 mol m⁻³, it is clear that the Ce³⁺ accumulation is also reduced. The corresponding proton conductivity in the ionomer phase of the cathode CL illustrated in Fig. 10 is increased when the initial cerium ion concentration is reduced from 100 to 25 mol m⁻³. The reduction in Ce³⁺ concentration also increases the ORR rate in the cathode CL, as shown in Fig. 11, which leads to a reduction in the kinetic voltage loss.

An increase in the ionomer loading of the cathode CL is expected to have a similar effect as the proposed reduction in initial Ce³⁺ loading which reduces the Ce³⁺ accumulation in the cathode CL because higher ionomer loading can store more cerium ions such that the local concentration is diluted. Hence, as illustrated in Fig. 10, the simulated proton conductivity of the cathode CL increases with increasing ionomer volume fraction. As the effective proton conductivity in the cathode CL is calculated using the Bruggeman approximation [33], the ohmic loss due to ionomer resistance in the elevated ionomer loading MEA is further reduced. Moreover, with less cerium ion interference at the cathode, the kinetic voltage loss associated with the ORR is also reduced (Fig. 11).

The initial Ce³⁺ concentration and ionomer loading could be optimized to mitigate the performance decay observed in the ceria-supported MEAs. For the optimization of the initial Ce³⁺ concentration, the most critical concern is the mitigation effectiveness of the chemical membrane degradation which may otherwise cause lifetime-limiting hydrogen leaks across the membrane [27]. The cumulative fluoride loss is therefore simulated as a func-

tion of initial Ce^{3+} concentration under accelerated conditions for chemical membrane degradation at OCV [27]. As expected, the results provided in Fig. 12(a) demonstrate that the fluoride release rate increases with decreasing Ce^{3+} concentration. Fortunately, the fluoride release is less sensitive at higher concentrations which was also observed with ceria-supported MEAs subjected to the *ex situ* Fenton's durability test [23]. For example, when the initial concentration decreases from 50 mol m^{-3} to 25 mol m^{-3} , the total fluoride loss increases by 0.29 mol m^{-2} which is almost 10x higher than the increase of fluoride loss when the concentration decreases from 100 mol m^{-3} to 75 mol m^{-3} . This property of the ceria additive makes it feasible to reduce the additive loading while still achieving a desirable mitigation of chemical membrane degradation. For instance, approximately 40x reduction in the fluoride emission rate can be achieved with a mere initial Ce^{3+} concentration of 50 mol m^{-3} .

As a potential power source, however, fuel cells are normally operated below OCV to provide power during duty operation. The mitigation effectiveness is therefore more important under realistic operating conditions than for idle OCV conditions. The cumulative fluoride release of MEAs with various initial cerium ion loadings is hence simulated at 0.8 V, with results shown in Fig. 12(b). In general, the fluoride release is less sensitive to the initial Ce^{3+} concentration when compared to the OCV condition. This suggests that the performance tradeoff can be minimized without compromising membrane durability by reducing the initial Ce^{3+} concentration from 100 to 50

mol m⁻³, which was also observed to be acceptable under the more stressful OCV condition. On the other hand, the durability mitigation effectiveness of ceria is slightly reduced at 0.8 V compared with the effectiveness simulated at OCV. The reduction in effectiveness is related with the cerium ion accumulation in the cathode CL which results in a lower Ce³⁺ concentration in the membrane that reduces the ·OH quenching rate, as discussed in our previous publication [36]. Moreover, the proton starvation near the cathode CL-MPL interface reduces the local ORR rate, and consequently reduces the local ionomer potential gradient, as illustrated in Fig. 13. Therefore, the ion migration of harmful Fe²⁺ toward the cathode CL is also reduced, which results in a higher remaining Fe²⁺ concentration in the membrane. This effect is depicted in Fig. 14(a), indicating that the addition of 100 mol m⁻³ ceria can effectively double the iron ion concentration in the membrane under these conditions.

When the cell voltage is further reduced to 0.6 V, the cerium ion accumulation at the cathode CL becomes more significant due to the enhanced ORR in which the current densities increased from ~0.23 A cm⁻² at 0.8 V to 0.85-1.0 A cm⁻² at 0.6 V under the present conditions. This effect magnifies the influence of the ceria loading on the ionomer potential gradient (Fig.13) and the Fe²⁺ concentration in the membrane (Fig.14(b)). The ceria induced increase in Fe²⁺ concentration in the membrane is notable, in contrast to the baseline MEA without ceria which had essentially zero iron ion concentration in the membrane at this cell voltage. As shown in Fig. 15, this alters the

chemical membrane degradation rates quantified by the simulated fluoride release, even to the extent where a ceria-supported MEA may have a *higher* degradation rate than the ceria-free baseline MEA. At this cell voltage, the baseline MEA is therefore deemed to have the best overall durability and performance combination since it has a membrane durability equivalent to the MEA with 50 mol m^{-3} ceria without the associated performance tradeoffs.

Overall, the simulated results demonstrate that an optimized ceria loading can successfully provide MEA durability management at high cell voltages in terms of enhanced membrane durability and MEA performance stability. However, this approach becomes more convoluted at low cell voltages. The role of the cathode CL is more critical at low cell voltages because of cerium ion accumulation which suggests that both performance and durability issues should be addressed simultaneously in the engineering design of the cathode CL. Based on the present simulation results, joint optimization of the ionomer volume fraction in the cathode CL and the ceria additive loading could be feasible in order to enhance the overall MEA durability across the entire range of cell voltages.

4 Conclusions

The performance tradeoff observed in ceria-supported MEAs in hydrogen PEFCs is investigated using a comprehensive, transient MEA durability model. The cathode catalyst layer of ceria-supported MEAs is found to experience

proton starvation due to cerium ion migration across the membrane. The inadequate supply of protons in the ionomer phase of the cathode CL reduces the proton conductivity as well as the oxygen reduction reaction kinetics, which contributes to the performance tradeoff in terms of ohmic and kinetic voltage losses. Increased ionomer volume fraction in the cathode CL and reduced Ce^{3+} concentration in the MEA are found to be effective strategies to reduce the performance tradeoffs in ceria stabilized MEAs. Overall durability management is shown to be possible at high cell voltages by optimizing the ceria loading in the MEA such as reduction of Ce^{3+} concentration from 100 to 50 mol m^{-3} ; however, at low cell voltages additional steps must be taken to achieve a useful combination of membrane durability and cathode CL performance stability in order to address proton starvation in the cathode CL without compromising membrane durability. The role of the cathode CL becomes more important for the overall MEA durability at low cell voltages, which suggests that the membrane durability and CL performance stability ought to be jointly addressed by optimization of the MEA design.

Acknowledgements

This research was supported by Ballard Power Systems and the Natural Sciences and Engineering Research Council of Canada through an Automotive Partnership Canada (APC) grant. We thank our colleagues at SFU FCReL and Ballard for their valuable comments and advice.

References

- [1] M. P. Rodgers, L. J. Bonville, H. R. Kunz, D. K. Slattery, and J. M. Fenton. Fuel cell perfluorinated sulfonic acid membrane degradation correlating accelerated stress testing and lifetime. *Chem. Rev.*, 112(11):6075–6103, 2012.
- [2] C.S. Gittleman, F.D. Coms, and Y.-H. Lai. Chapter 2 - membrane durability: Physical and chemical degradation. In M. Mench, E. C. Kumbur, and T. N. Veziroglu, editors, *Polymer Electrolyte Fuel Cell Degradation*, pages 15 – 88. Academic Press, Boston, 2012.
- [3] C. Lim, L. Ghassemzadeh, F. Van Hove, M. Lauritzen, J. Kolodziej, G. G. Wang, S. Holdcroft, and E. Kjeang. Membrane degradation during combined chemical and mechanical accelerated stress testing of polymer electrolyte fuel cells. *J. Power Sources*, 257(0):102 – 110, 2014.
- [4] N. Macauley, A. Alavijeh Sadeghi, M. Watson, J. Kolodziej, M. Lauritzen, S. Knights, G. G. Wang, and E. Kjeang. Accelerated membrane durability testing of heavy duty fuel cells. *J. Electrochem. Soc.*, 162(1):F98–F107, 2015.
- [5] M.-A. Goulet, S. Arbour, M. Lauritzen, and E. Kjeang. Water sorption and expansion of an ionomer membrane constrained by fuel cell electrodes. *J. Power Sources*, 274(0):94 – 100, 2015.

- [6] R. M. H. Khorasany, E. Kjeang, G. G. Wang, and R. K. N. D. Rajapakse. Simulation of ionomer membrane fatigue under mechanical and hygrothermal loading conditions. *J. Power Sources*, 279(0):55 – 63, 2015.
- [7] R. M. H. Khorasany, A. Sadeghi Alavijeh, E. Kjeang, G. G. Wang, and R. K. N. D. Rajapakse. Mechanical degradation of fuel cell membranes under fatigue fracture tests. *J. Power Sources*, 274(0):1208 – 1216, 2015.
- [8] M.-A. Goulet, R. M. H. Khorasany, C. De Torres, M. Lauritzen, E. Kjeang, G. G. Wang, and N. Rajapakse. Mechanical properties of catalyst coated membranes for fuel cells. *J. Power Sources*, 234(0):38 – 47, 2013.
- [9] A. Sadeghi Alavijeh, M.-A. Goulet, R. M. H. Khorasany, J. Ghataurah, C. Lim, M. Lauritzen, E. Kjeang, G. G. Wang, and R. K. N. D. Rajapakse. Decay in mechanical properties of catalyst coated membranes subjected to combined chemical and mechanical membrane degradation. *Fuel Cells*, 15(1):204–213, 2015.
- [10] A. B. LaConti, M. Hamdan, and R. C. McDonald. *Mechanisms of membrane degradation. Handbook of Fuel Cells*. John Wiley & Sons, Ltd, 2003.

- [11] M. Inaba, T. Kinumoto, M. Kiriake, R. Umebayashi, A. Tasaka, and Z. Ogumi. Gas crossover and membrane degradation in polymer electrolyte fuel cells. *Electrochim. Acta*, 51(26):5746–5753, 2006.
- [12] K.H. Wong and E. Kjeang. Mitigation of chemical membrane degradation in fuel cells: Understanding the effect of cell voltage and iron ion redox cycle. *ChemSusChem*, 8(6):1072–1082, 2015.
- [13] E. Endoh, S. Terazono, H. Widjaja, and Y. Takimoto. Degradation study of mea for pemfcs under low humidity conditions. *Electrochem. Solid-State Lett.*, 7(7):A209–A211, 2004.
- [14] J. Healy, C. Hayden, T. Xie, K. Olson, R. Waldo, M. Brundage, H. Gasteiger, and J. Abbott. Aspects of the chemical degradation of pfsa ionomers used in pem fuel cells. *Fuel Cells*, 5(2):302–308, 2005.
- [15] L. Gubler, S. M. Dockheer, and W. H. Koppenol. Radical HO \cdot , H \cdot and HOO \cdot formation and ionomer degradation in polymer electrolyte fuel cells. *J. Electrochem. Soc.*, 158(7):B755–B769, 2011.
- [16] L. Ghassemzadeh and S. Holdcroft. Quantifying the structural changes of perfluorosulfonated acid ionomer upon reaction with hydroxyl radicals. *J. Am. Chem. Soc.*, 135(22):8181–8184, 2013.
- [17] L. Ghassemzadeh, T. J. Peckham, T. Weissbach, X. Luo, and S. Holdcroft. Selective formation of hydrogen and hydroxyl radicals by elec-

- tron beam irradiation and their reactivity with perfluorosulfonated acid ionomer. *J. Am. Chem. Soc.*, 135(42):15923–15932, 2013.
- [18] K.H. Wong and E. Kjeang. Macroscopic in-situ modeling of chemical membrane degradation in polymer electrolyte fuel cells. *J. Electrochem. Soc.*, 161(9):F823–F832, 2014.
- [19] M. Ghelichi, P.-. A. Melchy, and M. H. Eikerling. Radically coarse-grained approach to the modeling of chemical degradation in fuel cell ionomers. *J. Phys. Chem. B*, 118(38):11375–11386, 2014.
- [20] P.-É. A. Melchy and M. H. Eikerling. Physical theory of ionomer aggregation in water. *Phys. Rev. E*, 89:032603, 2014.
- [21] P. Trogadas, J. Parrondo, and V. Ramani. Degradation mitigation in polymer electrolyte membranes using cerium oxide as a regenerative free-radical scavenger. *Electrochem. Solid-State Lett.*, 11(7):B113–B116, 2008.
- [22] F. D. Coms, H. Liu, and J. E. Owejan. Mitigation of perfluorosulfonic acid membrane chemical degradation using cerium and manganese ions. *ECS Trans.*, 16(2):1735–1747, 2008.
- [23] Z. Wang, H. Tang, H. Zhang, M. Lei, R. Chen, P. Xiao, and M. Pan. Synthesis of nafion/ceo2 hybrid for chemically durable proton exchange membrane of fuel cell. *J. Membrane Sci.*, 421422(0):201 – 210, 2012.

- [24] B.P. Pearman, N. Mohajeri, R. P. Brooker, M. P. Rodgers, D. K. Slattery, M. D. Hampton, D. A. Cullen, and S. Seal. The degradation mitigation effect of cerium oxide in polymer electrolyte membranes in extended fuel cell durability tests. *J. Power Sources*, 225(0):75 – 83, 2013.
- [25] B. P. Pearman, N. Mohajeri, D. K. Slattery, M. D. Hampton, S. Seal, and D. A. Cullen. The chemical behavior and degradation mitigation effect of cerium oxide nanoparticles in perfluorosulfonic acid polymer electrolyte membranes. *Polym. Degrad. Stabil.*, 98(9):1766 – 1772, 2013.
- [26] L. Wang, S. G. Advani, and A. K. Prasad. Degradation reduction of polymer electrolyte membranes using ceo2 as a free-radical scavenger in catalyst layer. *Electrochimica Acta*, 109(0):775 – 780, 2013.
- [27] C. Lim, A. Sadeghi Alavijeh, M. Lauritzen, J. Kolodziej, S. Knights, and E. Kjeang. Fuel cell durability enhancement with cerium oxide under combined chemical and mechanical membrane degradation. *ECS Electrochem. Lett.*, 4(4):F29–F31, 2015.
- [28] S. A. Hayes, P. Yu, T. J. O’Keefe, M. J. O’Keefe, and J. O. Stoffer. The phase stability of cerium species in aqueous systems: I. e-ph diagram for the $\text{CeHClO}_4\text{H}_2\text{O}$ system. *J. Electrochem. Soc.*, 149(12):C623–C630, 2002.

- [29] S. M. Stewart, D. Spornjak, R. Borup, A. Datye, and F. Garzon. Cerium migration through hydrogen fuel cells during accelerated stress testing. *ECS Electrochem. Lett.*, 3(4):F19–F22, 2014.
- [30] D. Banham, S. Ye, T. Cheng, S. Knights, S. M. Stewart, M. Wilson, and F. Garzon. Effect of ceox crystallite size on the chemical stability of ceox nanoparticles. *J. Electrochem. Soc.*, 161(10):F1075–F1080, 2014.
- [31] T. Xie and C. A. Hayden. A kinetic model for the chemical degradation of perfluorinated sulfonic acid ionomers: Weak end groups versus side chain cleavage. *Polymer*, 48(19):5497–5506, 2007.
- [32] L. Gubler and W. H. Koppenol. Kinetic simulation of the chemical stabilization mechanism in fuel cell membranes using cerium and manganese redox couples. *J. Electrochem. Soc.*, 159(2):B211–B218, 2011.
- [33] A. A. Shah, T. R. Ralph, and F. C. Walsh. Modeling and simulation of the degradation of perfluorinated ion-exchange membranes in pem fuel cells. *J. Electrochem. Soc.*, 156(4):B465–B484, 2009.
- [34] R. Coulon, W. Bessler, and A. A. Franco. Modeling chemical degradation of a polymer electrolyte membrane and its impact on fuel cell performance. *ECS Trans.*, 25(35):259–273, 2010.
- [35] M. Gummalla, V. V. Atrazhev, D. Condit, N. Cipollini, T. Madden, N. Y. Kuzminyh, D. Weiss, and S. F. Burlatsky. Degradation of polymer-

- electrolyte membranes in fuel cells: Ii. theoretical model. *J. Electrochem. Soc.*, 157(11):B1542–B1548, 2010.
- [36] K.H. Wong and E. Kjeang. In situ modeling of chemical membrane degradation and mitigation in ceria-supported fuel cells. *Submitted*, 2015.
- [37] T. T. H. Cheng, S. Wessel, and S. Knights. Interactive effects of membrane additives on pemfc catalyst layer degradation. *J. Electrochem. Soc.*, 160(1):F27–F33, 2013.
- [38] T. Okada, Y. Ayato, M. Yuasa, and I. Sekine. The effect of impurity cations on the transport characteristics of perfluorosulfonated ionomer membranes. *J. Phys. Chem. B*, 103(17):3315–3322, 1999.
- [39] T. Okada, H. Satou, and M. Yuasa. Effects of additives on oxygen reduction kinetics at the interface between platinum and perfluorinated ionomer. *Langmuir*, 19(6):2325–2332, 2003.
- [40] B. Kienitz, B. Pivovar, T. Zawodzinski, and F. H. Garzon. Cationic contamination effects on polymer electrolyte membrane fuel cell performance. *J. Electrochem. Soc.*, 158(9):B1175–B1183, 2011.
- [41] B.L. Kienitz, H. Baskaran, and T.A. Zawodzinski Jr. Modeling the steady-state effects of cationic contamination on polymer electrolyte membranes. *Electrochim. Acta*, 54(6):1671 – 1679, 2009.

- [42] A. Z. Weber and C. Delacourt. Mathematical modelling of cation contamination in a proton-exchange membrane. *Fuel Cells*, 8(6):459–465, 2008.
- [43] T. A. Greszler, T. E. Moylan, and H. A. Gasteiger. *Modeling the impact of cation contamination in a polymer electrolyte membrane fuel cell*, chapter 49. John Wiley and Sons, Ltd, 2010.
- [44] M. F. Serincan, U. Pasaogullari, and T. Molter. Modeling the cation transport in an operating polymer electrolyte fuel cell (pefc). *Int. J. Hydrogen Energy*, 35(11):5539 – 5551, 2010.
- [45] J. Fimrite, B. Carnes, H. Struchtrup, and N. Djilali. Transport phenomena in polymer electrolyte membranes: Ii. binary friction membrane model. *J. Electrochem. Soc.*, 152(9):A1815–A1823, 2005.
- [46] B. Carnes and N. Djilali. Analysis of coupled proton and water transport in a pem fuel cell using the binary friction membrane model. *Electrochim. Acta*, 52(3):1038–1052, 2006.
- [47] C. Siegel. Review of computational heat and mass transfer modeling in polymer-electrolyte-membrane (pem) fuel cells. *Energy*, 33(9):1331 – 1352, 2008.
- [48] C. Chan, N. Zamel, X. Li, and J. Shen. Experimental measurement of effective diffusion coefficient of gas diffusion layer/microporous layer in pem fuel cells. *Electrochim. Acta*, 65(0):13–21, 2012.

- [49] J. Shen, J. Zhou, N. G. C. Astrath, T. Navessin, Z.-S. Liu, C. Lei, J. H. Rohling, D. Bessarabov, S. Knights, and S. Ye. Measurement of effective gas diffusion coefficients of catalyst layers of pem fuel cells with a loschmidt diffusion cell. *J. Power Sources*, 196(2):674–678, 2011.

List of Figures

1	Schematic of the computational domain, including membrane, catalyst layers (CLs), and gas diffusion layers (GDLs; consisting of a macroporous substrate and a microporous layer). Chemical degradation is considered in the membrane. Gas and electron transport is considered in the GDLs and CLs, and transport in the ionomer phase is considered in the CLs and membrane.	35
2	Simulated fuel cell polarization curves with and without ceria additive for two different cathode ionomer volume fractions: (a) 27% and (b) 20%.	36
3	Simulated and measured voltage losses due to ceria additive as a function of current density.	37
4	Simulated ionomer potential across the cathode CL ($2 < x < 3$), membrane ($3 < x < 4$), and anode CL ($4 < x < 5$) for baseline and ceria-supported MEAs.	38
5	Simulated cerium(III) ion and proton concentrations in the ionomer phase across the cathode CL ($2 < x < 3$), membrane ($3 < x < 4$), and anode CL ($4 < x < 5$) for ceria-supported MEAs.	39

6	Simulated proton conductivity in the ionomer phase across the cathode CL ($2 < x < 3$), membrane ($3 < x < 4$), and anode CL ($4 < x < 5$) baseline and ceria-supported MEAs.	40
7	Simulated four-electron ORR rate in the cathode CL for baseline and ceria-supported MEAs.	41
8	Simulated voltage losses of ceria-supported MEAs under reference ($c_{\text{Ce}^{3+}} = 100 \text{ mol m}^{-3}$), and reduced cerium ion concentration ($c_{\text{Ce}^{3+}} = 75, 50$ and 25 mol m^{-3}) conditions.	42
9	Simulated Ce^{3+} concentrations in the ionomer phase at 0.6 V under reference ($c_{\text{Ce}^{3+}} = 100 \text{ mol m}^{-3}$ and $\varepsilon_e = 0.27$), reduced ionomer volume fraction ($\varepsilon_e = 0.2$), and reduced cerium ion concentration ($c_{\text{Ce}^{3+}} = 75, 50$ and 25 mol m^{-3}) conditions.	43
10	Simulated proton conductivities in the ionomer phase at 0.6 V under reference ($c_{\text{Ce}^{3+}} = 100 \text{ mol m}^{-3}$ and $\varepsilon_e = 0.27$), reduced ionomer volume fraction ($\varepsilon_e = 0.2$), and reduced cerium ion concentration ($c_{\text{Ce}^{3+}} = 75, 50$ and 25 mol m^{-3}) conditions.	44
11	Simulated ORR rate in the cathode CL at 0.6 V under reference ($c_{\text{Ce}^{3+}} = 100 \text{ mol m}^{-3}$ and $\varepsilon_e = 0.27$), reduced ionomer volume fraction ($\varepsilon_e = 0.2$), and reduced cerium ion concentration ($c_{\text{Ce}^{3+}} = 75, 50$ and 25 mol m^{-3}) conditions.	45
12	Simulated cumulative fluoride release as a function of the initial Ce^{3+} concentrations in the membrane at (a) OCV and (b) 0.8 V.	46

13	Simulated ionomer potential under reference ($c_{\text{Ce}^{3+}} = 100 \text{ mol m}^{-3}$) and reduced initial cerium ion concentration ($c_{\text{Ce}^{3+}} = 75, 50 \text{ and } 25 \text{ mol m}^{-3}$) conditions.	47
14	Simulated iron(II) concentration in the ionomer phase of the cathode CL at (a) 0.8 V and (b) 0.6 V under reference ($c_{\text{Ce}^{3+}} =$ 100 mol m^{-3}) and reduced initial cerium ion concentration ($c_{\text{Ce}^{3+}} = 75, 50 \text{ and } 25 \text{ mol m}^{-3}$) conditions.	48
15	Simulated cumulative fluoride release as a function of the ini- tial Ce^{3+} concentration in the membrane during fuel cell op- eration at a constant cell voltage of 0.6 V.	49

List of Tables

1	Structural and physical parameters used in the model.	50
2	Parameters associated with calculation of reaction kinetics . . .	51

Figures

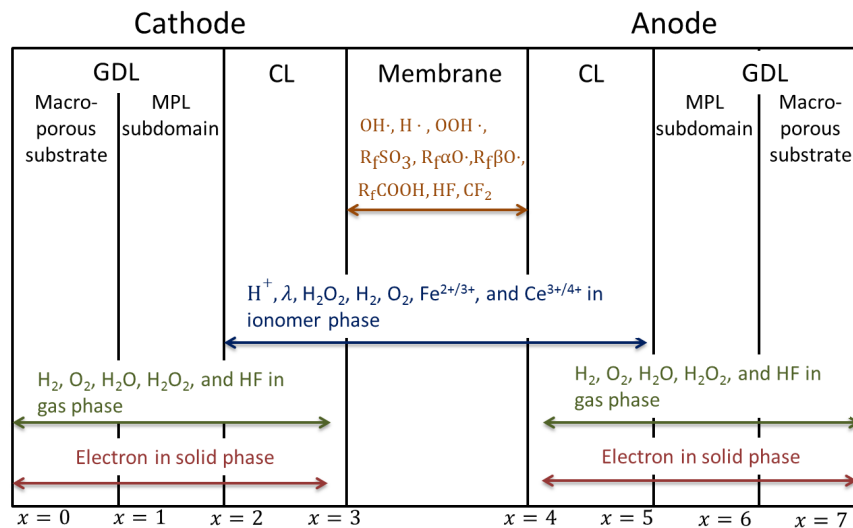


Figure 1: Schematic of the computational domain, including membrane, catalyst layers (CLs), and gas diffusion layers (GDLs; consisting of a macroporous substrate and a microporous layer). Chemical degradation is considered in the membrane. Gas and electron transport is considered in the GDLs and CLs, and transport in the ionomer phase is considered in the CLs and membrane.

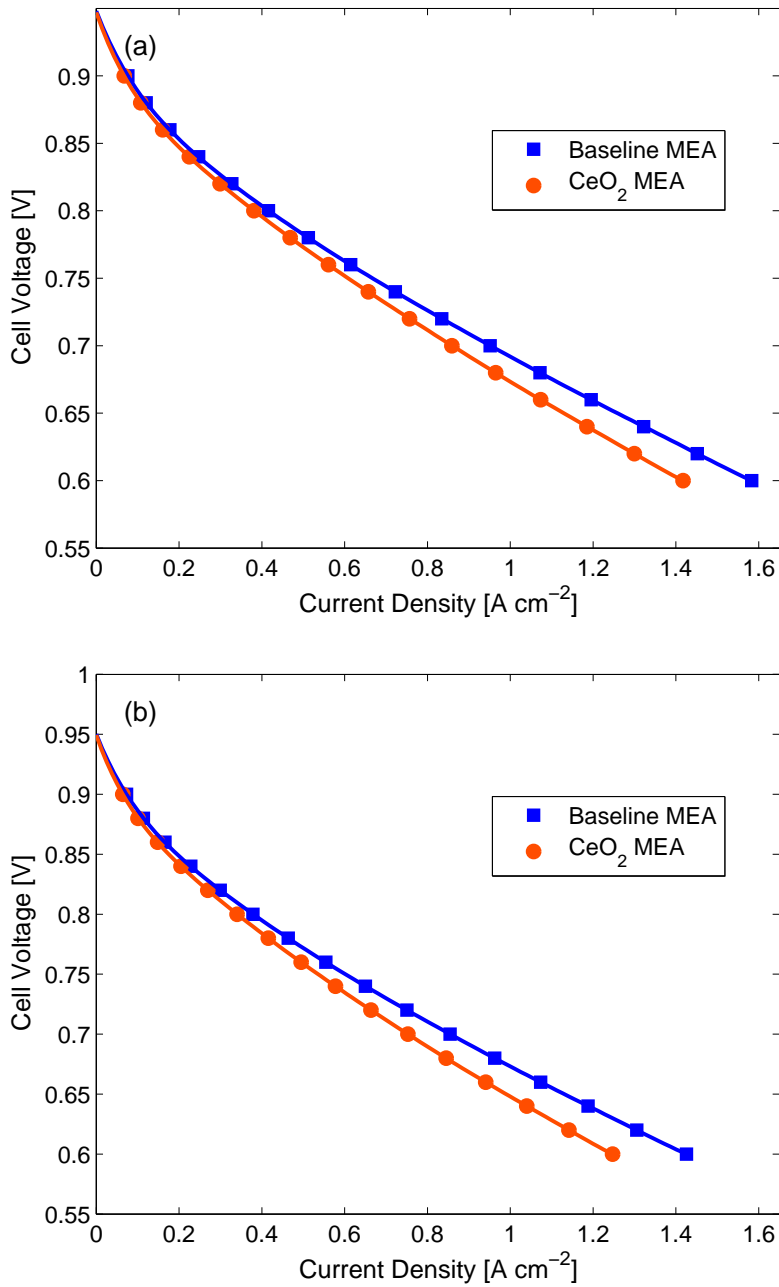


Figure 2: Simulated fuel cell polarization curves with and without ceria additive for two different cathode ionomer volume fractions: (a) 27% and (b) 20%.

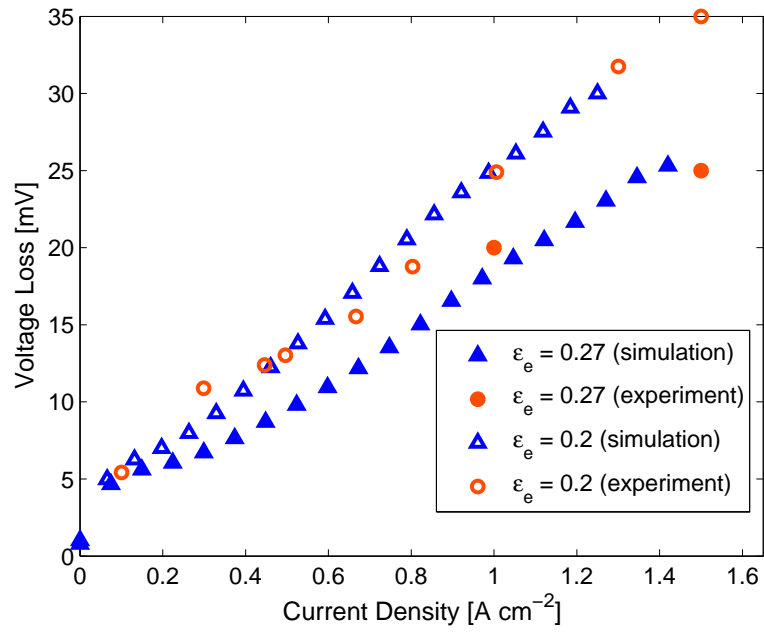


Figure 3: Simulated and measured voltage losses due to ceria additive as a function of current density.

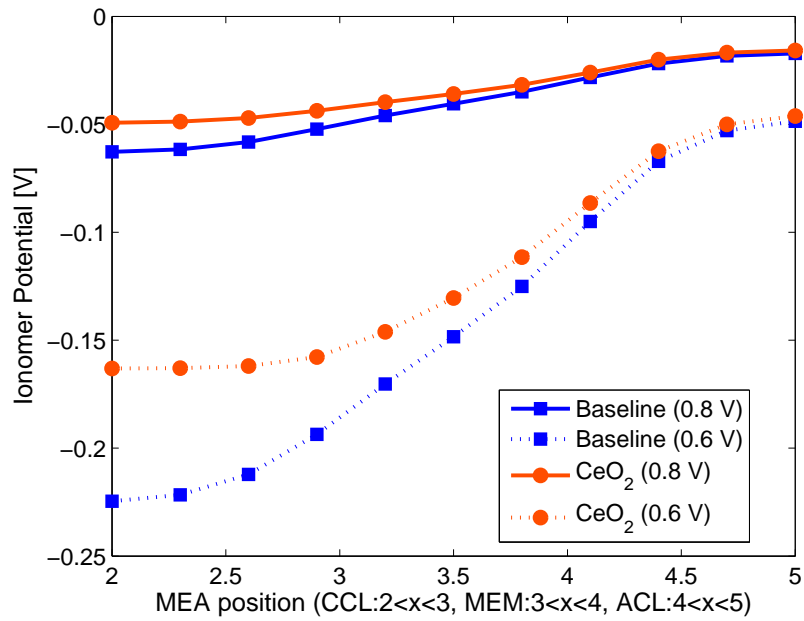


Figure 4: Simulated ionomer potential across the cathode CL ($2 < x < 3$), membrane ($3 < x < 4$), and anode CL ($4 < x < 5$) for baseline and ceria-supported MEAs.

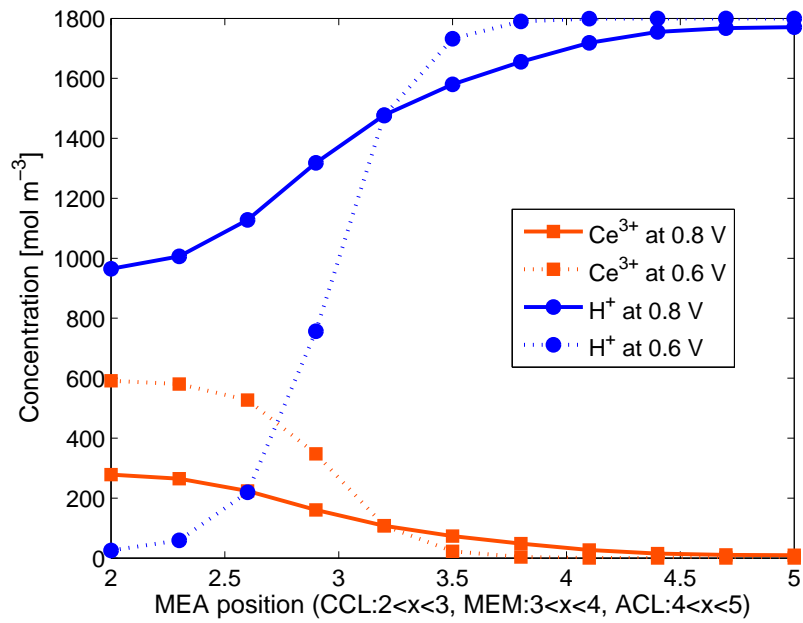


Figure 5: Simulated cerium(III) ion and proton concentrations in the ionomer phase across the cathode CL ($2 < x < 3$), membrane ($3 < x < 4$), and anode CL ($4 < x < 5$) for ceria-supported MEAs.

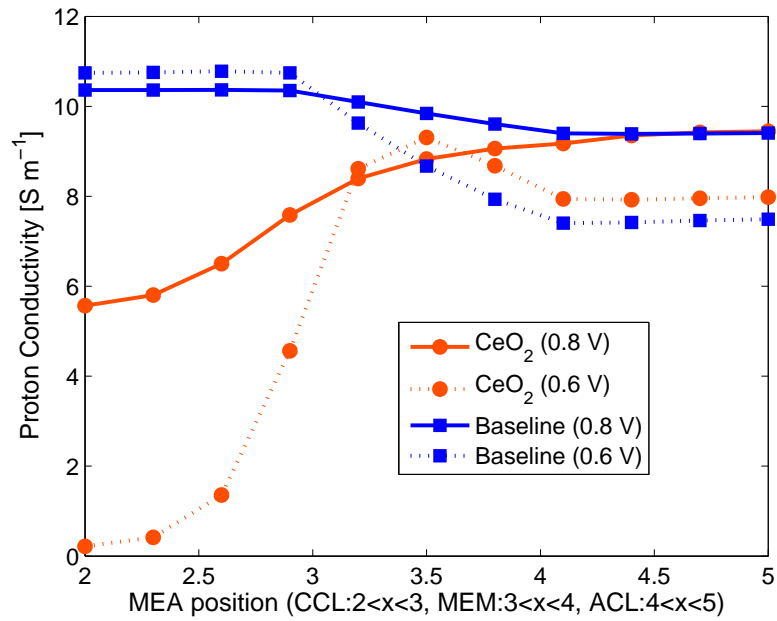


Figure 6: Simulated proton conductivity in the ionomer phase across the cathode CL ($2 < x < 3$), membrane ($3 < x < 4$), and anode CL ($4 < x < 5$) baseline and ceria-supported MEAs.

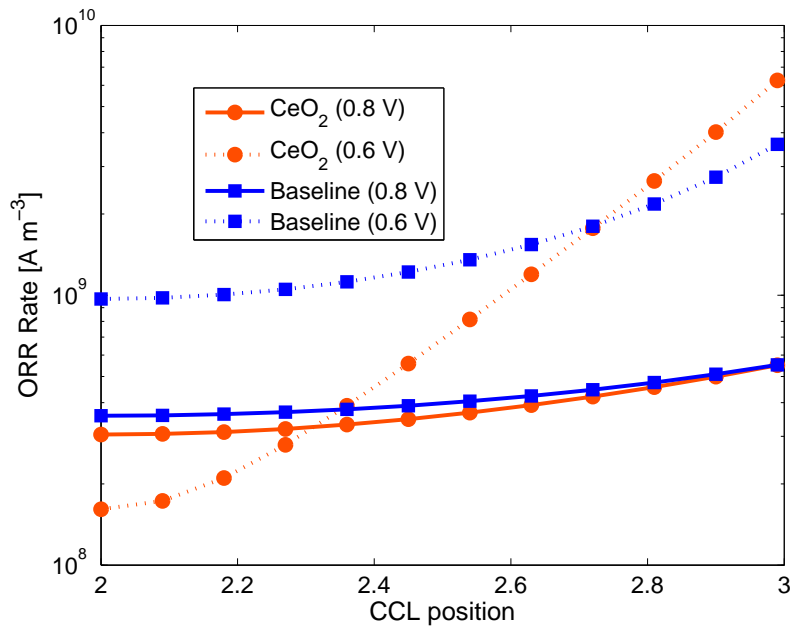


Figure 7: Simulated four-electron ORR rate in the cathode CL for baseline and ceria-supported MEAs.

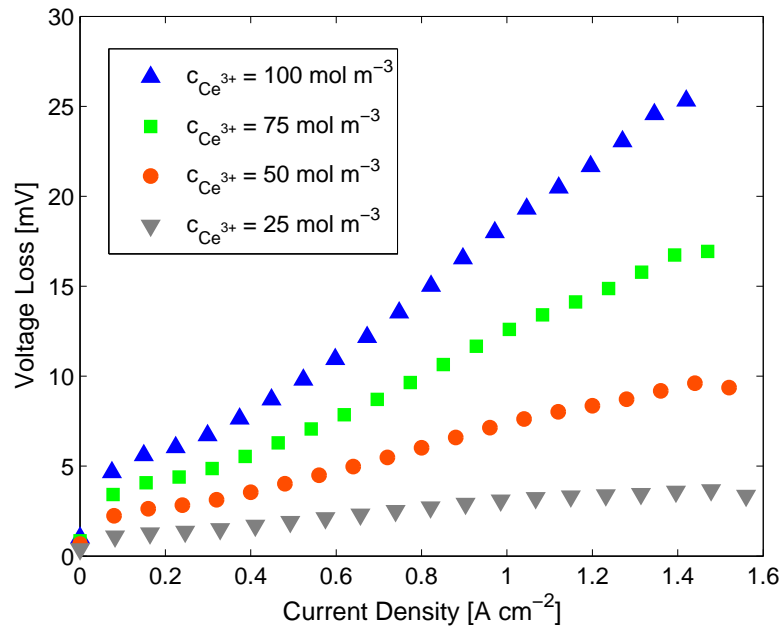


Figure 8: Simulated voltage losses of ceria-supported MEAs under reference ($c_{\text{Ce}^{3+}} = 100 \text{ mol m}^{-3}$), and reduced cerium ion concentration ($c_{\text{Ce}^{3+}} = 75, 50$ and 25 mol m^{-3}) conditions.

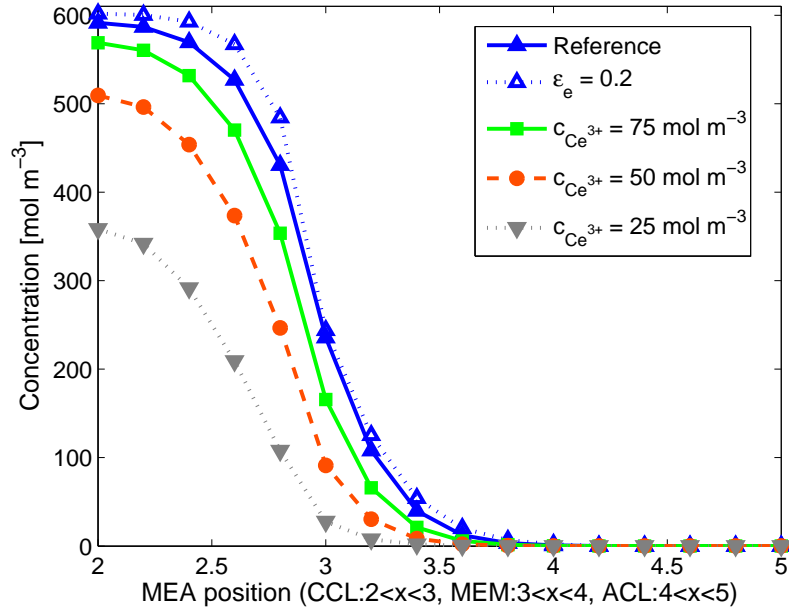


Figure 9: Simulated Ce^{3+} concentrations in the ionomer phase at 0.6 V under reference ($c_{\text{Ce}^{3+}} = 100 \text{ mol m}^{-3}$ and $\epsilon_e = 0.27$), reduced ionomer volume fraction ($\epsilon_e = 0.2$), and reduced cerium ion concentration ($c_{\text{Ce}^{3+}} = 75, 50$ and 25 mol m^{-3}) conditions.

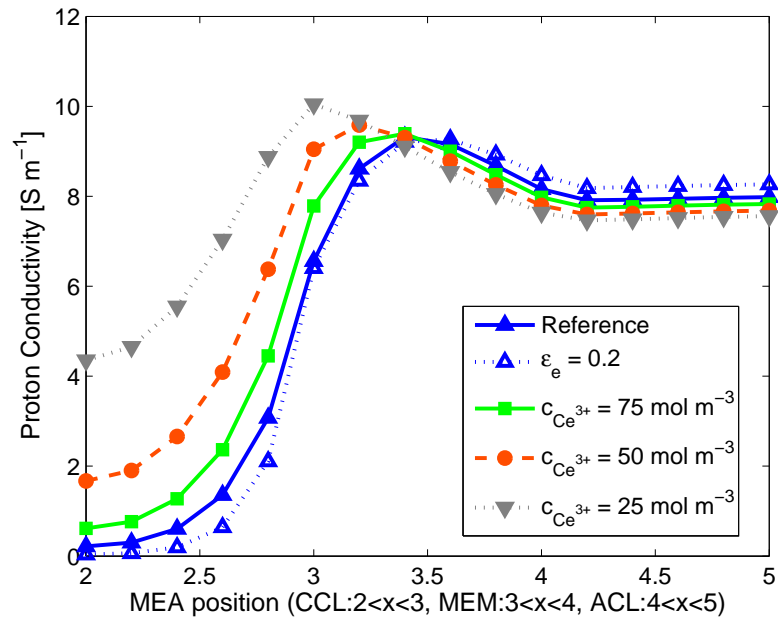


Figure 10: Simulated proton conductivities in the ionomer phase at 0.6 V under reference ($c_{Ce^{3+}} = 100 \text{ mol m}^{-3}$ and $\epsilon_e = 0.27$), reduced ionomer volume fraction ($\epsilon_e = 0.2$), and reduced cerium ion concentration ($c_{Ce^{3+}} = 75, 50$ and 25 mol m^{-3}) conditions.

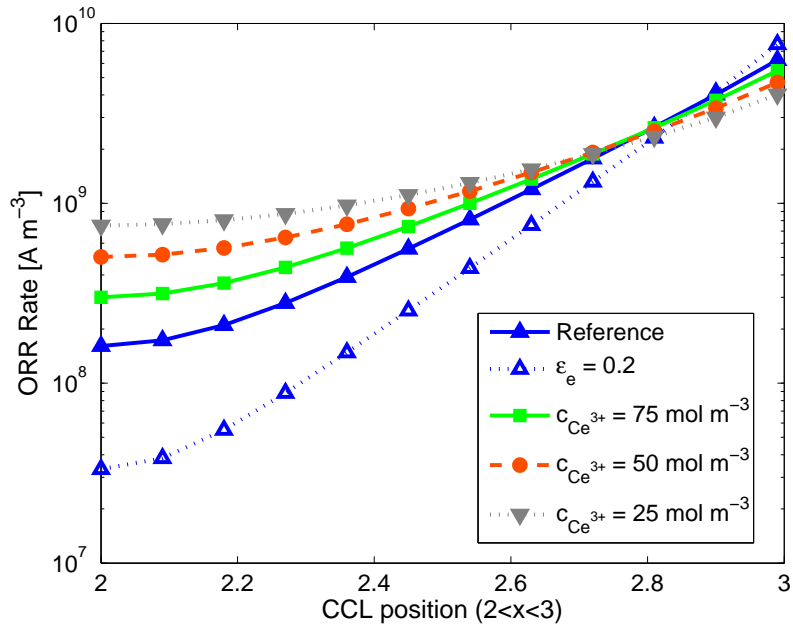


Figure 11: Simulated ORR rate in the cathode CL at 0.6 V under reference ($c_{\text{Ce}^{3+}} = 100 \text{ mol m}^{-3}$ and $\epsilon_e = 0.27$), reduced ionomer volume fraction ($\epsilon_e = 0.2$), and reduced cerium ion concentration ($c_{\text{Ce}^{3+}} = 75, 50$ and 25 mol m^{-3}) conditions.

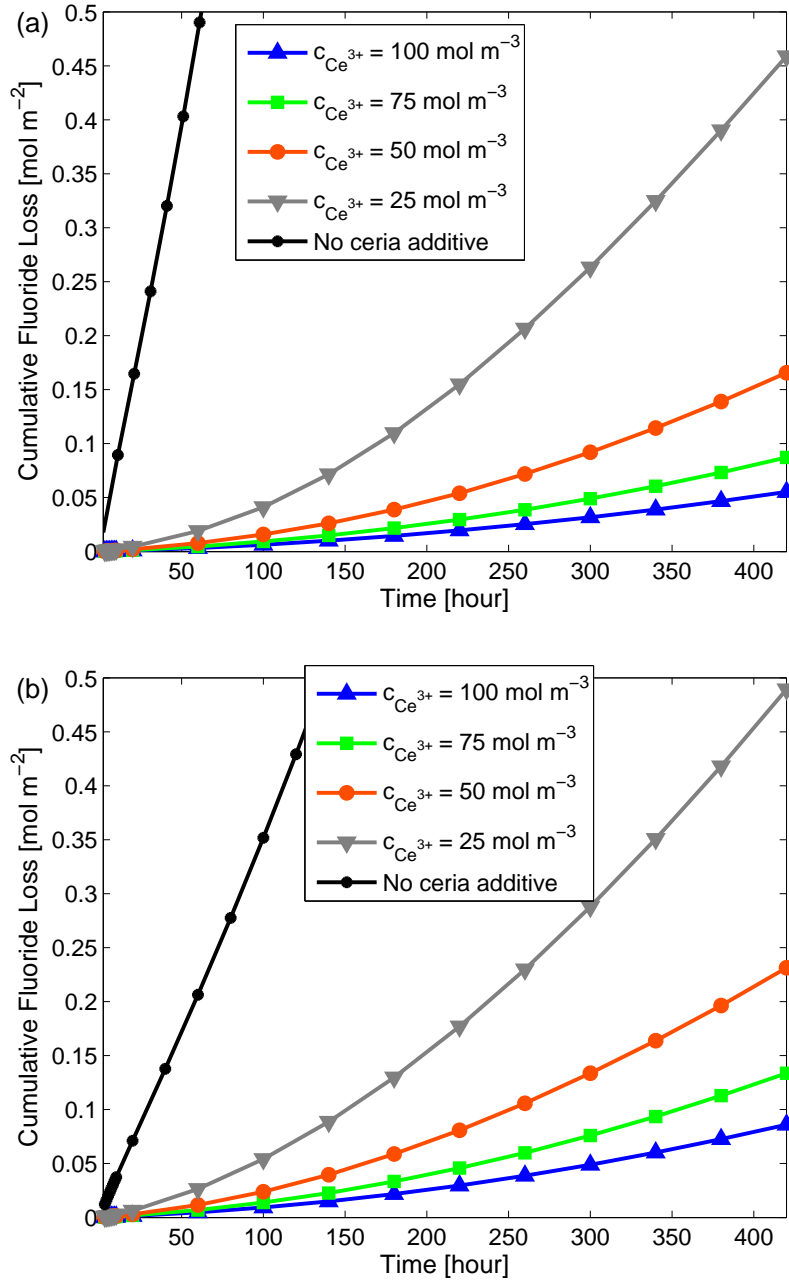


Figure 12: Simulated cumulative fluoride release as a function of the initial Ce^{3+} concentrations in the membrane at (a) OCV and (b) 0.8 V.

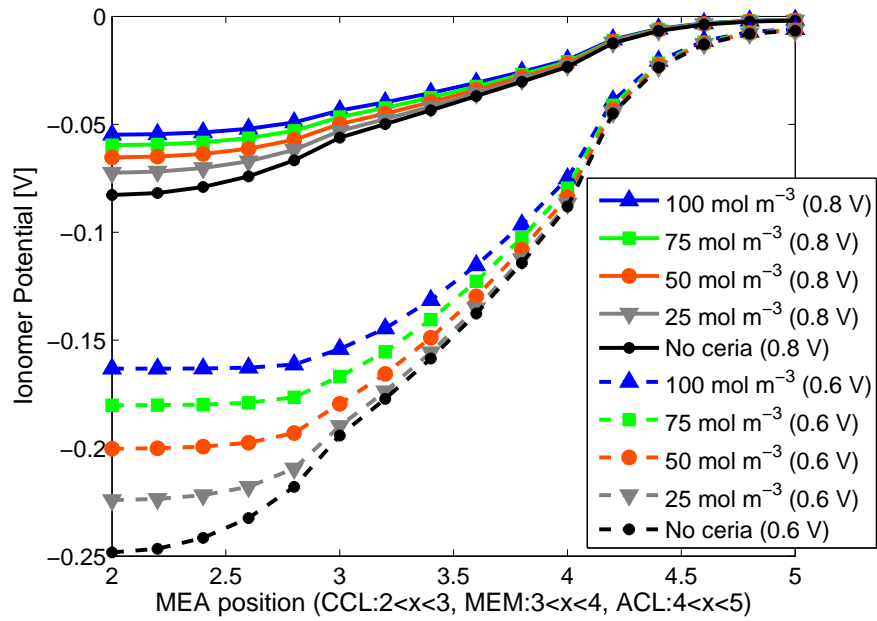


Figure 13: Simulated ionomer potential under reference ($c_{\text{Ce}^{3+}} = 100 \text{ mol m}^{-3}$) and reduced initial cerium ion concentration ($c_{\text{Ce}^{3+}} = 75, 50 \text{ and } 25 \text{ mol m}^{-3}$) conditions.

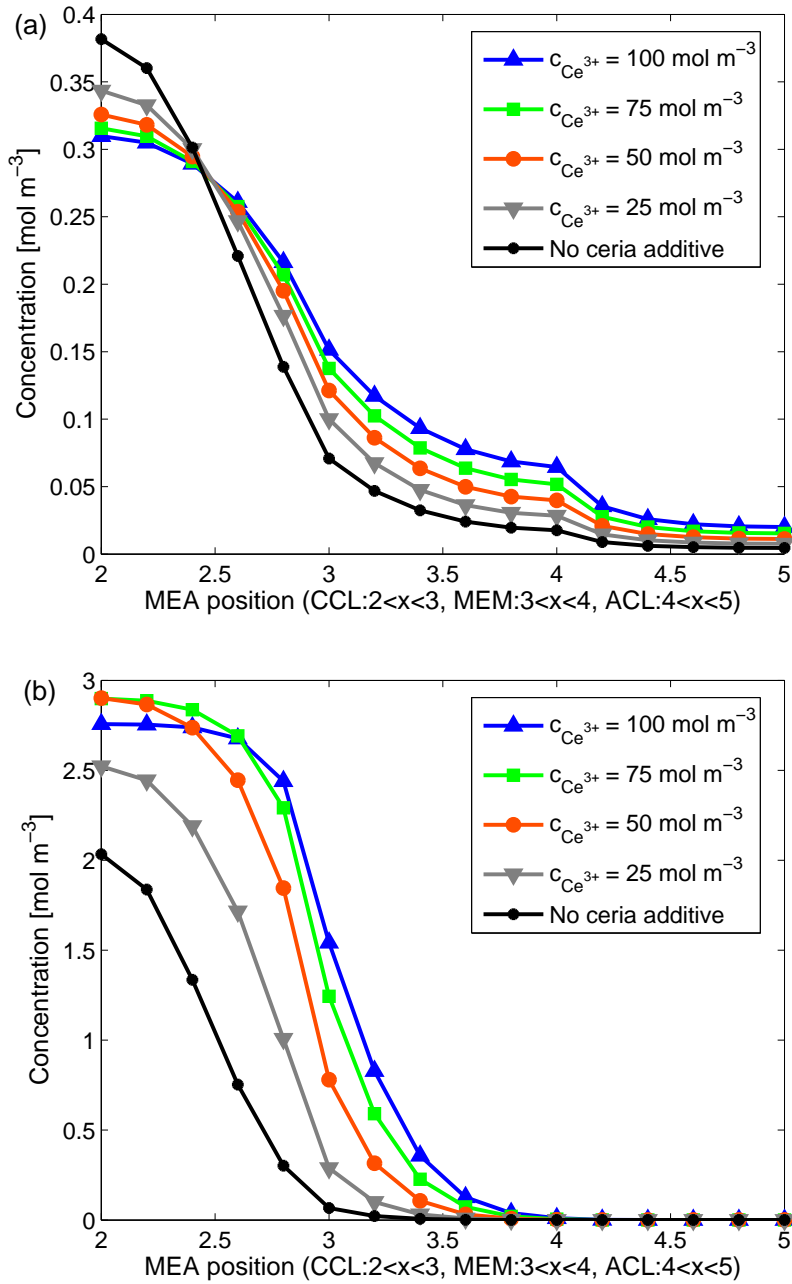


Figure 14: Simulated iron(II) concentration in the ionomer phase of the cathode CL at (a) 0.8 V and (b) 0.6 V under reference ($c_{\text{Ce}^{3+}} = 100 \text{ mol m}^{-3}$) and reduced initial cerium ion concentration ($c_{\text{Ce}^{3+}} = 75, 50$ and 25 mol m^{-3}) conditions.

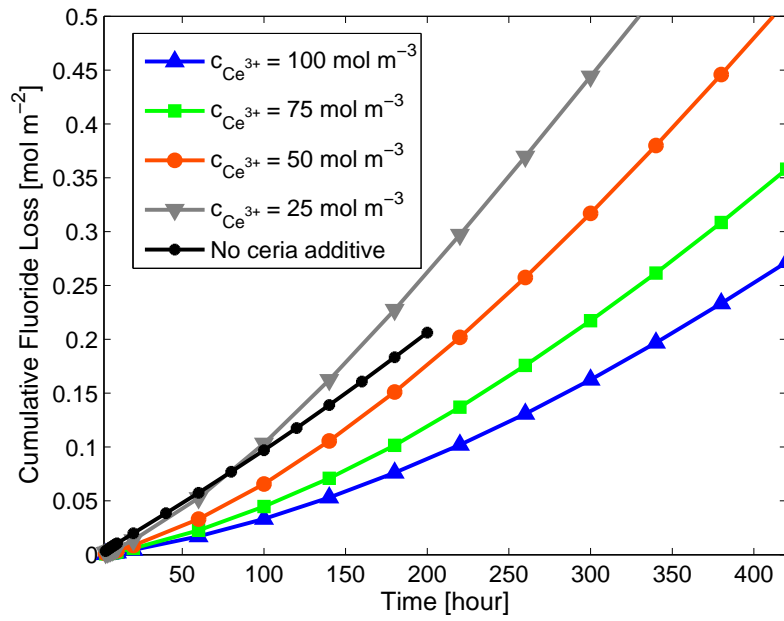


Figure 15: Simulated cumulative fluoride release as a function of the initial Ce^{3+} concentration in the membrane during fuel cell operation at a constant cell voltage of 0.6 V.

Tables

Table 1: Structural and physical parameters used in the model.

Parameter	Symbol	Value (Unit)
Thickness of:		
GDL macroporous substrate	L_{GDL}	250 (μm)
MPL subdomain	L_{MPL}	25 (μm)
CL	L_{CL}	10 (μm)
Membrane	L_{m}	30 (μm)
Porosity of:		
GDL macroporous substrate	ε_{GDL}	0.78 [48]
MPL subdomain	ε_{MPL}	0.65 [48]
CL	ε_{CL}	0.4 [49]
Ionomer fraction in CLs	ε_{e}	0.27
Faraday's constant	F	96485 (C mol ⁻¹)
Gas constant	R	8.314 (J K ⁻¹ mol ⁻¹)

Table 2: Parameters associated with calculation of reaction kinetics

Parameter	Value (Unit)
Volumetric specific surface area, a	10^4 (m^{-1})
HOR Exchange current density, $i_{\text{HOR},0}$	10^5 (A m^{-2})
4e ORR Exchange current density, $i_{4e,0}$	1 (A m^{-2})
Equilibrium potential for:	
4e ORR, $E_{4e,eq}$	$1.23 - 0.9 \times 10^{-3}(T - 298.15)$ (V)
HOR, $E_{\text{HOR},eq}$	0 (V)
Reference proton concentration, $c_{\text{p},0}$	1800 mol m^{-3}